High-Performance 3-D Imaging Algorithms for UWB Pulse Radars

by

Shouhei Kidera

Acknowledgments

Preface

Non-destructive testing or measurement for precision devices such as reflector antennas, requires high-performance image reconstruction systems. There are also emergent demands from the proximity imaging systems for moving robots or vehicles aimed at Intelligent Transport System (ITS). These applications require different kinds of performance, such as real-time operation, fine resolution, robustness and others. Much research focusing on high-grade imaging systems with a wave has been carried out, which are based on optical, ultrasonic and radio detections. Each method however, has its own unique problems, and it is difficult to achieve all the required performance to a high degree. This thesis introduces an imaging system and algorithm with pulse radars, which has an advantage in range resolution. Formerly, pulse radar systems never dealt with proximity imaging due to the limited frequency bandwidth of signals. However, in recent years, Ultra Wideband (UWB) signal has been regulated and approved in several countries including Japan. UWB pulse radar systems show great promise in dealing with near field imaging and with considerably high range resolution.

Much research has been carried out on sensing algorithms with radar such as SAR, range migration and diffraction tomography. It is well-known that proximity imaging with radars often becomes an ill-posed inverse problem. Most conventional algorithms are therefore, based on a recursive optimization or model-based approach, which requires intensive computational resources. As such, they are not applicable to real-time applications, which are needed for robotic and other visualization systems. To solve this problem, SEABED (Shape Estimation Algorithm based on BST and Extraction of Directly scattered waves) has been proposed. It can deal with real-time imaging using a nonparametric approach. SEABED utilizes a reversible transform BST (Boundary Scattering Transform) between the target boundary and the estimated time delays. The observed data can be transformed directly to the target boundary with this transform, and it produces real-time imaging. However, this method has several problems, which must be solved before high-performance imaging in a real environment is possible. This thesis pays attention to the problems inherent in SEABED, and offers a new imaging algorithm, which is suitable for high-grade proximity imaging.

SEABED assumes 2-D scanning of mono-static radar, and requires a great deal of time for data acquisition. To increase the speed of imaging with SEABED, we utilize a linear array antenna and shorten the time taken for data acquisition by scanning this array.

However, the resolution of the original SEABED is limited by the number of antennas, and, in general, the interval of the array antennas should be greater than half of the transmitted wavelength. Therefore, the resolution of the estimated image is relatively low for the array direction. To solve this problem, we extend a reversible transform BST to a bi-static radar system. The extended BST enables us to obtain finer resolution by increasing the estimated points to the combinations between the transmitted and received antennas. We evaluate the performance using numerical simulations and experiments.

SEABED has another serious problem in that the estimated image is extremely unstable in a noisy environment, because BST utilizes the derivative of the received data. To resolve this instability, adaptive smoothing algorithms have been proposed. Although these approaches accomplish a robust imaging, there is a trade-off between the resolution and the stability due to data smoothing. We propose a new imaging algorithm with an envelope of spheres, to minimize this trade-off, and which can realize robust imaging even in noisy environments. This method utilizes the principle that the target boundary can be expressed as an envelope of the spheres, which can be determined by the antenna locations and the time delays. It can realize rapid, robust 2-D or 3-D imaging without derivative operations, and this completely removes the trade-off between resolution and stability.

The resolution of the estimated image with an envelope of spheres is distorted by the scattered waveform deformations, even in the absence of noise. The obtained image deteriorates, especially around the target edges. To enhance the resolution, we synthesize the shape and waveform estimations. Numerical simulations and experiments verify the effectiveness of this algorithm in 2-D problems. The accuracy with this method increases to 1/100 of the center wavelength of the transmitted pulse, which has never been accomplished with conventional radar systems. However, this method is based on a recursive approach, and requires intensive computation for 3-D problems. To resolve this problem, we propose a fast, high-resolution imaging algorithm with spectrum offset correction of received signals. This method compensates for measured errors due to the waveform estimations by utilizing the center frequencies of received signals. We verify that it can realize high-performance 3-D imaging, with respect to rapidness, robustness and fine resolution in numerical simulations and experiment.

Contents

List of Tables

List of Figures

xi

Chapter 1

General Introduction

1.1 Introduction

Appearances from high-performance imaging techniques are highly desired for use in various sensing applications. These can be applied to the non-destructive testing of a reflective surface, such as antennas, aircraft and other industrial devices, which have precision structures. On the other hand, the emergent development of robotic techniques demands high-grade imaging systems. Moving robots and vehicles must locate and specify various objects rapidly, in order to avoid collisions or to identify the target. For these applications, many different image reconstruction systems have been developed, based on wave propagation and which utilize either visible rays, ultrasonic waves, X-rays, radio waves or some other waveform. In near field imaging for robots, many studies have been based on optical approaches involving either passive or active sensor techniques. However, these techniques have a problem in terms of lower range resolution, even if they make the best use of the complicated systems or multiple sensors. Although ultrasonic imaging has been applied successfully in the medical and biological fields and has an advantage for fine range-resolution, there is insufficient research to achieve high-performance imaging in the free space.

Pulse radar systems have been developed as a sensing application for terrain surfaces and for embedded landmines or pipes underground. This is because the short radio pulse radiation through the air has been prohibited to avoid the interferences for other signals. The Ultra Wideband (UWB) signal was regulated by the Federal Communications Commission (FCC) in 2002, and has been approved in European countries and also in Japan. UWB signals enable us to achieve proximity imaging with considerable high-range resolution. However, the conventional radar imaging algorithms have many problems, for example intensive computation, instability, and lower resolution. Furthermore, there is insufficient comprehensive research on the assumed applications. This paper proposes a promising study on high performance radar imaging, that makes use of the characteristics of UWB signals. In the remainder of this chapter, we introduce the background to our

research, and describes the problems of conventional radar systems. The contribution of this thesis is presented at the end of the chapter.

Required Performance of Imaging

Let us introduce the performance criteria required for general proximity imaging. While the required performances is variable and dependent on the particular application, the primary and essential requirements are listed below.

- **Rapidness**

- **Robustness**

- **Flexibility**

- **Accuracy**

- **Resolution**

Rapidness refers to the speed with which the images are updated, and is highly significant for a realtime collision avoidance in dangerous situations for vehicles or moving robots. **Robustness** is indispensable as it deals with the image reconstruction in noisy or cluttered environments. If there is not enough robustness in the imaging, we need to oversee the system to avoid the calculative divergence, which can result in dangerous situations. **Flexibility** refers to the applied range of the imaging techniques, in order to deal with the kinds of situations or target models in the application. Highly flexible imaging can be applied to and is suitable for imaging systems for robots, which must be able to deal with many kinds of objects and unpredictable situations. **Accuracy** is expressed as the locationing errors of the target, and is necessary for nondestructive measurement, which must detect small defects on precision surfaces. Moreover, accurate imaging enables us to capture fragile objects, such as human tissue, where it is vital not to misread the measurement. **Resolution** is expressed as the fineness or sharpness of the obtained image, and determines the characteristics of the estimated target with regard to edges, wedges, and plain or curved surfaces. It is less important and not as indispensable when compared to the other requirements. Fine resolution is, however, still necessary for target identification and to highlight the details, such as for individual recognition based on the characteristics of a human face or a fingerprint. Since it is generally hard to achieve all these performances requirements to a high degree, we must select the most critical requirements for the assumed system.

1.2 Image Reconstruction with Wave Propagations

A large number of imaging techniques utilizing wave propagations have been studied and some of these have already been put to practical use. The type of waves, which have been
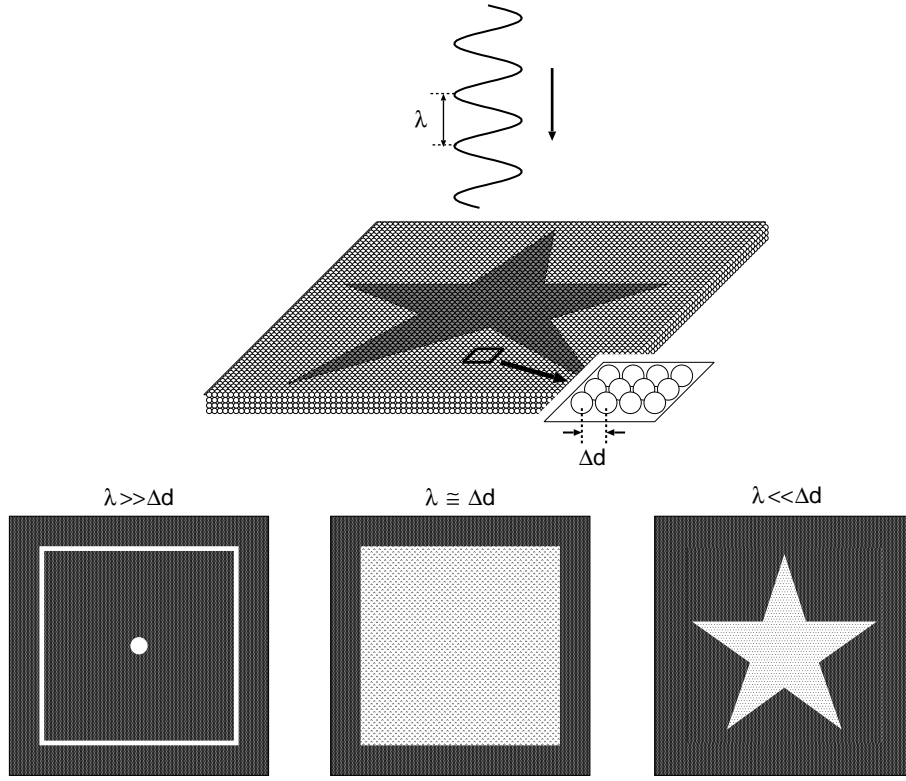
Figure 1.1: Estimated images for different relationship between surface roughness and incident wavelength.

highly studied in these recent works, can be divided into the following groups:

- **Visible ray**

- **Ultra sonic**

- **X-ray**

- **Radio**

A visible ray wave is an electromagnetic wave with a wavelength between 4.0×10^{-7}m and 8.0×10^{-7}m. Ultra sonic waves are defined as longitudinal waves through solids, liquids or air, which have a higher frequency than 20 kHz, and the wavelength of which corresponds to 1.7×10^{-2}m at room temperature. X-ray and radio waves are electromagnetic waves whose wavelengths are in the range 10^{-11}m $\leq \lambda \leq 10^{-8}$m and 10^{-3}m $\leq \lambda \leq 10^{2}$m, respectively.

The characteristics of the estimated image obtained with each wave are mostly determined by the transmitted wavelength. This is because the obtained target image
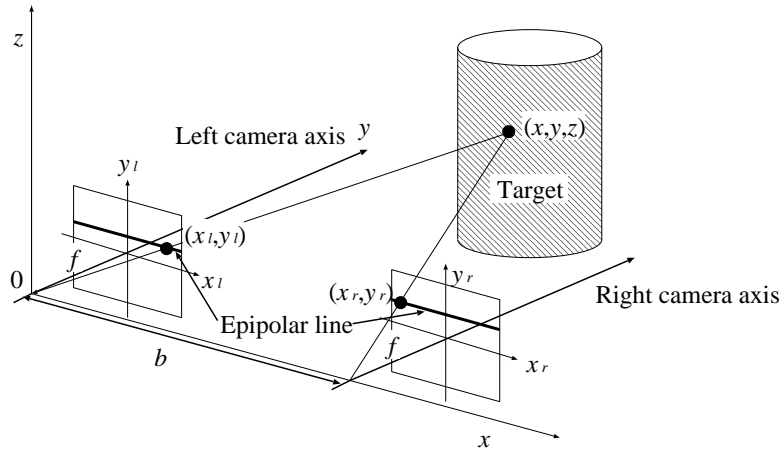
Figure 1.2: Model of passive stereo imaging.

depends on the relationship between the surface roughness of the target and the incident wavelength. Fig. 1.1 shows this relationship and the expected images in each case. Δd expresses the order of the roughness of the target surface, and λ is an incident wavelength. In $\lambda \gg \Delta d$, which corresponds to the use of radio or ultrasound waves, an incident wave is strongly reflected in one direction, which satisfies the law of reflection. In addition, a diffraction wave can be observed from the target edge or wedges. As a result, we obtain the image as shown on the extreme left of Fig. 1.1. In $\lambda \simeq \Delta d$, which corresponds to the use of visible ray waves, a comprehensive image of the target is obtained as shown in the middle of Fig. 1.1. This is because the diffraction wave from all the surface points can be observed. In $\lambda \ll \Delta d$, which corresponds to X-ray waves, the wave penetrates the target surface, and is diffracted by embedded objects which have structures with a less scale than the wavelength. The expected image is shown as on the extreme right of Fig. 1.1.

1.2.1   Visible Ray Wave

Various visualization techniques for robots employ photographic cameras. However, a photometric image does not include the range information, which is required to reconstruct the 3-D target image. To obtain the range information, passive and active range sensor techniques have been developed.

Passive Sensor Imaging

A passive sensor scanner does not radiate any form of waves itself, but relies on detecting reflected ambient radiation. In most cases, passive sensors measure the distance to the target using triangulation principles with two optical cameras. Fig. 1.2 shows a model for

4
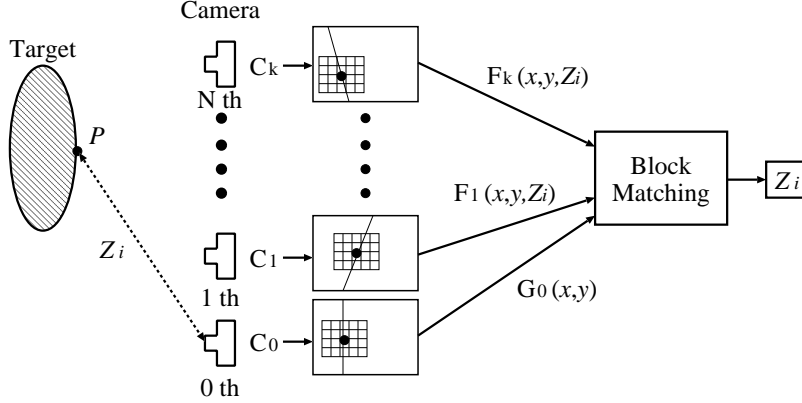
Figure 1.3: Principle of multiple baseline stereo matching.

passive stereo imaging. The surface point on the target (x, y, z) is calculated as

$$(x, y, z) = \frac{b}{x_l - x_r}(x_l, y_l, f), \tag{1.1}$$

where f and b are the focus distance and the length of baseline, respectively. (x_r, y_r) and (x_l, y_l) express the projective locations on the right and left side of the cameras, respectively. Eq. (1.1) enables us to determine each target point; however, this method requires the point or block matching method between the left and right projective images. The configuration of this method is quite simple, and has a high accuracy for near field targets. However, in the case of a longer baseline or distance to targets, it cannot obtain sufficient range accuracy because the pattern matching becomes quite difficult and complicated. Moreover, there is a trade-off between resolution and robustness in passive stereo imaging for the following reasons. If the size of comparative region is small, a mismatch occurs in the pattern matching resulting in deterioration of the estimated accuracy. On the other hand, where the region is too large, the resolution of the image is, in general, lower.

To enhance the performance of passive stereo imaging, the multiple baseline stereo method can be applied. The principle and characteristics of multiple sensor fusions can be described as follows [1, 2]. Fig. 1.3 shows the model of stereo matching with multiple baselines. We assume that N cameras are used. $G_k(x.y)$ is defined as the image obtained with the k th camera. Z_i is defined as the distance between point P on the target and the location of the 0 th camera. We define $(x_k(x, y, Z_i), y_k(x, y, Z_i))$ as the point on the k th camera, which corresponds to the point P. In the parallel stereo case, $x_k(x, y, Z_i) = x - bf/Z_i$ and $y_k(x, y, Z_i) = y$ hold. The brightness of the k th camera is defined as $F_k(x, y, Z_i) = G_k(x_k(x, y, Z_i), y_k(x, y, Z_i))$. Z_i is calculated by

$$Z_i = \arg\min_{Z_i} \sum_{p=-n_1}^{n_1} \sum_{q=-n_2}^{n_2} \sum_{k=1}^{N} W_{p,q}|F_k(x+p, y+q, Z_i) - G_0(x+p, y+q)|, \tag{1.2}$$

5

Eq. (1.2) compares the similarity between $G_0(x, y)$ and $F_k(x, y, Z_i)$ for all cameras. We utilize block matching around a point, where the each number of block for x and y is set to $2n_1+1$ and $2n_2+1$, respectively. $W_{p,q}$ is a weight for each window. In general, the accuracy and robustness of multiple stereo imaging can be enhanced by increasing the number of cameras. However, it has been verified that to be effective, the number of cameras should be less than 10. In addition, the accuracy of the range estimation can be approximated as $|\Delta Z| = \dfrac{Z^2}{bf}|\Delta d|$, where Δd expresses the error scale of the obtained images. By utilizing this relationship, the accuracy of stereo imaging in an ideal environment can be estimated as $|\Delta Z| = 20$mm, where $b = 300$mm, $f = 16$mm, $Z = 300$mm , and $|\Delta d| = 1$mm. This level of accuracy is not acceptable for our applications.

Many studies have been done in optical stereo imaging [3–9]. H. Jeong and Y. Oh have proposed a fast, effective stereo imaging method by positioning the three cameras in triangularization and utilizing the local disparity slice on a linear array sensor [10]. S.H. Seo et al. have proposed an accurate, robust imaging system based on the least squares filtering scheme [11]. It matches the left and right disparity image block in least squares about the image pattern, and determine the optimum weight in the matching filter. G.L. Mariottini et al. utilize an epipolar geometry with pinhole camera for visualization of serving robots [12]. This system can realize target identification for robots without preliminary geometrical knowledge. V. Lippiello et al. utilize a position based serving robot with hybrid eye-in-hand/eye-to-hand multi-camera system [13]. This method estimates the position of the objects based on an extended Kalman filter with visual feedback data. The Fusion algorithm with a radar system is also promising as an intelligent transport system [14]. This system estimates the 2-D image with a CCD camera, obtains the depth of the target using radar, and accomplishes the 3-D positioning of the target. Although various kinds of algorithm have been developed [15–17], they all depend on the target shape or situation and there is trade-off between speed and robustness in each imaging algorithm. The fusion techniques, however, which incorporate both an optical approach and radar, show great potential for high-performance imaging by compensating for each demerit.

Active Sensor Techniques

Active scanners emit some form of radiation and then detect the reflection in order to probe an object or environment. Various active range sensor systems have been proposed, and they can be classified as either

- Trigonometric method,

- Time-of flight method.

Trigonometric methods measure the distance to the target based on the triangular principle. In time-of flight methods, the round-trip time for a light pulse to be transmitted
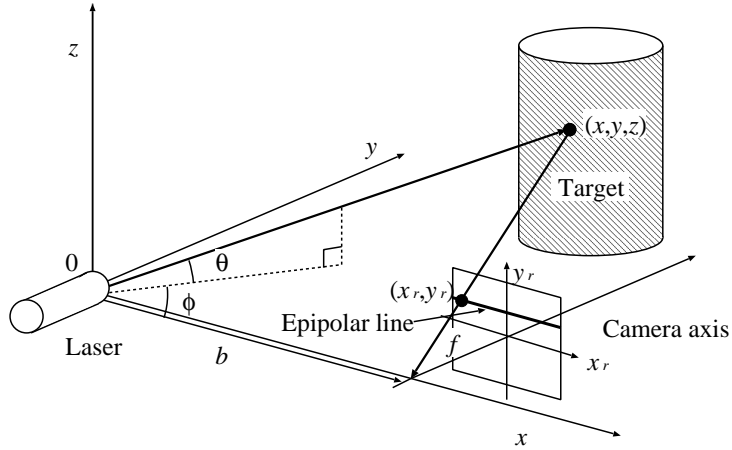
Figure 1.4: Model of active trigonometric imaging.

and received, is used to measure the distance. It is mostly used as a laser range finder. We now introduce active sensor scanning based on the trigonometric method.

A laser sensors technique based on active trigonometric imaging is one of the most efficient algorithms using active sensors. Fig. 1.4 shows a system model for active trigonometric imaging. In this model, we locate a laser source and a CCD camera separately. We can measure the incident angles as θ and ϕ, and obtain the projective image of the CCD camera as (x_r, y_r). The spotted point on the target boundary (x, y, z) is calculated as

$$(x, y, z) \; = \; b \left(\frac{1}{\tan \phi} - \frac{x_r}{f} \right)^{-1} \left(\frac{1}{\tan \phi}, \; 1, \; \frac{1}{\cos \phi \tan \theta} \right), \qquad (1.3)$$

Eq. (1.3) can determine the target locations in 3-dimension without the pattern matching, that is required for passive stereo imaging. However, the laser beam is required to scan all directions to obtain the comprehensive target image. To enhance the speed of imaging, light pattern modulations have been proposed, such as slitting patterns or coded patterns. These methods achieve fast scanning and effective imaging with high-resolution. However, they depend significantly on the shape of the target boundary because the coded pattern can be modified by the target gap.

To obtain finer range resolution, active array sensor imaging systems has been proposed [18, 19]. A high-resolution image for general objects is obtained by utilizing the interferogram on the array aperture and eigen vector of the power correlation of the data. However, this method incorporates an iterative algorithm, and take more than 1.0 sec to obtain the image. A high-speed scanning active sensor has been developed, and unlike stereo imaging, it does not utilize block matching but instead utilizes the light section method [20]. Other approaches based on optical probing are useful for imaging surface

details or constructions of the order nm [21]. Light detection and ranging (Lidar) techniques have been developed to measure the leaf area density of trees for example [22, 23]. Large-footprint airborne lidar has been used to estimate the vertical canopy surface profile on the basis of the waveforms of returned pulses. Using a voxel-based algorithm, it has been shown that the leaf area of a tree can be imaged in finer spatial resolution. However, this methods requires scanning of the laser beam in principle, and cannot resolve the trade-off between the accuracy and rapidness of the imaging.

Like other applications, Intelligent Transport Systems (ITS) enhance the development of proximity imaging based on optical and radar approaches. Such systems require both a real-time and accurate measurement. Active laser scanning and trigonometric imaging have mainly been developed for this purpose [24–26]. Real-time 3-D visualization for vehicles has been developed, which can realize high-speed visualization within 60 msec by combining the depth map around the vehicles, which can be determined by the distance to visible road markings, and image contrasts higher than a given threshold [27].

As a fusion technique, laser radar which can detect the forward objects on and alongside the road, is known as as vehicle-mounted scanning laser radar (SLR). It is often utilized as an on-board sensor for headway distance measurement systems [28–33]. This system utilizes the fact that vehicles are generally equipped with reflectors, which can reflect sufficiently from the laser radar beams. The major approaches of SLR are based on grouping the detecting points with the close range and movement vectors. In general, the size of the vehicles are smaller than the white lane, which can be detected with SLR. With this preliminary knowledge, the method achieves a real-time and accurate forward measurement to avoid collisions. However, this method has the same problem as the point or pattern matching for general proximity imaging, where the preliminary knowledge about the target or obstacles cannot be obtained. Although many kinds of active sensor imaging have been proposed [34], they have problems in terms of robustness, rapidness and the limitations on the preliminary assumed model.

In general, imaging with light waves has an advantage in angular resolution. This is because the scattered wave can be diffracted on target surfaces, which have roughness smaller than the wavelength. On the contrary, ultrasonic and radio wave are useful for high-range resolution with regard to the wavelength. Synthesis of these techniques seems to be promising for proximity imaging.

1.2.2   Ultra Sonic Wave

An ultrasonic wave is a kind of sound wave, which has a frequency greater than 20 kHz. Various imaging techniques with ultrasonic wave have been developed for the purpose of medical applications. This is because these waves can propagate through human organs and tissue while optical methods cannot be applied. Furthermore, a device for ultrasonic signals is more inexpressive and simpler compared to that for radio waves because the sampling rate of the ultra sonic wave is considerably lower than the radio wave. How-
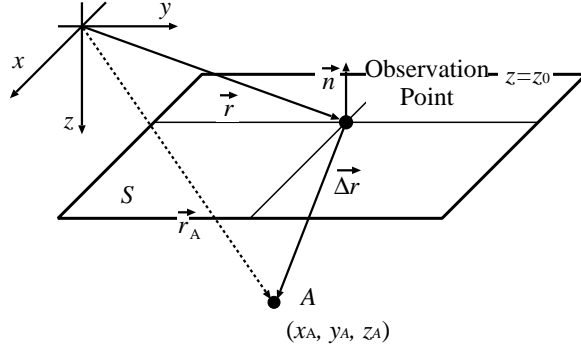
Figure 1.5: Acoustic phased array model.

ever, the propagation range for this wave is narrower than that of radio waves, and the transmitting and receiving devices are more sensitive to the surrounding environment.

Ultrasonic techniques have been used successfully for many nondestructive inspection applications. With the combination of radiography, they have proven to increase the probability of defect detection. Phased array sectoral scans are used successfully in medical imaging [35]. We introduce an efficient algorithm with phased arrays to detect small defects on the girth weld of pipes. This method utilizes the acoustic theory of the inverse wave field extrapolation with a Rayleigh II integral. It is explained that the acoustic theory can also be applied to the individual shear and longitudinal components of the wave field. We assume the phased array on a certain plain. The general Rayleigh II integral derived from the Kirchhoff integral, is formulated as

$$R(\boldsymbol{r}_A, \omega) = \int_S P(\boldsymbol{r}, \omega) \frac{\partial G}{\partial n} \mathrm{d}S, \tag{1.4}$$

where $P(\boldsymbol{r}, \omega)$ is the Fourier transform of the pressured field $p(\boldsymbol{r}, t)$, $\boldsymbol{r}_A = (x_A, y_A, z_A)$ is the position vector of a point A not on the observation surface S, $\boldsymbol{r}$ is the position vector of an observation point on S, and n is the normal direction on the surface. Fig. 1.5 shows the coordinates of this model. In the assumed application, the source corresponds to the defects that act as reflectors or cause diffraction. For inverse wave field extrapolation, Eq. (1.4) yields

$$P(\boldsymbol{r}_A, \omega) = \frac{z_0 - z_A}{2\pi} \int_{-\infty}^{\infty} \int_{-\infty}^{\infty} P(\boldsymbol{r}, \omega) \frac{1 - \mathrm{j}k\Delta r}{\Delta r^3} \mathrm{e}^{\mathrm{j}k\Delta r} \mathrm{d}x \mathrm{d}y, \tag{1.5}$$

with $\Delta r = \sqrt{(x - x_A)^2 + (y - y_A)^2 + (z_0 - z_A)^2}$ and z_0 indicates the location of the recording plane. If the secondary source is present in A, extrapolation to that point causes in the energy of the secondary source to be focused. This method make use of a ray-tracing approach to solve Eq. (1.5), and can focus on the defect, the size of which is

9

of the order mm. However, it requires large computational resources, and as such is not suitable for real-time applications.

A global ultrasonic system has been developed for self-localization of a mobile robot with Kalman filtering for moving robots [36]. In this method, a robot with a receiver moves around the room by measuring the distance to obstacles, which have ultra sound generators on all corners. The state vector of the robots can be estimated by the extended Kalman filter, and can realize global localization in an indoor environment. A 3-D imaging algorithm based on volume-rendering has been developed, and it utilizes adaptive boundary detection, which is based on a user defined threshold [37]. By applying SAR principles to ultrasonic echographic imaging, a high-resolution imaging method with pulse compression has been developed [38]. A frequency division algorithm with SAR principles has also been proposed [39], and it can focus perfectly on all the points on the image. However, these methods require the focusing process of the SAR principles and fail to obtain sufficient resolution of the image.

In general, the velocity of ultrasound depends significantly on the temperature and pressure of the air, and ultrasound imaging cannot be utilized in the event of fire. Moreover, the angular resolution is generally lower than that of optical trigonometric imaging, and in order to obtain sufficient angular resolution, scanning or utilizing an array is necessary.

1.2.3 X-rays and Other Wave

These are useful for the detection of pathology of the skeletal system, and also for some disease processes in cancer of the soft tissues. Computed Tomography (CT) with X-ray wave is applied to visualize the cross-section of the human body. This principle can be applied with γ rays, ultra-sonic waves and nuclear magnetic resonance (NRM). The most simplest principle of this technique is based on the Fourier transform. We collect the signals received from the target in all direction, and construct the 2-D distribution of the signals. These signals correspond to the convolution between the transmitted signal and the 2-D distribution of the target medium. Therefore, we can determine the estimated 2-D target image by applying the inverse Fourier transform to the received signals. As a further example of medical imaging techniques, Magnetic Resonance Imaging (MRI) has recently been developed as a non-invasive measurement by utilizing Nuclear Magnetic Resonance. MRI has the ability to recognize the state of the target tissues, which is not possible with CT scans. Synthetic techniques incorporating both CT and MRI have been developed, and these can realize more accurate imaging as each compensates for the disadvantages of the other technique, and this is quite important for preoperative diagnosis [40–42]. Both of these imaging techniques are principally based on the tomographic approach, and require data sensed from all direction of the target. This requirement is hard to accomplish in moving robots or vehicles which must sense forward objects.

Infrared waves are utilized for night-vision sensors, where visible rays produce an

insufficient image of the object. They also enable us to distinguish warm targets, such as the human body or automobiles, and can be applicable for imaging in surveillance systems. These waves are also utilized in thermography, which is a non-destructive imaging that utilizes the thermal patterns and temperatures of the target. This method is widely utilized in industry for predictive maintenance. It is useful in imaging techniques where visible imaging is not applicable, and much research has focused on this [43–45]. As far as other promising techniques go, imaging with T-ray (Terahertz-ray) waves has been of considerable interest due to a number of new developments such as terahertz time-domain spectroscopy [46]. These techniques, however, have the same problems concerning range resolution for the same reasons as in the optical approaches. Nevertheless, fusion techniques with radar imaging appear promising for non-destructive imaging in various applications.

1.2.4 Radio Wave

Imaging with radio waves have the advantage of the high-range resolution, for the same reason as in ultrasound wave. Radio detection and ranging (Radar) has been developed for far field imaging or measurements of the surface of terrain or or the atmosphere, where acoustic waves cannot be applicable. Moreover, the recent development of wideband techniques enables us to deal with proximity imaging for radar systems as well. Radar can be applied in harsh environments, where optical and ultrasonic waves cannot be used such as in the case of fire, dark smoke or underground. Radar is also suitable for collision detection and distance measurement of vehicles, where the relative speed of the target may be more than 10 % of the acoustic velocity.

1.3 Direct Scattering Problems for Radar

This section describes the scattering problems in electromagnetic fields. In general, the calculation of the scattering field from an arbitrary dielectric or conductive distribution is known as the direct scattering problem. We introduce analytical and numerical solutions for this problem. The image reconstruction algorithm with radar should be derived from the understanding and formulation of the direct problem. Moreover, the imaging performance with radar can be enhanced by synthesizing the direct scattering solutions. This is the main idea of the imaging algorithm described in Chapter 4. Given bellow are the characteristics and application range for each solution of the direct problem.

1.3.1 Maxwell's Equations

Electromagnetic fields radiated by an induced current or voltage satisfy Maxwell's equations given as,

$$\nabla \times \boldsymbol{E}(\boldsymbol{r}, t) = -\mu \frac{\partial \boldsymbol{H}(\boldsymbol{r}, t)}{\partial t}, \tag{1.6}$$

$$\nabla \times \boldsymbol{H}(\boldsymbol{r}, t) = \epsilon \frac{\partial \boldsymbol{E}(\boldsymbol{r}, t)}{\partial t} + \boldsymbol{j}(\boldsymbol{r}, t), \tag{1.7}$$

$$\nabla \cdot \boldsymbol{E}(\boldsymbol{r}, t) = \frac{\rho(\boldsymbol{r}, t)}{\epsilon}, \tag{1.8}$$

$$\nabla \cdot \boldsymbol{H}(\boldsymbol{r}, t) = 0. \tag{1.9}$$

where $\boldsymbol{E}(\boldsymbol{r}, t)$, $\boldsymbol{H}(\boldsymbol{r}, t)$, $\boldsymbol{j}(\boldsymbol{r}, t)$ and $\rho(\boldsymbol{r}, t)$ express an electric, magnetic field, current and charge density, respectively at the location $\boldsymbol{r}$ and time t [47–49]. ϵ and μ express electric permittivity and magnetic permeability, respectively. Eqs. (1.6) to (1.9) are fundamental equations that solve the direct scattering problem. If an induced source, electric permittivity and conductivity are given, these equations can be solved with assumed boundary conditions. However, in general, they cannot be solved analytically, except in some cases. Therefore, many different numerical or approximal solutions have been studied, which are based on discretization or optimization approaches. We introduce some of these analytical and numerical calculations below.

1.3.2 Finite Element Method

The finite element method (FEM) discretizes Maxwell's equations with the various grid models for the assumed space. This method has the advantage that it can be applied to a nonlinear medium or targets with complicated structures.

FDTD Method

Finite Difference Time Domain (FDTD) is one of the most popular and powerful methods in the FEMs [50, 51]. It can deal with the numerical calculation of the electro-magnetic field at any location in an arbitrary medium. This method discretizes Maxwell's equations in the space and time domains based on the Yee cell model, as shown in Fig. 1.6. We define $F_{i,j,k}^n$ as the field F at a point $(x, y, z) = (i\Delta x, j\Delta y, k\Delta z)$ at time $t = n\Delta$, where $\Delta x, \Delta y, \Delta z$ and Δt are the discretized space for the x, y, z directions and the time interval, respectively. For example, Eq. (1.7) is discretized as

$$\frac{H_{z_{i+\frac{1}{2},j+\frac{1}{2},k}}^{n+\frac{1}{2}} - H_{z_{i+\frac{1}{2},j-\frac{1}{2},k}}^{n+\frac{1}{2}}}{\Delta y} - \frac{H_{y_{i+\frac{1}{2},j,k+\frac{1}{2}}}^{n+\frac{1}{2}} - H_{y_{i+\frac{1}{2},j,k-\frac{1}{2}}}^{n+\frac{1}{2}}}{\Delta z}$$

$$= \frac{\epsilon_{i,j,k}^n \left\{ E_{x_{i+\frac{1}{2},j,k}}^{n+1} - E_{x_{i+\frac{1}{2},j,k}}^n \right\}}{\Delta t} + j_{x_{i+\frac{1}{2},j,k}}^n . \tag{1.10}$$
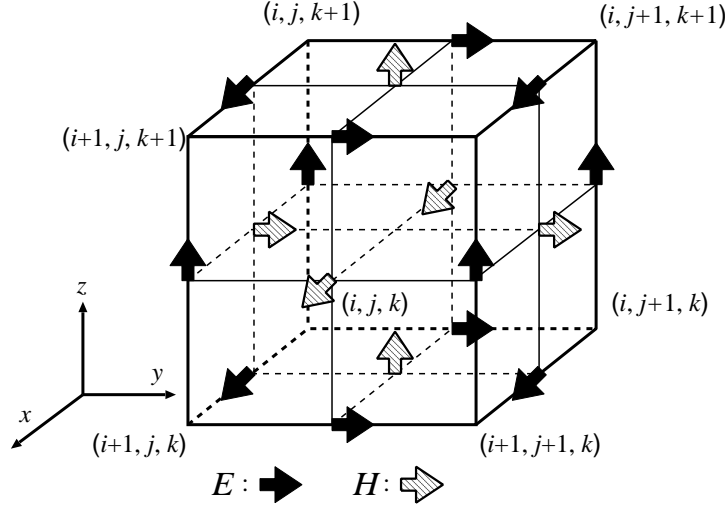
Figure 1.6: Yee cell model in FDTD method.

In general, the spatial and time grid sizes must be less than 1/10 of the transmitted wavelength to prevent the calculative divergence, known as the Courant condition. This method, thus, requires intensive computation for the calculation where the spatial scale is much larger than the wavelength. Accordingly, it is impractical to synthesize imaging algorithms to enhance their performance. Thus, by giving some constraints to the assumed problems, several solutions have been developed to reduce the computational resources.

1.3.3 Boundary Element Method

By utilizing Green's theorem, Maxwell's equations can be recast as the domain integral equation

$$g(\boldsymbol{r}) = \int_S K(\boldsymbol{r}, \boldsymbol{r}')f(\boldsymbol{r}')\mathrm{d}s', \tag{1.11}$$

where $g(\boldsymbol{r})$ and $f(\boldsymbol{r}')$ are expressed as an incident and scattered field, respectively, and S expresses the boundary for the assumed object. $K(\boldsymbol{r}, \boldsymbol{r}')$ is called the integral core which can be determined for the assumed problem. This equation is called a Fredholm integral equation of the first type. In the case of the scalar field of 3-D electromagnetic wave, Eq. (1.11) is expressed as

$$g(\boldsymbol{r}) = \frac{\mathrm{j}}{4}\int_S \left\{ G(\boldsymbol{r}, \boldsymbol{r}')\frac{\partial f(\boldsymbol{r}')}{\partial n'} - f(\boldsymbol{r}')\frac{\partial G(\boldsymbol{r}, \boldsymbol{r}')}{\partial n'} \right\}\mathrm{d}s', \tag{1.12}$$

where $G(\boldsymbol{r}, \boldsymbol{r}')$ is expressed by Green's function. The boundary element method (BEM) is efficient for the high-speed calculation of electromagnetic fields based on this type of

13

domain integral equation [52, 53]. It sets the unknown variables on the boundary, and solves these equations by resolving the matrix equation. BEM enables us to calculate the scattered field of simple linear or plane structures, and therefore is widely used for antenna or plane circuit analysis.

Moment Method

The moment method is one of the popular algorithms in the BEMs. In this method, an unknown function f is linearly expanded as

$$f \simeq f_{\mathrm{N}} = \sum_{n=1}^{N} \alpha_n f_n, \tag{1.13}$$

where α_n is an unknown constant, and the expansion function f_n is expressed as either the Delta, the step, the triangular, the Heaviside or the Tchebycheff function, for example, depending on the complications or the desirable accuracy of the assumed problems. α_n is an unknown constant. Here a residual R_N is expressed as

$$R_N = g - L f_N = g - \sum_{n=1}^{N} \alpha_n L f_n, \tag{1.14}$$

where L is a linear operator determined by the assumed problems, and includes differential and integral ones. The moment method assumes that R_N and a testing function $W_m, \ (m = 1, 2, \cdots, M)$ in the domain L, satisfy the perpendicular condition. Under this condition, Eq. (1.14) can be expressed as

$$\sum_{n=1}^{N} \langle W_m, L f_n \rangle = \langle W_m, g \rangle, \quad (m = 1, 2, \cdots, M), \tag{1.15}$$

where $\langle f, h \rangle$ is defined as the inner production. Thus, Eq. (1.15) can be expressed as the following matrix function,

$$\boldsymbol{A}\boldsymbol{\alpha} = \boldsymbol{B}, \tag{1.16}$$

where $\boldsymbol{A} = (a_{mn})$, $\boldsymbol{B} = (b_m)^T$, $\boldsymbol{\alpha} = (\alpha_n)^T$, $a_{mn} = \langle W_m, L f_n \rangle$ and $b_m = \langle W_m, g \rangle$ hold. We determine the unknown function f, by minimizing the next norm

$$\boldsymbol{\alpha} = \arg \min_{\boldsymbol{x}} \| \boldsymbol{B} - \boldsymbol{A}\boldsymbol{x} \|^2. \tag{1.17}$$

Eq. (1.17) can be solved by general numerical approaches, such as Gaussian-Jordan elimination. The Galerkin method determines W_m as the expansion function f_m. The moment method can realize more rapid calculation than the finite element method, however, it cannot be applied to general objects, which have a complicated shape or boundary. In addition, the computational time of this method largely depends on the assumed target boundary, and thus cannot be applied to the real-time solution of the direct problem.

1.3.4 Developed Approaches for Direct Problems

Many numerical approaches have been studied to enhance the accuracy or flexibility of the conventional solutions. The mode matching method utilizes the mode functions to expand the solutions to the 2-D Helmholtz equations. This method expresses each discretized point as a 1-D transmission line, and it enables us to deal with the scattering problem from arbitrary target boundaries. The TLM (Transmission Line Matrix) method is a discretized model of Huygens' principles to simulate the propagation of the secondary source excitations. The extended TLM has also been proposed by Yoshida as a Spatial Network method. EMS (Equivalent Source Method) approximates the scattering field from the target as the radiated field induced by the virtual source, which is located in the target. Each of these methods has both advantages and disadvantages, so the appropriate method must be chosen after considering the characteristics of the direct problem.

High-frequency Approximations

Geometrical Optics (GO) is widely utilized as a flexible, fast approach, which is based on high-frequency approximation. It assumes that the scattering scale of the target is quite a bit smaller than the propagation wavelength. This method cannot however, express the diffraction waves or other wave effects and the accuracy largely depends on the propagation wavelength. To solve these problems, Physical Optics (PO) has been developed, and this assumes the perfectly specular reflection for each local scattering point, even in edge points. Although the accuracy for PO does not depend on the frequency, it cannot express the diffraction effects perfectly. Geometry Theory of Diffraction (GTD) [54] is able to calculate the diffraction effects by utilizing the high-frequency approximation that expands the electric field about k^{-1} as

$$\boldsymbol{E}(\boldsymbol{r}) \simeq \mathrm{e}^{-\mathrm{j}k\Phi(\boldsymbol{r})} \sum_{m=0}^{\infty} (-\mathrm{j}k)^{-m} \boldsymbol{E}_m(\boldsymbol{r}) \ , \tag{1.18}$$

where $\Phi(\boldsymbol{r})$ is called as eikonal. Eq. (1.18) is known as the Luneberg-Kline expansion. $m = 0$ corresponds to GO. Fig. 1.7 shows the propagation model for the situation in which the ray makes the caustic. Electric field at the distance σ from σ_0 is expressed as

$$\boldsymbol{E}^{GO}(\sigma) = \boldsymbol{E}^{GO}(\sigma_0)\mathrm{e}^{-\mathrm{j}k(\sigma_0-\sigma)} \left[\frac{(R_1 + \sigma_0)(R_2 + \sigma_0)}{(R_1 + \sigma)(R_2 + \sigma)} \right]^{1/2} \ , \tag{1.19}$$

where the positions $R_1, -R_2$ on σ are called caustic points. In the case where the wave at σ_0 passes through the caustic points, the sign of the square root in Eq. (1.19) is negative and $\pi/4$ phase rotation is automatically calculated in Eq. (1.19). GTD is based on the assumption that the diffraction effect is a local effect and depends solely on the incident waveform and local shape of the target. Therefore, the strict solution for canonical problems, such as a wedge or infinite plain for example, is applicable to other problems, which include these types in the local shapes.

15
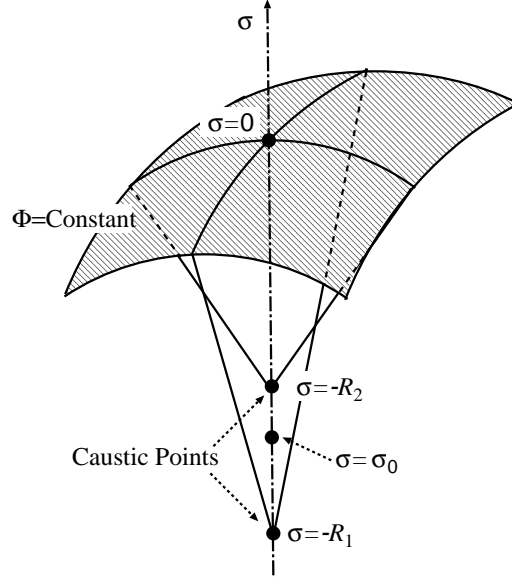
Figure 1.7: Propagation model where ray makes the caustic.

Canonical Problem with GTD

The analytical solutions for canonical problems using GTD are presented below. Fig. 1.8 shows a scattered model, which assumes a plain incident wave and the semi-infinite conductive plane. The diffraction waveform E_z^d is expressed as

$$
\begin{aligned}
E_z^d &= -E_z^i \frac{e^{-j(\pi/4)-jk\rho}}{2\sqrt{\pi}} \left\{ \frac{F_-(\xi^{i\,2})}{\xi^i} - \frac{F_-(\xi^{r\,2})}{\xi^r} \right\}, \\
F_-(\xi) &= 2\sqrt{\xi} e^{-j\xi - j(\pi/2)} \int_{\sqrt{\xi}}^{\infty} e^{-j\chi^2} d\chi,
\end{aligned}
\tag{1.20}
$$

where $\xi^{[i,r]} = \sqrt{2k\rho} \cos\frac{\phi^d \pm \phi^i}{2}$, E_z^i is the incident plain wave and ρ is the distance between the edge points and the observation point. ϕ_i and ϕ are the incident and diffraction angles, respectively. GTD can express diffraction effects with a high accuracy; however, it still has errors based on high-frequency approximation. The Physical Theory of Diffraction (PTD) has been proposed as a method to enhance the accuracy of the edge diffraction effects. This method can suppress the divergence at the shadow boundary (SB) or reflection boundary (RB) as shown in Fig. 1.8. It can deal with the caustic points by modifying the electric or magnetic current at the edge points. Fig. 1.9 shows the relationship between GO, PO, GTD and PTD. In general, the scale of assumed target shapes in our applications is less than the wavelength. Thus, there seems to be an ignorable error when applying these canonical problems. In Chapter 4, we present a simple waveform estimation based on Green's function integral, that solves this problem.

16
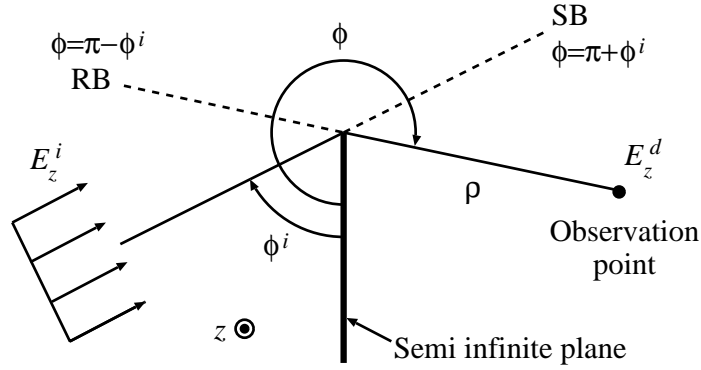
Figure 1.8: Canonical problem for the semi-infinite plane.
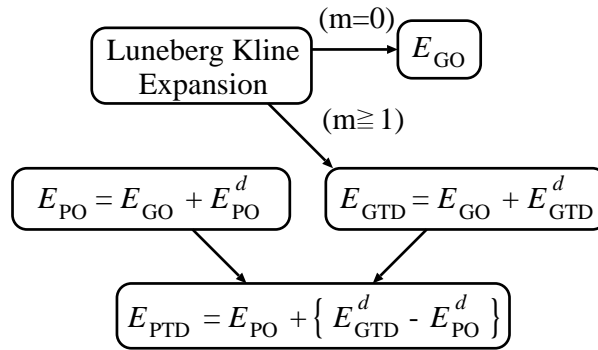
Figure 1.9: Relationship among GO, PO, GTD and PTD.

1.4 Inverse Problem for Proximity Imaging

Measurements or image reconstructions from observed data are called inverse problems in the mathematical field. Proximity imaging with radar is an example of these inverse problems. Radar systems have a big advantage over optical ones for higher-range resolution in imaging. However, this type of imaging has some problems described as follows. In this section, we specify the nature and characteristics of radar proximity imaging. We also describe Ultra Wideband signals, which enable us to deal with proximity imaging, and introduce our system configuration, pulse design and radar signal processing.

1.4.1 Ill-posedness

General radar systems dealing with proximity imaging assume antenna scanning or array antenna setting to obtain the received data. However, most of the non-destructive applications limit the baseline of antennas. This prevents us from obtaining received data
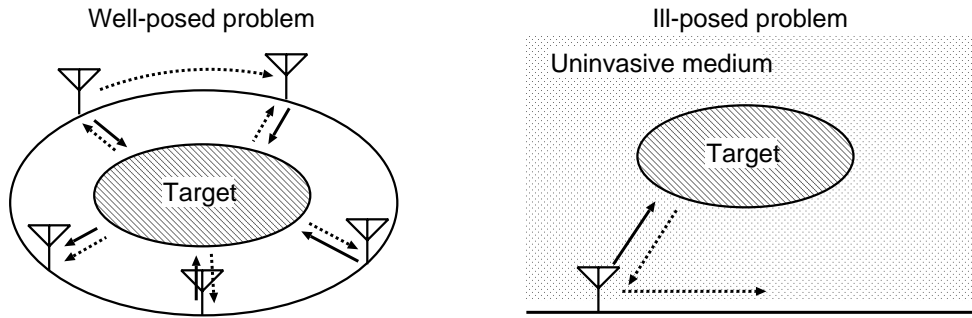
Figure 1.10: Examples of well-posed (left) and ill-posed (right) inverse problems.

from all the positions surrounding the assumed target. As a result, the observed data has insufficient information to reconstruct the target image completely. Image reconstruction with radar is therefore, well-known as an ill-posed inverse problem. The left and right hand side of Fig. 1.10 show examples of a well-posed and an ill-posed inverse problem, respectively. In the ill-posed problem, the distribution function of objects cannot be solved uniquely. Thus, we need to set several conditions for the assumed target model, such as uniform permittivity or a clear boundary. These conditions enable us to determine the boundary location of the target uniquely.

1.4.2 Ultra Wide-band Techniques

Conventional radar techniques assume far field investigations such as terrain surfaces, where the acceptable resolution is generally more than an order of 10m. The shorter pulse in the air causes interference to communication or broadcasting signals because it has large frequency bandwidth. In the past, the maximum frequency bandwidth of a transmitted signal in general radar systems was less than 10MHz which corresponds to 30m in the pulse wavelength. The range resolution of pulse radar is determined as a half of the wavelength, and thus the conventional signals never dealt with proximity imaging. In recent years, however, wideband signals have been approved and regulated as Ultra Wide-band (UWB) signals. In 2002, the Federal Communication Commission (FCC) regulated the 15 part rules concerning UWB signals. The Commission defined a UWB device for civilian purposes as one with,

- Fractional bandwidth is greater than 0.2 ,

- Bandwidth of signal is more than 500 MHz .

Fractional bandwidth and bandwidth were formulated by the Commission as $2(f_H - f_L)/(f_H + f_L)$ and $(f_H - f_L)$, respectively. Here f_H is the higher frequency of the -10 dB emission point and f_L is the lower frequency of the same emission point. Fig. 1.11
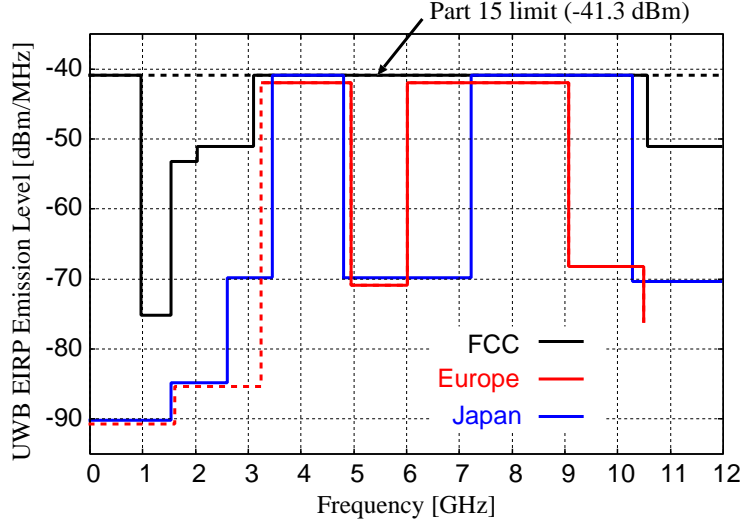
Figure 1.11: Comparison of EIRP limitations on UWB signals by each Commission.

shows the limitation on the EIRP (Equivalent Isotropically Radiated Power) of UWB signals by different Commissions. The power level of the upper boundary of EIRP is the same as that radiated by PC devices, so that it does not cause serious interference of other communication signals. Fig. 1.12 shows the comparison between a conventional radar pulse and a UWB signal. Thus, UWB signals give us a great advantage for high range-resolution, and enable us to deal with proximity imaging using radar.

1.4.3 Pulse Design and Signal Processing

In our system model, we utilize a mono-cycle pulse transmission at the current density, as shown in the left hand side of Fig. 1.13. The radiated electromagnetic field $E_z(\omega)$ in a 2-D problem is expressed as

$$E_z(\omega) \quad \propto \quad \sqrt{j\omega} I_z(\omega) H_0^{(2)}(k\rho) \tag{1.21}$$

where $I_z(\omega)$ is the excited current in the frequency domain. The right hand side of Fig. 1.13 shows the radiated waveform in the electronic field. The Wiener filter is well-known as an optimal filter for range measurement processing. The Wiener filter $W(\omega)$ is expressed as

$$W(\omega) = S_0 \frac{S(\omega)^*}{(1-\eta)S_0^2 + \eta|S(\omega)^2|} \tag{1.22}$$

where $S(\omega)$ is a reference signal in the frequency domain, and S_0 is a constant, which is determined by the regulation of the dimension in Eq. (1.22). We regulate the parameter η depending on the signal-to-noise ratio. In a noiseless situation, η is set to 0, which

19
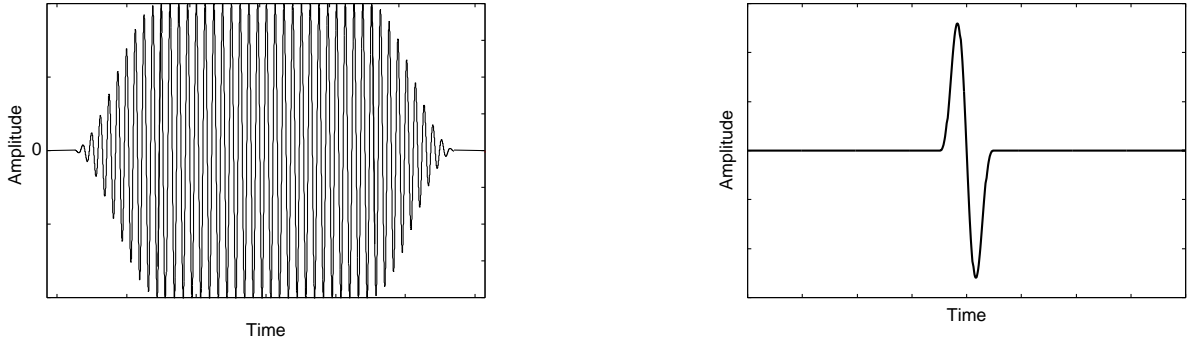
Figure 1.12: Conventional radio pulse (left) and UWB pulse (right).
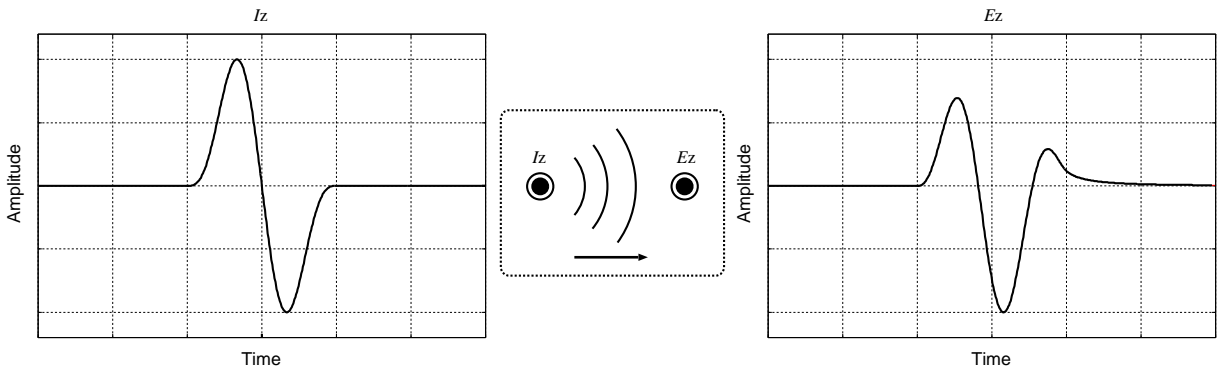
Figure 1.13: Induce current field (left) and electric field (right).

corresponds to the inverse filter. In a lower signal-to-ratio, η is set to 1, which correspond to the matched filter. Therefore, by considering the noise intensity, we can determine the optimal η in Eq. (1.22).

1.4.4 System Configuration

This section describes our system configuration and states several assumptions for the proximity imaging, which is dealt with in this thesis. Fig. 1.14 illustrates the assumed radar system. The transmitted signal is generated by a source generator and emitted through the antenna. The received data from the antenna is converted to digital data using an A-D converter and stored in memory. Then signal and image processing are applied to the received data. The application device, such as collision detection, defects detection, or target identification for example, can then be actuated with the information on the location or shape of the target.

We assume an omni-directional antenna, which radiate the radio wave as spherical
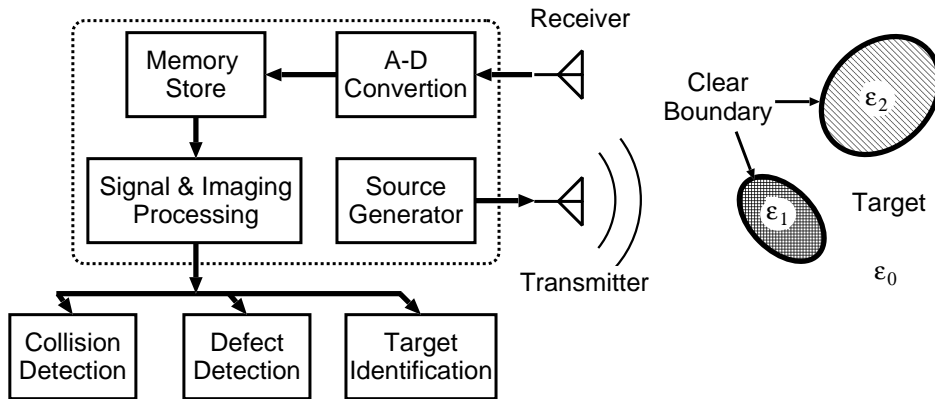
Figure 1.14: System configuration.

waves of the same intensity. It obtains the received signals by antenna scanning or array setting in a 2-D plain. It is assumed that the target has a uniform permittivity and clear boundary, the medium is homogeneous and the speed of the radio wave is known and constant as the speed of light.

1.4.5 Polarimetry Techniques

Polarimetry of scattered waves contains a significant information about the target, especially about the curvature or the major direction or shape of the target. In general, the scattered wave of the horizontal and vertical polarization, E_{H}^{s} and E_{V}^{s} are expressed as

$$\left[\begin{array}{c} E_{\mathrm{H}}^{s} \\ E_{\mathrm{V}}^{s} \end{array} \right] = \left[\begin{array}{cc} S_{\mathrm{HH}} & S_{\mathrm{HV}} \\ S_{\mathrm{VH}} & S_{\mathrm{VV}} \end{array} \right] \left[\begin{array}{c} E_{\mathrm{H}}^{i} \\ E_{\mathrm{V}}^{i} \end{array} \right] = \boldsymbol{S} \left[\begin{array}{c} E_{\mathrm{H}}^{i} \\ E_{\mathrm{V}}^{i} \end{array} \right] \tag{1.23}$$

where E_{H}^{i} and E_{V}^{i} are incident waves for each polarimetry, and $\boldsymbol{S}$ is called the scattering matrix. To monitor the scattering matrix, we obtain a various information about the characteristics of the target shape. Unifying the shape estimation and the polarimetry techniques shows great potential in proximity imaging.

1.5 Classical and Developed Works for Pulse Radars

1.5.1 Derivative Techniques from Synthetic Aperture Radar

Synthetic Aperture Radar is one of the most efficient and useful techniques in radar imagery [55–59]. It is aimed at terrain surfaces of agriculture forestry, soil, sea etc, and the derivative techniques of SAR have flourished from a geoscience sensing viewpoint [60–65]. We introduce several developed approaches based on SAR principles.

Polarimetric SAR (PolSAR) has an advantage in the classification of urban structures, natural distributed areas or land features [66–69]. It utilizes the polarimetric covariance $\boldsymbol{C}$ as $\boldsymbol{C} = \boldsymbol{SS}^*$, where $\boldsymbol{S}$ is the scattering matrix. To extract the information about the scattering mechanism with polarimetric data, PolSAR deals with the statics of SAR data such as the covariance matrix, Muller's matrix or a coherency matrix [70–73]. Polarimetric Entropy-Alpha evaluated by a coherency matrix was introduced by Cloud and Pottier [70]. Several decomposition techniques have been proposed to evaluate the polarimetric information including the model fitting method. Durden and Freeman have proposed a three-component scattering model which decomposes the measured covariance matrix into surface, double bounce and volume scattering contributions based on the physical scattering model [71]. Moriyama et al. developed this idea further to apply to the classification of urban structures using a suitable scattering model [74].

We now introduce one of the excellent surface classification methods with PolSAR based on Support Vector Machines(SVMs) [75]. To enhance the pattern recognition of the SAR image, this method utilizes SVMs together with the polarimetric data. SVMs utilize the linear classification function as the Optimal Separating Hyperplane (OSH), which can be determined by maximizing the margin in data mapping. The appeal of SVMs is found in their ability to handle linearly inseparable problems without difficulty, while the OSH is defined by a linear function. The principle of SVMs is that we separate the observed feature vectors, which is defined as $\boldsymbol{x}$ in n-dimensions, with the hyperplane $f(\boldsymbol{x})$ in training samples. The optimal hyperplane $f(\boldsymbol{x})$ is determined by maximizing the distance between the sample data and the separating hyperplane. The form of $f(\boldsymbol{x})$ is given by

$$f(\boldsymbol{x}) = \langle \boldsymbol{w}, \boldsymbol{x} \rangle + b, \quad (\boldsymbol{w} \in \boldsymbol{R}^n, \ b \in \boldsymbol{R}). \tag{1.24}$$

SVMs are a type of linear classifiers, which divides the feature space into two subspaces by the hyperplane $\langle \boldsymbol{w}, \boldsymbol{x} \rangle + b = 0$. The optimal separating hyperplane should satisfy the constrain condition $y_i(\langle \boldsymbol{w}, \boldsymbol{x} \rangle + b) \geq 1, \ (i = 1, \ldots, l)$, where l is the number of training samples. By utilizing the Lagrangian minimization, OSH is determined as

$$\mathrm{sgn}(f(\boldsymbol{x})) = \mathrm{sgn}\left(\sum_{i=1}^{l} \alpha_i y_i \langle \boldsymbol{x}_i, \boldsymbol{x} \rangle + b \right), \tag{1.25}$$

where the α_i is the Lagrange multiplier. The above OSH is a linear function; however, the general classification problems with PolSAR tend to be nonlinear. To overcome this nonlinearity, the kernel function approach can be used to transform the sampled data to the appropriate space with $\Phi(\boldsymbol{x})$ where a linear OSH exists. Applicable kernels are the Gaussian kernel and others. The effectiveness of the expanded algorithm has been verified in experimental studies on the classification of landscapes using multi-frequency polarization. However, this method assumes a far-field environment and requires training classifications with obtained data. Thus, it cannot be applied to near field target recognition, in which many different kinds of classifications are needed. In addition, by
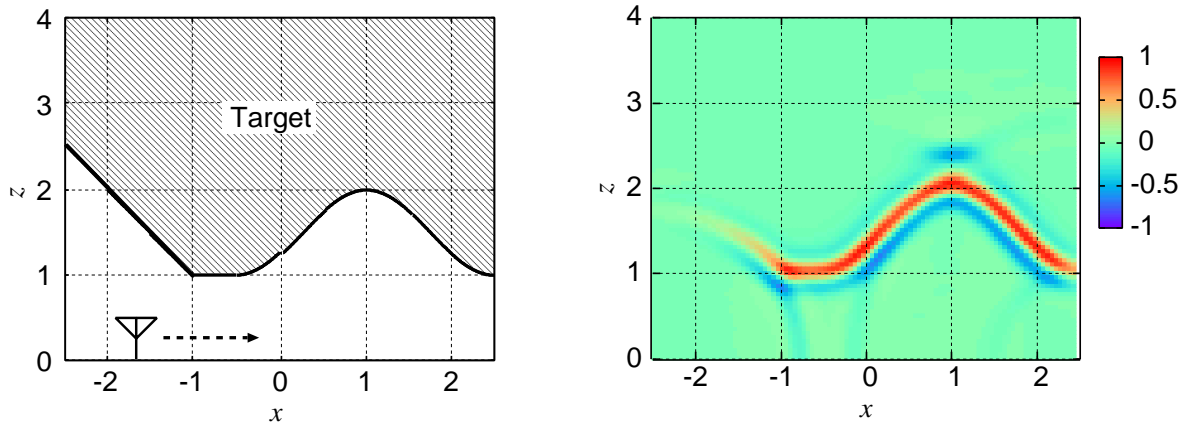
Figure 1.15: System model (left) and estimated image (right) with SAR.

combining the interferogram to PolSAR, PolInSAR methods have been developed [76–80]. These utilize the phase differences between two paired pixels of two complex SAR images obtained from the data collected by two antennas. Combining this classification algorithm with proximity imaging appears promising.

Proximity imaging with SAR has been applied to Ground Penetrating Radar for embedded landmines and medical imaging to detect tumors in human tissue. The principles of proximity SAR are summarized as follows. The left hand side of Fig. 1.15 shows the system model. The omni-directional antenna is scanned along the x axis. We obtain the distribution image in the real space $S(x, z)$ from

$$S(x, z) = \int_{-\infty}^{\infty} s \left(X, \sqrt{(X - x)^2 + z^2} \right) dX, \tag{1.26}$$

where $s(X, t)$ is defined as the output of the matched filter in time t at the antenna location $(x, z) = (X, 0)$. The space is normalized with the center wavelength of the transmitted pulse. On the right hand side of Fig. 1.15 the estimated image with SAR is shown, and we identify the target boundary from the highest intensity. However, the resolution around the target is insufficient to recognize a clear boundary, especially along edge regions. Furthermore, this method requires a total search of the assumed region, and the calculation time is more than 60 sec using a 3.2 GHz Xeon processor. As such it cannot be applied to real-time operations.

1.5.2 Inverse Scattering with Domain Integral Equation

As described in Sec 1.3.3, the direct problems in given boundary conditions can be recast as domain integral equations. Inverse scattering approaches have been developed to solve the domain integral equations for buried dielectric objects underground and for human

23

tissue [81–85]. Here, we explain the basic approach to the inverse scattering problems [86]. Let us consider a 2-D scalar configuration, where an incident TM-polarized time-harmonic incident wave illuminates the target with an arbitrary cross-section Θ. The target is expressed as object function $\tau(x,y)$,

$$\tau(x,y) = \begin{cases} \epsilon_r - 1 - \mathrm{j}(\sigma(x,y)/\omega\epsilon_0) & (x,y) \in \Theta, \\ 0 & \text{otherwise,} \end{cases} \qquad (1.27)$$

where ϵ_r and σ are the dielectric permittivity and conductivity of the target, respectively. The inverse problem consists of retrieving the object function from the resulting measured electric field, which is defined as $F(x,y)$. We set receivers around D in the observation domain O. This problem can be expressed by the following integral equations.

$$F_{\text{scat}}^{(v)}(x,y) = k_0^2 \int_D G_0(x,y,;x',y')F^{(v)}(x',y')\tau(x',y')\mathrm{d}x\mathrm{d}y, \quad (x,y) \in O, \quad (1.28)$$

$$F_{\text{inc}}^{(v)}(x,y) = F^{(v)}(x,y) - F_{\text{scat}}^{(v)}(x,y), \quad (x,y) \in D, \qquad (1.29)$$

where F_{scat}^v and F_{inc}^v are the scattered and incident fields, respectively, and G_0 is the free-space Green function in 2-dimensions. We discretize the unknown function with the linear combination of the rectangular basis function $R_n(x,y), (n=1,\dots,N)$ as

$$\tau(x,y) = \sum_{n=1}^{N} \tau_n R_n(x,y) \quad (x,y) \in D, \qquad (1.30)$$

$$F^{(v)}(x,y) = \sum_{n=1}^{N} \psi_n^{(v)} R_n(x,y) \quad (x,y) \in D. \qquad (1.31)$$

Then, the inverse problem is recast as the global minimization of the cost function Φ

$$\Phi(\underline{f}) = \alpha_{\text{Data}} \frac{\sum_{m=1}^{M} \sum_{v=1}^{V} \left| F_{\text{scat}}^{(v)}(x_m,y_m) - \mathcal{F}_{\text{Data}}(\tau_n, \psi_n^{(v)}) \right|^2}{\sum_{m=1}^{M} \sum_{v=1}^{V} \left| F_{\text{scat}}^{(v)}(x_m,y_m) \right|^2}$$

$$+ \alpha_{\text{State}} \frac{\sum_{q=1}^{N} \sum_{v=1}^{V} \left| F_{\text{inc}}^{(v)}(x_q,y_q) - \mathcal{F}_{\text{State}}(\tau_n, \psi_n^{(v)}) \right|^2}{\sum_{q=1}^{N} \sum_{v=1}^{V} \left| F_{\text{inc}}^{(v)}(x_q,y_q) \right|^2}, \qquad (1.32)$$

where $\underline{f} = \{\tau_n, \psi_n^{(v)}; n = 1,\dots; v = 1,\dots,V\}$, M is the number of points of the observation domain, where F is measured; $\mathcal{F}_{\text{Data}}$ and $\mathcal{F}_{\text{State}}$ indicate the discretized forms of the right hand side terms in Eqs. (1.28) and (1.29), respectively. α_{Data} and α_{State} are regularization parameters, which are determined as 1.0 with normalization. Since the global minimization method of the cost function Φ corresponds to a kind of multidimensional optimization problem, a Generic Algorithm (GA) is commonly used to avoid the local optimization [87,88]. However, GA is quite time-consuming, and cannot be applied

to real-time operations. A parallel GA method is, however, effective for real-time imaging [86]. This method utilizes 25 computers, each of which is a 1.7 GHz Intel Pentium IV with 256 MB of RAM. Although we can realize real-time imaging with these parallel implementations, the image resolution is insufficient, as this is highly dependent on the discretization size of the space domain. For example, 20×20 divisions of the space is the upper limit for any real-time operation, and this is not suitable for out assumed applications.

1.5.3 Diffraction Tomography Algorithm

Microwave tomography has been developed using the same principles as CT with X-ray waves, and this is promising for accurately locating a target in the air or underground. The transmitted signals of radio wave are, in general, scattered in all directions, with the result that we can receive the diffraction echoes at any observation point. The diffraction tomography algorithm utilizes this principle, and has been developed for microwave imaging in the near field.

Developed image-reconstruction methods for microwave tomography can be divided into two groups. The first group represents the approximation methods such as Born or Rytov. The latest iterative modifications have proven very fast and reliable for imaging low and medium dielectric-contrast objects. However, these methods have limited application in finding reliable biological solutions to nonlinear ill-posed mathematical problems of microwave tomography, especially when imaging high dielectric contrast objects. The second group consists of non approximation methods. These methods, proven to be much more accurate, are however, expensive in terms of computer resources [89]. The cross-hole radar tomography algorithm has been developed as a quasi linear approximation of this problem [90]. This method does not require an iterative approach and can be applied to multiple sources as follows. The scattered electric field is expressed by the domain integral equation as

$$E_s(\boldsymbol{r}_s, \boldsymbol{r}_r) = -K_0^2 \int G(\boldsymbol{r}_1, \boldsymbol{r}_r) O(\boldsymbol{r}_1) E(\boldsymbol{r}_s, \boldsymbol{r}_1) \mathrm{d}\boldsymbol{r}_1 \tag{1.33}$$

where $E_s(\boldsymbol{r}_s, \boldsymbol{r}_r)$ is a scattered electric field where $\boldsymbol{r}_s$ and $\boldsymbol{r}_r$ are the location of the source and receiver, respectively. K_0 is the wave number of the background medium, $E(\boldsymbol{r}_s, \boldsymbol{r}_1)$ is the electric field at $\boldsymbol{r}_1$, $G(\boldsymbol{r}_s, \boldsymbol{r}_r)$ is Green's function in free space, and $O(\boldsymbol{r})$ is the object function, which expresses the distribution of the target and is zero outside the target. To solve this non-linear integral equation, this method utilizes the quasi linear approximation as

$$E_s(\boldsymbol{r}_s, \boldsymbol{r}_r) \simeq -k_0^2 \int G(\boldsymbol{r}_1, \boldsymbol{r}_r) O'(\boldsymbol{r}_1) E_0(\boldsymbol{r}_s, \boldsymbol{r}_1) \mathrm{d}\boldsymbol{r}_1 \tag{1.34}$$

$$\lambda(\boldsymbol{r}) \simeq -k_0^2 \int G(\boldsymbol{r}_1, \boldsymbol{r}) \tag{1.35}$$
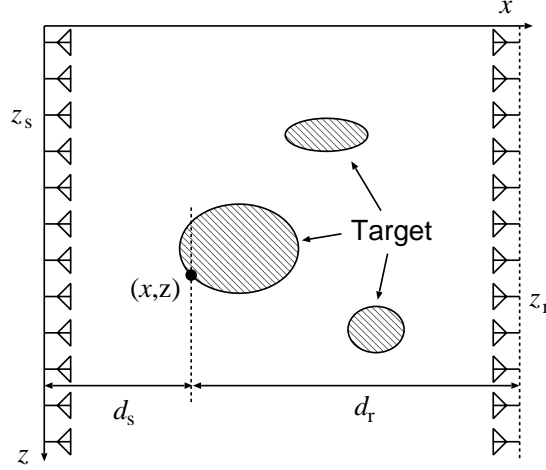
Figure 1.16: Cross hole configuration for diffraction tomography.

where $\lambda(\boldsymbol{r})$ known as the scattered coefficient, is defined as $E_s(\boldsymbol{r}_s, \boldsymbol{r}_1)/E_0(\boldsymbol{r}_s, \boldsymbol{r}_1)$, and $O'(\boldsymbol{r}_1) = O(\boldsymbol{r}_1)(1 + \lambda(\boldsymbol{r}_1))$ holds. $E_0(\boldsymbol{r}_s, \boldsymbol{r}_1)$ is the incident electric field.

We assume a 2-D cross hole configuration as shown in Fig. 1.16. The horizontal coordinates of the source and receiver are assumed to be constant, so that we can substitute $\boldsymbol{r}_s$ and $\boldsymbol{r}_r$ with z_s and z_r, respectively. By utilizing the tomography principles, $O'(x, y)$ is expressed with the Fourier transform as

$$
\begin{aligned}
O'(x, z) &= \frac{1}{\pi^2} \int_{-\pi}^{\pi} \int_{-\pi}^{\pi} \frac{|k_s \gamma_r + k_r \gamma s|}{k_0^2} \widetilde{E}_s(k_s, k_r) \\
&\quad \cdot e^{-j(\gamma_r d_r - \gamma_s d_s)} e^{j[(\gamma_r - \gamma_s)x + (k_s + k_r)z]} dk_s dk_r
\end{aligned}
\tag{1.36}
$$

where $\widetilde{E}_s(k_s, k_r)$ is the Fourier transform of $E_s(z_s, z_r)$, and k_s and k_r, d_s and d_r are the wave number and distance of the source and receiver, respectively. Also $\gamma_s = \sqrt{k_0^2 - k_s^2}$ and $\gamma_r = \sqrt{k_0^2 - k_r^2}$ hold. By calculating $\lambda(\boldsymbol{r})$ and $O'(\boldsymbol{r})$, we obtain the target distribution function as $O(\boldsymbol{r})$. Although this method can realize robust, fast imaging for multiple source environments, we must arrange the antennas in all regions surrounding the target.

Many studies have focused on diffraction tomography with radar systems. These include buried objects imaging aimed at subsurface imaging in GPR [91,92], through wall imaging [93], and biological tissues imaging [94]. Where there is insufficient received data, data interpolation in the wave number domain has also been proposed [95]. Although other kinds of diffraction tomography have been developed [96–98], they have serious problems with respect to calculation time and in the scanning limitation for proximity imaging, where vehicles require forward imaging to avoid collisions.

1.5.4 Model Fitting Algorithm

Many different model based imaging algorithms have been studied. These methods utilize data matching between the measured received signals and those previously calculated for various target models. To obtain the optimal target model, an optimization algorithm, based on the conjugate gradient method or Generic Algorithms has been developed [99–101]. It has been applied to conductors buried underground as GPR applications [102–104]. One of the most accurate methods, is the discrete model fitting algorithm [105]. This method assumes a lossy and dispersive medium, and accomplishes a robust imaging even in highly cluttered situations. The principle of this method is summarized as follows. $\boldsymbol{X}$ is defined as the parameter which, expresses the characteristic of the surface points and medium of the target. $e_i(t)$ is defined as the received electric field in the time domain for the i th antenna. $e_i(t; \boldsymbol{X})$ is expressed as the calculated received signal in the case of the model parameter $\boldsymbol{X}$. We determine the parameter $\boldsymbol{X}$ as

$$\boldsymbol{X} = \arg \min_{\boldsymbol{X}} \sum_{i=1}^{N} [e_i(t) - e_i(t; \boldsymbol{X})]^2. \tag{1.37}$$

where N is the total number of the observation points. In general, $e_i(t; \boldsymbol{X})$ is non-linear function about $\boldsymbol{X}$, and can be approximated with the linear function

$$e_i(t; \boldsymbol{X_0} + \Delta \boldsymbol{X}) \simeq e_i(t; \boldsymbol{X_0}) + \Delta \boldsymbol{X} \cdot \frac{\partial}{\partial \boldsymbol{X}} e_i(t; \boldsymbol{X}). \tag{1.38}$$

We determine the optimal model parameter with this linear function, using the linear least square method. This method can realize buried pipe imaging with the accuracy within 0.2λ with 5 iterations. However, the degree of freedom for the assumed models is relatively high, and in the case that an inappropriate initial value is given, the estimated image hardly converges to the true shape. Moreover, in this case, the method requires intensive computation, which is not suitable for the assumed applications.

1.5.5 Migration Algorithm

The range migration method has been applied to seismic analysis. It can detect the source of an earth quake by obtaining the received echoes at many observation points. Radar systems based on the migration principle, and targeting embedded objects or the earth's surface, have been developed [106–108]. A breast cancer detection method has also been developed for biomedical applications [109]. Greenhalgh et al. have developed an accurate surface imaging for GPR radar or Georadar [110–112] As far field applications, space debris detection and land space imaging have been developed [113,114]. A matched filter based migration method has been proposed, which is modified to deal with the vector wave [115]. For detecting early stage breast cancer, microwave imaging via space-time (MIST) beamforming has been proposed by S.C. Hagness et al. [116–120]. This method
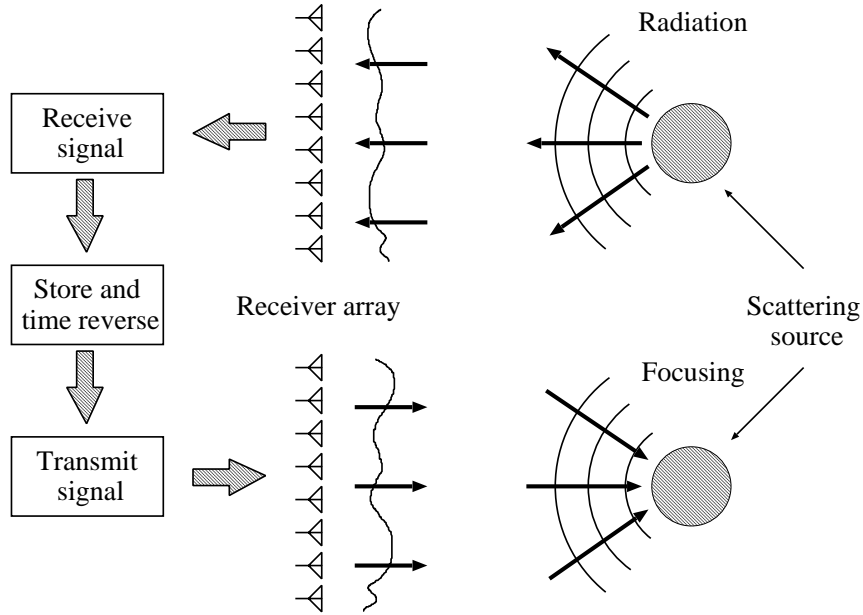
Figure 1.17: Schematic of time reversal algorithm.

utilizes the UWB signals for high-resolution imaging. It achieves spatial focus by first time shifting the received signals to align the returns from the assumed scatterer at a candidated location.

Time Reversal Algorithm

The time reversal method has recently received much attention, and as such is one of the most well-used algorithms based on migration. It has been developed for the detection, in cluttered environments, of buried objects [121–123] or in medical imaging of breast cancer detection [124, 125]. Much research has been carried out using this algorithm for underground imaging and detection, forest communications and hardware realization of the time reversal mirror. Here, we introduce the multiple objects localization algorithm in highly cluttered environments [126]. The time reversal method utilizes the reciprocity of wave propagation in a time-invariant medium. Fig. 1.17 shows the basic principle of this method. A time-domain source emits a signal received by a transmitter and receiver array. The signals are reversed in time and radiated into the domain. In a domain with significant multi-path, a large effective aperture is realized, and space-time focusing is introduced at the original source. We consider a single target situated in a time-invariant cluttered background. Assume a linear array of K receivers, with the k th receiver located at $\boldsymbol{r}_k$, and a single source located at $\boldsymbol{r}_s$. The target is treated as M stationary scattering centers. Assume that a time domain pulse $p(t)$ is emitted from the transmitter at $\boldsymbol{r}_s$. The

fields incident on the target at $\boldsymbol{r}'$ due to the source are represented as

$$E(\boldsymbol{r}, t) = p(t) * G_e(\boldsymbol{r}', \boldsymbol{r}_s, t) \tag{1.39}$$

where $G_e(\boldsymbol{r}', \boldsymbol{r}_s, t)$ is the Green's function representative of a source emitting in the presence of the clutter item and $*$ is the convolution operator. The scattered electric field at the k th receiver $U_k(\omega)$ is expressed as with the Born and the high-frequency approximation,

$$U_k(\omega) \simeq \sum_{m=1}^{M} B_m(\boldsymbol{r}') P(\omega) G_e(\boldsymbol{r}'_m, \boldsymbol{r}_s) G_e(\boldsymbol{r}_k, \boldsymbol{r}'_m). \tag{1.40}$$

where $B_m(\boldsymbol{r}'_m)$ is a function that represents the conversion of excitation field $E(\boldsymbol{r}', t)$ into equivalent currents that re-radiate as secondary sources. For each receiver, we calculate the time-reversal signals as $I_k(\boldsymbol{r}, t)$

$$I_k(\boldsymbol{r}, t) = \int \left[\sum_{m=1}^{M} B_m(\boldsymbol{r}') P(\omega) G_e(\boldsymbol{r}'_m, \boldsymbol{r}_s) G_e(\boldsymbol{r}_k, \boldsymbol{r}'_m) \right]^* G_c(\boldsymbol{r}, \boldsymbol{r}_k) G_c(\boldsymbol{r}_s, \boldsymbol{r}) \mathrm{e}^{\mathrm{j}\omega t} \mathrm{d}\omega, \tag{1.41}$$

where the subscript c emphasizes that Green's functions are computed within the imaging process. By summing all K receivers, $I(\boldsymbol{r}, t) = \sum_{k=1}^{K} I_k(\boldsymbol{r}, t)$, and calculating the total field at time $t = 0$, which corresponds to the time of arrival from the target, the time reversal image can be focused on the true target image.

This method can achieve clear image in a highly cluttered environment, by choosing an appropriate Green's function. Additionally, it can be applied to detect a breast cancer tumor in an inhomogeneous and cluttered environment. However, the time reversal procedures require intensive computation as the calculations for these are based on, for example, the ray-tracing method. Additionally, the resolution and robustness depend highly on the selection of Green's function, and it is hard to accomplish high-resolution imaging, where various target models or environments can be assumed.

1.5.6   SEABED

While many imaging algorithms have been proposed for radar systems, they mostly require intensive computation, and are limited to assumed target models. As a solution of these problems, SEABED (Shape Estimation Algorithm based on BST and Extraction of Directly scattered waves) offers high-speed, non-parametric imaging for UWB pulse radars [127–131]. It is based on a reversible transform BST (Boundary Scattering Transform) between the received signals and the target shape and can specify the target surface locations accurately. A description of the principles and characteristics of this algorithm follows.

We deal with 3-D problems, and assume that the target has clear boundaries. A mono-static radar system and homogeneous medium are assumed. The induced current
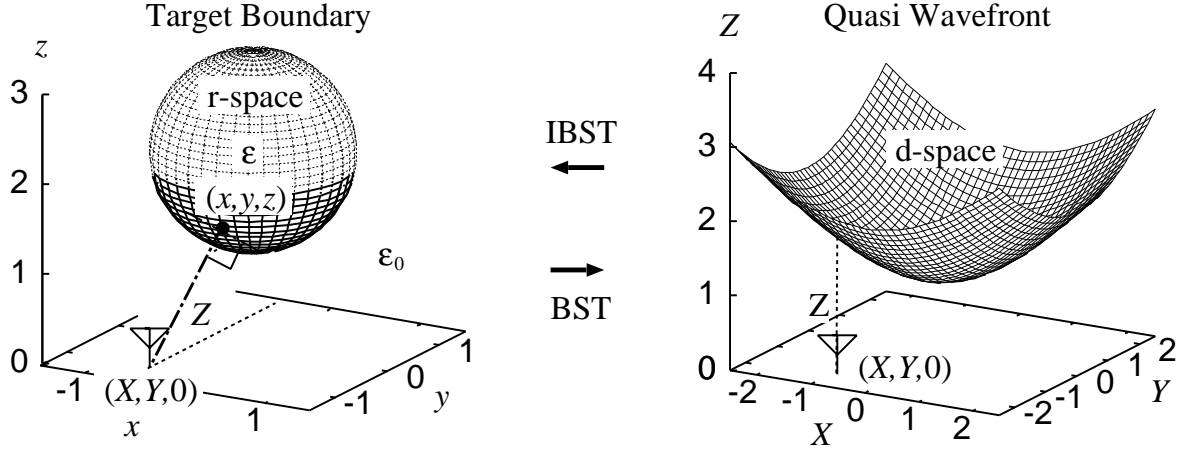
Figure 1.18: Relationship between r-space and d-space.

at the transmitting antenna is a mono-cycle pulse. R-space is defined as the real space where targets and antennae are located, and is expressed by the parameters (x, y, z). An omni-directional antenna is scanned on the $z = 0$ plane, and for simplicity, $z > 0$ is assumed. $s'(X, Y, Z')$ is defined as the received electric field at the antenna location $(x, y, z) = (X, Y, 0)$, where $Z' = ct/(2\lambda)$ is expressed by the time t and the speed of the radio wave c. $s(X, Y, Z')$ is defined as the output of the filter. We extract the significant peaks of $s(X, Y, Z')$ as Z for each X and Y, and extract the surface (X, Y, Z), which is called a quasi wavefront. D-space is defined as the space expressed by (X, Y, Z). SEABED utilizes a reversible transform BST between the point (x, y, z) of r-space and the point (X, Y, Z) of d-space . BST is expressed as

$$\left. \begin{array}{rcc} X & = & x + z\partial z/\partial x \\ Y & = & x + z\partial z/\partial y \\ Z & = & z\sqrt{1 + (\partial z/\partial x)^2 + (\partial z/\partial y)^2} \end{array} \right\}. \tag{1.42}$$

IBST (Inverse BST) is expressed as

$$\left. \begin{array}{rcc} x & = & X - Z\partial Z/\partial X \\ y & = & Y - Z\partial Z/\partial Y \\ z & = & Z\sqrt{1 - (\partial Z/\partial X)^2 - (\partial Z/\partial Y)^2} \end{array} \right\}, \tag{1.43}$$

where $(\partial Z/\partial X)^2 + (\partial Z/\partial Y)^2 \leq 1$ holds. This transform is reversible, and gives us a strict solution for the inverse problem. Fig. 1.18 shows the relationship between r-space and d-space. IBST utilizes the characteristic that an incident wave is intensively reflected in the normal direction. SEABED has a great advantage in that it can estimate the target boundary directly from the received data with a non-parametric approach. The

most appealing part of the SEABED algorithm is the direct imaging with the simple transform. This cannot be realized with the conventional methods. A discretized model of BST has previously been developed [120], however, discretized errors still appear in the target boundary estimation. On the contrary, SEABED enables us to estimate the target boundary perfectly, if we extract the true quasi wavefront from the received data. However, SEABED itself has several problems in terms of stability, accuracy and others. In this thesis, we develop a new imaging algorithm based on this model to accomplish high-performance imaging.

1.6   Contribution of the Present Work

The main contribution of the present work is a high-performance imaging algorithm for UWB pulse radar systems. In this thesis, we investigate the characteristics of the SEABED algorithm in detail, and propose a new imaging algorithm, which can solve several problems inherent in SEABED.

Chapter 2 describes an imaging algorithm with linear array antennas to realize high-speed data acquisition. SEABED assumes 2-D scanning of the mono-static antenna, and therefore data acquisition takes an excessively long time. To shorten this time, we constitute a 1-D linear array. However, the resolution of the image with SEABED in a linear array, is limited to the interval of the array antennas. In a real environment, the interval of the array should be more than one half of the wavelength of the transmitted pulse to avoid the mutual couplings. To enhance finer resolution, we extend a reversible transform BST in a bi-static radar system. By applying the extended BST to linear array antennas, we can increase the estimated points to the number of combinations of the array antennas. Accordingly, we can realize high-resolution 2-D and 3-D imaging without increasing the number of samples in the numerical simulations and experiment.

Chapter 3 presents a new imaging algorithm with an envelope of circles or spheres, which can realize robust, fast imaging. Another serious problem with SEABED is its instability in noisy environments This is as a result of utilizing the derivative of the received data in BST. The fluctuation of the estimated image is readily enhanced by the white noise with derivative operations. As means of solving this problem, adaptive smoothing algorithms have been developed [130, 131]. However, the resolution of images with these methods depends on the correlation length of the data smoothing, and there is a trade-off between resolution and stability. The proposed imaging algorithm with an envelope of spheres without derivative operations, essentially removes this trade-off. Our method is based on the principle that the target boundary can be expressed as an envelope of spheres, whose center is the antenna location and whose radius is the distance. It also proves that the target boundary can be expressed as the boundary points of the union or intersection set of spheres by considering the circumscription and inscription to the target boundary. This algorithm can realize robust, fast 3-D imaging and completely solves the

trade-off.

Chapter 4 describes the high-resolution, accurate imaging algorithm based on waveform estimation. It is confirmed that the estimated image with an envelope of spheres is distorted around the target edges even in a noiseless environment. This is caused by the error of the extracted wavefront due to the scattered waveform deformations. To enhance finer resolution and accuracy, we propose an imaging algorithm that iterates the shape and waveform estimation recursively. In 2-D problems, we propose a simple, fast waveform estimation, which does not sacrifice the speed of shape estimation. By utilizing this algorithm in numerical simulations and experiments, we confirm that it can realize high-resolution and accurate imaging including around target edges. However, in 3-D problems, the calculation time of the waveform estimation is not negligible. In this chapter, we develop a new real-time, high-performance imaging algorithm with the spectrum offset correction. In this algorithm, we ensure that the scattered waveform resembles the transmitted one, and we succeed in compensating for the range errors with the center frequencies shift. Thus, this method accomplishes high-performance 3-D imaging, and satisfies, to a high degree, several of the required performances criteria.

Concluding remarks are given in Chapter 5. We give a general evaluation of our proposed methods, and indicate future developments for radar proximity imaging.

Chapter 2

High-Resolution Imaging Algorithm with Linear Array Antennas

2.1 Introduction

We have already proposed a high-speed 3-D imaging algorithm SEABED, which utilizes a reversible transform BST between the time delays and the target boundary. This method accomplishes a direct and non-parametric imaging with the received data. However, it requires large time for data acquisition because it needs for a 2-D scanning of the mono-static radar. We constitute a linear array antenna and scan it along a straight line to avoid this difficulty. However, the interval of the array should be set to more than a half of the center wavelength of the pulse to avoid mutual couplings. Therefore, the number of the antennas should be small. Also the resolution of the image with the conventional SEABED is limited with the number of the antennas because BST is applied only to mono-static radars. In this paper, we extend BST to a bi-static model. We propose a fast and high-resolution imaging algorithm without increasing the number of the antennas by applying the extended BST to the linear array. First, we show the method and examples for 2-D problem for simplicity. This method is readily extended to 3-D problem, and we show the performance evaluation with numerical simulations and experiments.

2.2 2-D Problem

2.2.1 System Model

We show the system model in Fig. 2.1. We deal with 2-D problems and TE mode waves for simplicity. We assume that the target has uniform permittivity and is surrounded by a clear boundary that is composed of smooth curves concatenated at discrete edges. We assume that the propagation speed of the radiowave is constant and known. The induced
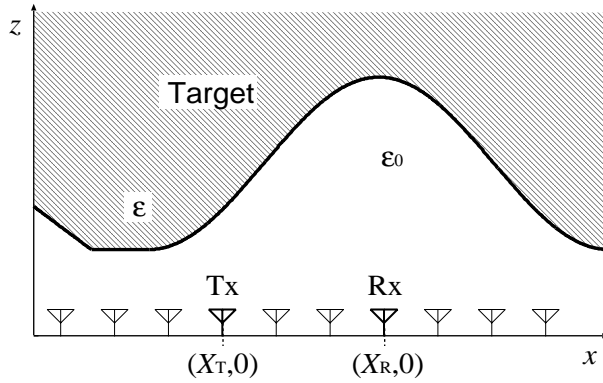
Figure 2.1: System model in 2-D problem.

current at the transmitting antenna is a mono-cycle pulse. We utilize omni-directional antennas and locate them with a fixed interval along x axis.

R-space is defined as the real space, where targets and the antenna are located, and is expressed with the parameters (x, z). Both x and z are normalized by λ, which is the center wavelength of the transmitted pulse in the air. We assume $z > 0$ for simplicity. The locations of the transmitting and the receiving antennas are defined as $(x, z) = (X_{\mathrm{T}}, 0)$ and $(X_{\mathrm{R}}, 0)$, respectively. $s'(X_{\mathrm{T}}, X_{\mathrm{R}}, Z')$ is defined as the received electric field where we set the transmitted and received antennas as $(X_{\mathrm{T}}, 0)$ and $(X_{\mathrm{R}}, 0)$, respectively. We also define Z' with time t and speed of the radio wave c as $Z' = \mathrm{c}t/2\lambda$. $s(X_{\mathrm{T}}, X_{\mathrm{R}}, Z')$ is defined as the output of the matched filter with the transmitted waveform. We extract the significant peaks of $s(X_{\mathrm{T}}, X_{\mathrm{R}}, Z')$ for each X_{T} and X_{R} and define those peak points as $(X_{\mathrm{T}}, X_{\mathrm{R}}, Z)$. D-space is defined as the space expressed by $(X_{\mathrm{T}}, X_{\mathrm{R}}, Z)$, and we call it a quasi wavefront. The transform from d-space to r-space corresponds to the imaging.

2.2.2 Problem in Mono-Static Radar

We have already developed a high-speed imaging algorithm that we term SEABED. This method utilizes a mono-static radar, and defines as $X = X_{\mathrm{T}} = X_{\mathrm{R}}$. It clarifies the existence of a reversible transform BST between the target boundary (x, z) and the quasi wavefront (X, Z) [127]. BST is expressed as

$$\left. \begin{array}{rcl} X &=& x + z\partial z/\partial x \\ Z &=& z\sqrt{1 + (\partial z/\partial x)^2} \end{array} \right\}. \tag{2.1}$$

IBST (Inverse BST) is expressed as

$$\left. \begin{array}{rcl} x &=& X - Z\partial Z/\partial X \\ z &=& Z\sqrt{1 - (\partial Z/\partial X)^2} \end{array} \right\}, \tag{2.2}$$

34

where $|\partial Z/\partial X| \leq 1$ holds. This transform gives us a strict solution for the inverse problem. We extract the part of quasi wavefront as (X, Z) from (X_T, X_R, Z), where $X = X_T = X_R$ satisfies. A target image is directly estimated by applying the IBST to the quasi wavefront. Although this method realizes a high-speed imaging, the resolution of the image is limited by the number of the antennas because it assumes a mono-static radar. Fig. 2.2 shows the relationship between the estimated points with this model and antenna locations. As shown in Fig. 2.2, the estimated image has insufficient resolution. If we increase the number of scanning samples to enhance the resolution, data acquisition needs long time. Accordingly, there is a trade-off between the time taken to obtain the data and the resolution of the estimated image.

2.2.3 Boundary Scattering Transform for Bi-Static Radar

To resolve the problem as described in the previous section, we propose a fast and high-resolution imaging method with linear array antennas. First, we introduce a reversible transform BST for bi-static radars. We fix the interval of the transmitted and received antennas, and set it to $2d$. X is defined as $X = (X_T + X_R)/2$. The scattering center on the target boundary is defined as (x, z). Z is the distance to the scattering point, where the law of reflection is satisfied. Fig. 2.3 shows the relationship between the target boundary and a part of the quasi wavefront. With this geometrical condition, (X, Z) is expressed as

$$\left. \begin{aligned} X &= x + \frac{2z_x(z^2 + d^2)}{z(1 - z_x^2) + \sqrt{z^2(1 + z_x^2)^2 + 4d^2 z_x^2}} \\ Z &= \sqrt{z^2 + d^2 + zz_x(X - x)} \end{aligned} \right\}, \tag{2.3}$$

where $z_x = \partial z/\partial x$. We call this transform BBST (Bi-static BST). (x, z) is also expressed as

$$\left. \begin{aligned} x &= X - \frac{2Z^3 Z_X}{Z^2 - d^2 + \sqrt{(Z^2 - d^2)^2 + 4d^2 Z^2 Z_X^2}} \\ z &= \frac{\sqrt{Z^2 - d^2}}{Z}\sqrt{Z^2 - (x - X)^2} \end{aligned} \right\}, \tag{2.4}$$

where $Z_X = \partial Z/\partial X$. We call this transform IBBST (Inverse BBST). The derivations of Eqs. (2.3) and (2.4) are given in Appendix A.1. IBBST is effective for real-time imaging, as we can directly estimate the target boundary by using this transform with bi-static radars.

We apply IBBST to the linear array antennas as described in the following procedures. We define the number of antennas as N_X and the interval of the array antennas as ΔX. First, $k = 0$ is set.

Step 1). Apply the matched filter to $s'(X_T, X_R, Z')$, and obtain the output as $s(X_T, X_R, Z')$.

Step 2). Extract the quasi wavefront as (X_T, X_R, Z) by connecting the peaks of $s(X_T, X_R, Z')$.
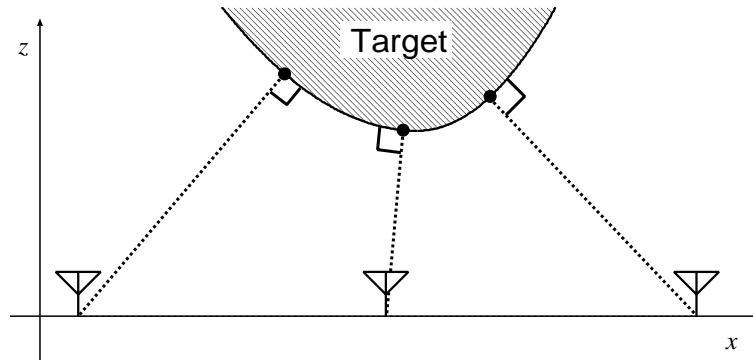
Figure 2.2: Relationship between estimated points and antenna locations of the mono-static model.
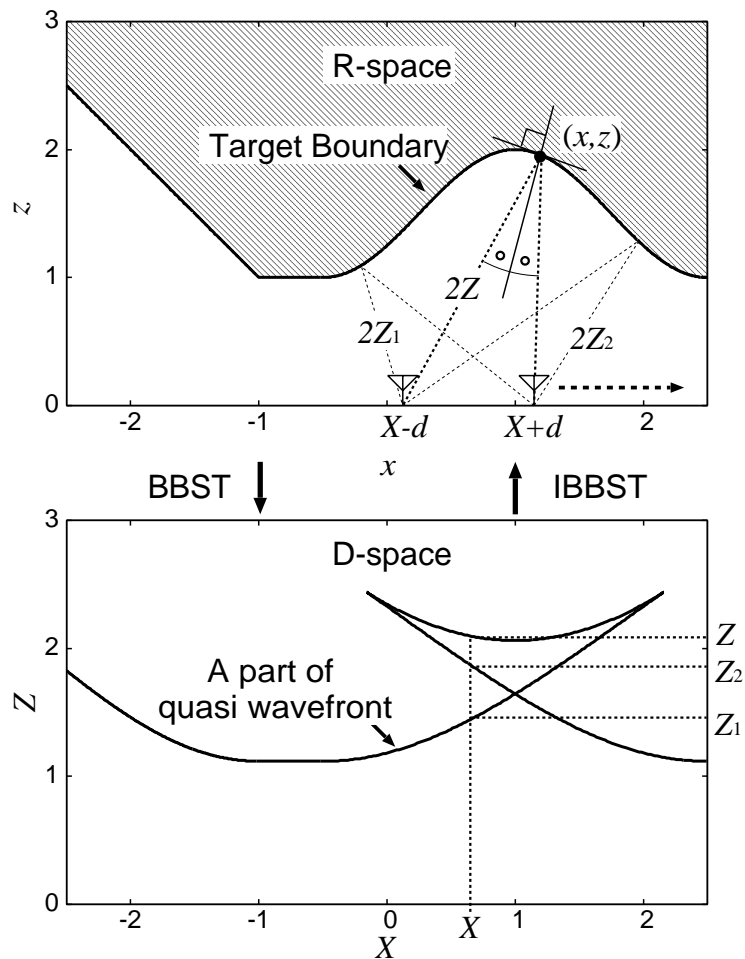
Figure 2.3: Relationship between the target boundary and the part of quasi wavefront in bi-static radars.
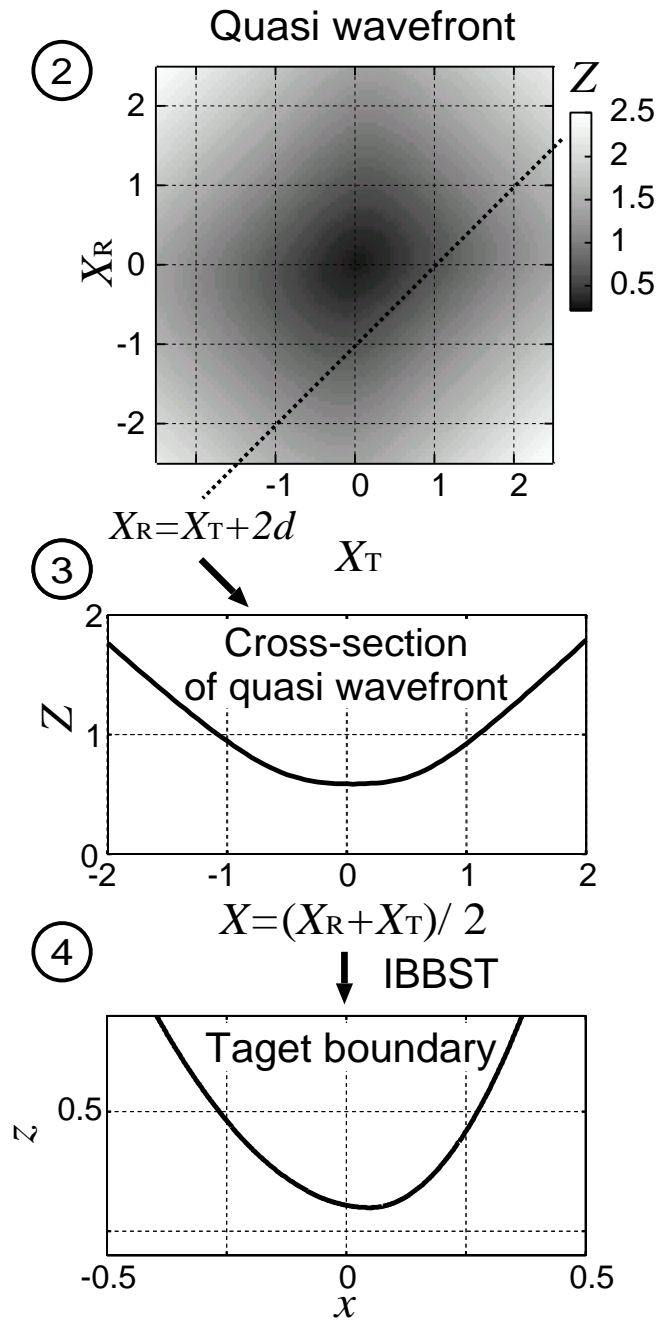
Figure 2.4: Quasi wavefront (upper), cross section of the quasi wavefront (middle) and target boundary (lower).
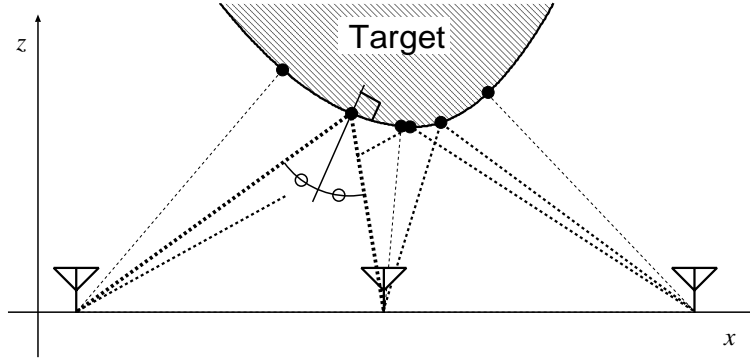
Figure 2.5: Relationship between estimated points and antenna locations of the bi-static model.

Step 3. Set $2d = k\Delta X$ and extract a cross section of the quasi wavefront as (X, Z), where $X = (X_\mathrm{T} + X_\mathrm{R})/2$ and $X_\mathrm{R} = X_\mathrm{T} + 2d$ hold.

Step 4). Apply IBBST to the extracted curve (X, Z) and obtain a target image.

Step 5). Set $k = k + 1$. If $k \leq N_X - 1$ holds, return to Step 3), otherwise complete the shape estimation.

Fig. 2.4 shows Steps 2), 3) and 4) in these procedures. This method enables us to increase the estimated points to $N_X(N_X - 1)/2$ by changing the parameter d. Fig. 2.5 shows the relationship between the estimated points with the bi-static model and antenna locations. Each estimated point is located at a different point on the target surface because the scattered wave propagate along a different path as shown in Fig. 2.5. This means that we can enhance the resolution of the target image using just a small number of antennas.

2.3   3-D Problem

2.3.1   System Model

SEABED is suitable for real-time 3-D imaging with BST [129]. However, it assumes 2-D scanning of the mono-static radar. For the same reasons as described in 2-D problem, there exists a trade-off between the resolution of the image and the time taken for data acquisition. To resolve this problem, we extend the bi-static model to 3-D problems with linear array antennas.

Fig. 2.6 shows the system model in 3-D problems. We utilize the same assumption of the target and the medium as in Sec. 1.5.6. We set a linear array antenna along the x axis and scan it along the y axis. The transmitted and received antenna locations are defined in r-space as $(X_\mathrm{T}, Y, 0)$ and $(X_\mathrm{R}, Y, 0)$, respectively. We define the received electric field
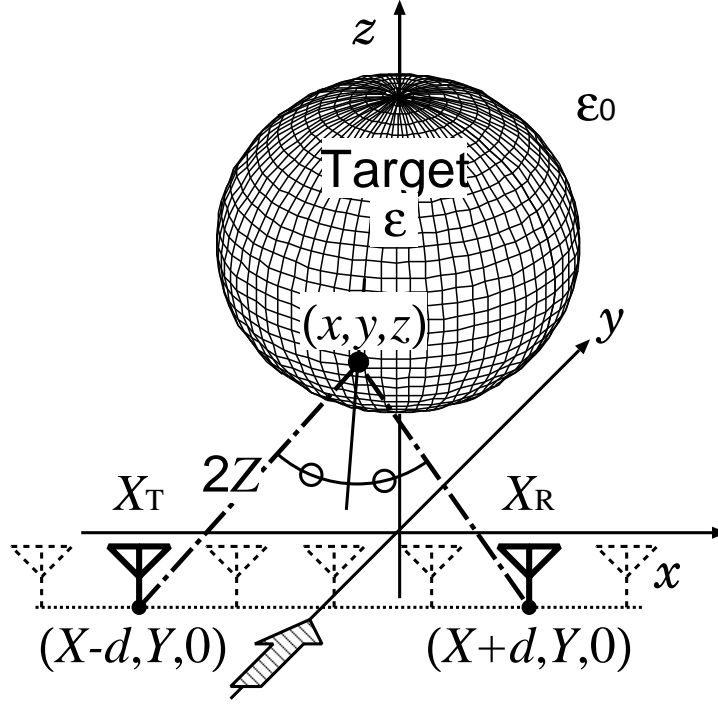
Figure 2.6: System model with linear array antennas in 3-D problems.

as $s'(X_\mathrm{T}, X_\mathrm{R}, Y, Z')$. We define the output of the matched filter with the transmitted waveform as $s(X_\mathrm{T}, X_\mathrm{R}, Y, Z')$. The quasi wavefront is extracted as $(X_\mathrm{T}, X_\mathrm{R}, Y, Z)$ by connecting the significant peaks of $s(X_\mathrm{T}, X_\mathrm{R}, Y, Z')$, and it expresses d-space. R-space is expressed by (x, y, z), which is the target boundary. A transform from $(X_\mathrm{T}, X_\mathrm{R}, Y, Z)$ to (x, y, z) corresponds to the imaging.

2.3.2 Bi-Static BST for Linear Array Antennas

Let us introduce the reversible transform for bi-static radars for 3-D problems. We set $X = (X_\mathrm{T} + X_\mathrm{R})/2$ and $X_\mathrm{T} = X_\mathrm{R} + 2d$, where d is constant. (x, y, z) is defined as the scattering point of the target boundary. Z is the distance to (x, y, z), where the law of reflection is satisfied as shown in Fig. 2.6. BBST and IBBST in 3-D problems are given as

$$
\left.
\begin{aligned}
X &= x + \frac{2z_x(z^2 + z^2 z_x^2 + d^2)}{z(1 - z_x^2 + z_y^2) + \sqrt{z^2(1 + z_x^2 + z_y^2)^2 + 4d^2 z_x^2}} \\
Y &= y + z z_y \\
Z &= \sqrt{z^2(1 + z_y^2) + z z_x(X - x) + d^2},
\end{aligned}
\right\},
\tag{2.5}
$$

39
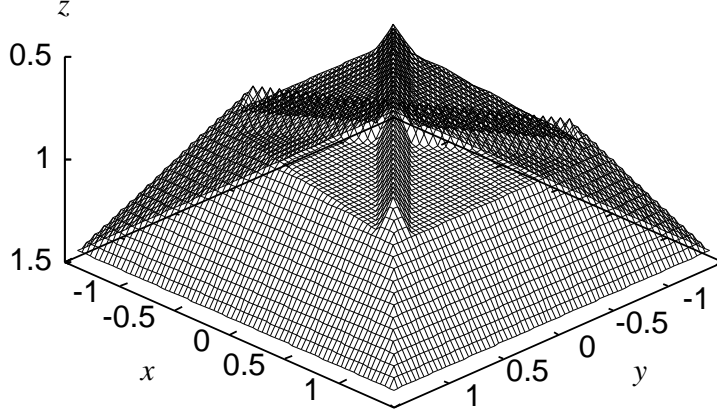
Figure 2.7: True target boundary.

$$
\left.
\begin{aligned}
x &= X - \frac{2Z^3 Z_X}{Z^2 - d^2 + \sqrt{(Z^2 - d^2)^2 + 4d^2 Z^2 Z_X^2}} \\
y &= Y + Z_Y\{d^2(x - X)^2 - Z^4\}/Z^3 \\
z &= \sqrt{Z^2 - d^2 - (y - Y)^2 - \frac{(Z^2 - d^2)(x - X)^2}{Z^2}}.
\end{aligned}
\right\},
\qquad (2.6)
$$

where $z_y = \partial z/\partial y$ and $Z_Y = \partial Z/\partial Y$. The derivations of Eqs. (2.5) and (2.6) are given in Appendix A.2. IBBST enables direct estimates of the target shape for 3-D problems.

Procedure of High-Resolution 3-D Imaging

With the similar approach in 2-D problem, the procedure of the 3-D imaging is summarized as follows. The point of a quasi wavefront (X_T, X_R, Y, Z) is extracted by connecting the peak of $s(X_T, X_R, Y, Z')$. We extract (X, Y, Z) from (X_T, X_R, Y, Z), where $2d = k\Delta X$ holds, and $k = 0, 1, ..., N_X - 1$ is satisfied. IBBST is applied to the extracted wavefront (X, Y, Z) and the target boundary is estimated for each d. By changing the distance d, we can increase the number of estimated points for the x direction. As the same reason for the 2-D case, each estimated point expresses a different target point. This enables us to enhance the resolution of the image in the x direction without increasing the number of antennas.

2.3.3 Application Examples with Numerical Simulations

We now consider examples of shape estimations using numerical simulations. The target boundary is set as shown in Fig. 2.7. The linear array antenna is set for $-2.0\lambda \leq x \leq 2.0\lambda$, where each interval of the antennas is 0.4λ, and $N_X = 11$. We scan this array antenna for $-2.0\lambda \leq y \leq 2.0\lambda$, where the number of observations N_Y is 51. It is assumed that the

true quasi wavefront $(X_{\mathrm{T}}, X_{\mathrm{R}}, Y, Z)$ without noise is given. Fig. 2.8 shows the estimated image with the mono-static model, in which the total number of estimated points is 459. It is clear that the image with the mono-static model has an insufficient resolution to express the target surface for the x direction, especially on the upper side of the target. This is because the number of estimated points for the x direction is limited to N_X. In contrast, Fig. 2.9 shows the estimated image with the bi-static model, which achieves a higher resolution for the x direction, and captures the details on the upper side. In this method, the total number of estimated points is 2754. These results verify that the bi-static model has the advantage of providing a high resolution image without increasing the number of antennas. The error around the edge points is caused by the error of the numerical derivative.

Next, we show an application example in which the received signals are calculated with FDTD method in a noiseless environment. We extract the quasi wavefront by connecting the peaks of $s(X_{\mathrm{T}}, X_{\mathrm{R}}, Y, Z')$. Figs. 2.10 and 2.11 show the estimated image with the mono-static and bi-static model, respectively. The total number of estimated points employed in the mono-static and the bi-static models are 432 and 1920, respectively. Our method provides a higher resolution than that of the mono-static model. However, the accuracy of the image is distorted around the target edges compared to that shown in Fig. 2.9. This is because deformation of the scattered waveform generates errors in the quasi wavefront. It is our future task to enhance the accuracy around this region by compensating these distortions. The computational time required for imaging is within 30 msec when using a single Xeon 3.2 GHz processor, which is sufficiently quick for real-time operations.

2.3.4 Application Examples with the Experiment

This section describes the performance evaluation with an experiment. Fig. 2.12 shows the arrangement of the linear array antennas and the target, as well as the coordinates used in the experiment. We utilize a UWB signal with a center frequency of 3.2 GHz and a 10 dB-bandwidth of 2.0 GHz. The antenna has an elliptic polarization whose ratio of the major axis to the minor one is about 17 dB; the direction of the polarimetry is along the x axis. The 3dB beam width of the antenna is about 90°. The linear array antennas are set in the vertical direction with 18 antennas. The interval is 100 mm, which corresponds to 1.1 center wavelength of the pulse. The array antennas are scanned along the y axis for -300 mm $\leq y \leq 300$ mm. The sampling interval is 10.0 mm, and $N_Y = 61$. The data are coherently averaged 256 times to enhance the S/N. We preliminarily measure the direct wave from the transmitting antenna without any targets and eliminate this signal from the observed signals with a target in order to obtain the scattered waveform. We observe the transmitted waveform as the reflection from a large specular board that is 1920 mm in hight and 1180 mm in width. We utilize the high-frequency relays as switches, where the isolation ratio of each relay is 50 dB and the switching time is within
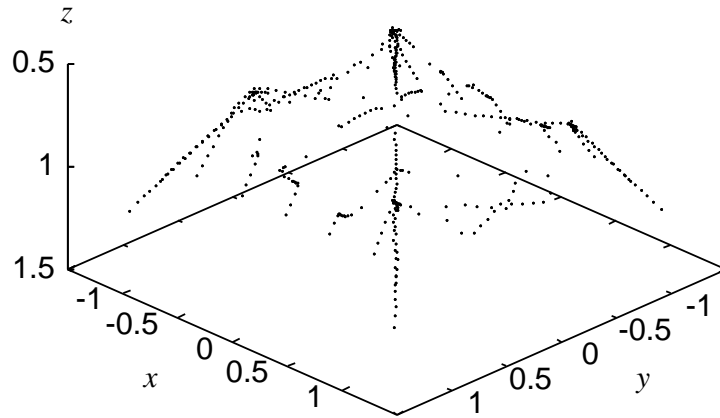
Figure 2.8: Estimated image with the mono-static model $(X_\mathrm{T}, X_\mathrm{R}, Y, Z)$ is known).
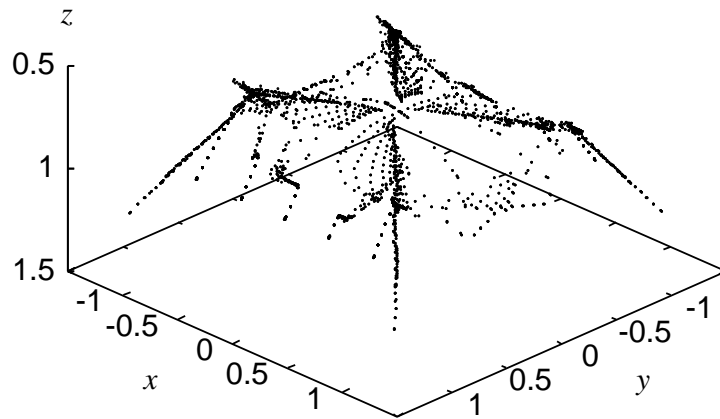
Figure 2.9: Estimated image with the bi-static model $((X_\mathrm{T}, X_\mathrm{R}, Y, Z)$ is known).

42
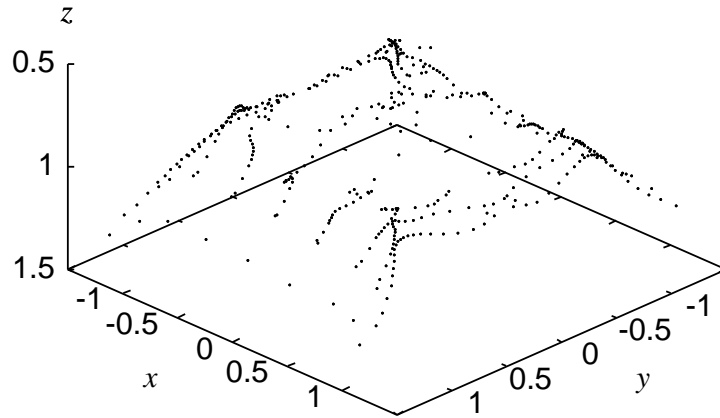
Figure 2.10: Estimated image with the mono-static model ($(X_{\mathrm{T}}, X_{\mathrm{R}}, Y, Z)$ is unknown).
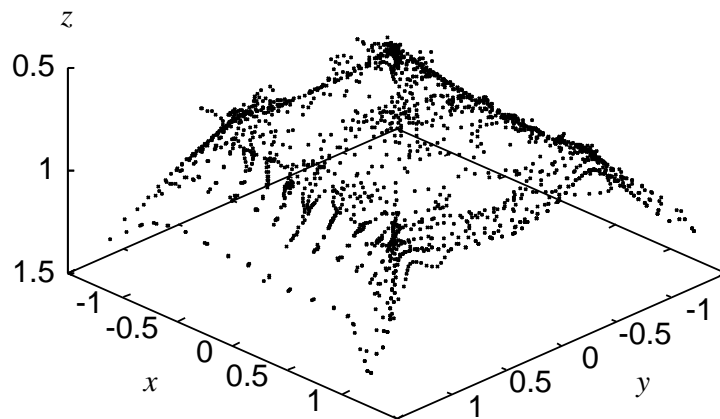
Figure 2.11: Estimated image with the bi-static model ($(X_{\mathrm{T}}, X_{\mathrm{R}}, Y, Z)$ is unknown).
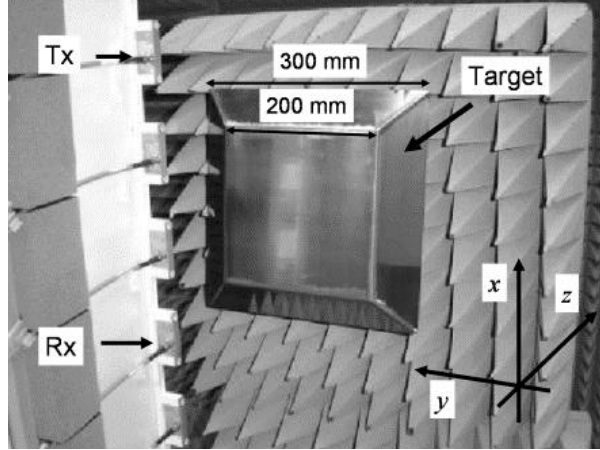
Figure 2.12: Linear array antennas and the target in the experiment.

100 msec. We divide the 18 antennas into 6 groups. To simplify the switching system, we do not select transmitting and receiving antennas from the same group. Fig. 2.13 shows the arrangement of the relays and the antennas employed in the experiment.

We set a metallic hexahedral target made of stainless steel sheeting with thickness of 3 mm. Fig. 2.14 shows the true target boundary. We utilize 11 antennas set for -500.0 mm $\leq x \leq 500.0$ mm. Fig. 2.15 shows the output of the matched filter in our experiment, where we set $X_{\mathrm{T}} = 100.0$ mm and $X_{\mathrm{R}} = -200.0$ mm. The S/N in the experiment is 32.0 dB, where we define the S/N as the ratio of peak of instantaneous signal power to the averaged noise power after applying the matched filter. This also corresponds to the standard deviation $3.0 \times 10^{-3}\lambda$ of the Gaussian random error of the quasi wavefront [131]. The extracted quasi wavefront is smoothed with the Gaussian filter with a correlation length is 0.2λ. Fig. 2.16 shows the estimated image with the mono-static model. The colors of the estimated points represent the estimation error calculated as the distance to the true target boundary. The number of estimated points is 166. The image has an insufficient resolution in the x direction to locate the edges and surface details. Fig. 2.17 shows the estimated image with the bi-static model. Our method obtains a higher resolution image around the target edges and the surface details for the x direction compared to that shown in Fig. 2.16. The number of estimated points is 496. We quantitatively evaluate the accuracy of the two methods with an evaluation value ϵ that is defined as

$$\epsilon = \sqrt{\frac{1}{N} \sum_{i=0}^{N} \min_{\boldsymbol{x}} \|\boldsymbol{x} - \boldsymbol{x}_{\mathrm{e}}^{i}\|^2}, \tag{2.7}$$

where $\boldsymbol{x}$ and $\boldsymbol{x}_{\mathrm{e}}^{i}$ express the location of the true target points and that of the estimated points, respectively. N is the number of estimated points. Values of ϵ with the mono-
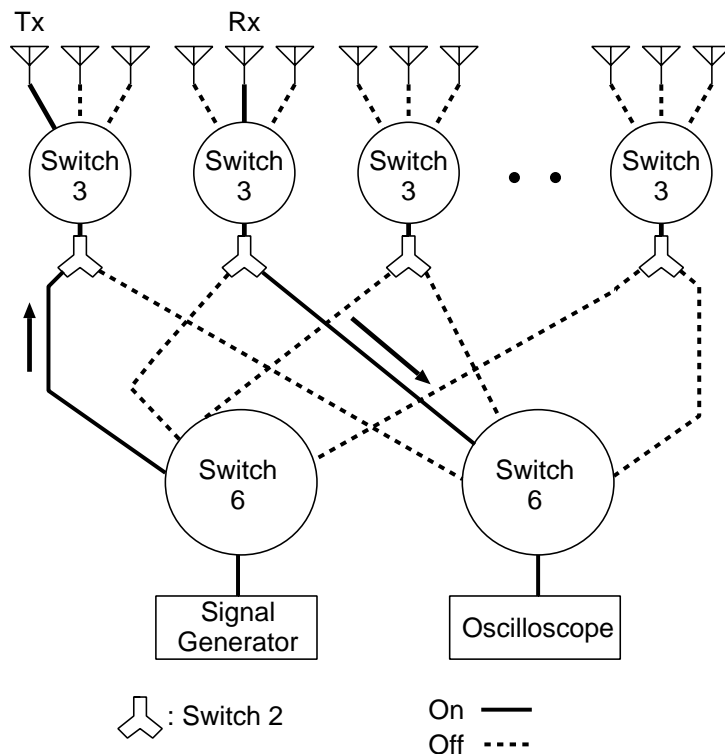
Figure 2.13: Arrangement of high-frequency relays and antennas.

static and the bi-static models are $8.8325 \times 10^{-2}\lambda$ and $8.9174 \times 10^{-2}\lambda$, respectively. In addition, Fig. 2.18 shows the minimum error to the edge points of the target boundary. The numbers along the horizontal axis correspond to those of the target edges as shown in Fig. 2.14. Fig. 2.18 confirms that the method with the bi-static model is able to estimate the edge locations more accurately than that with the mono-static model. These results demonstrate that the method with the bi-static model obtains a higher resolution image in the real environment. The calculation time for imaging is within 30 msec with a single Xeon 3.2 GHz processor, which is sufficient for real-time operations.

The estimated accuracy obtained in Fig. 2.17 deteriorates around the side of the target due to deformation of the scattered waveform. In addition, the estimated points diverge due to the noise. To enhance the robustness of the image, data is required with higher S/N and S/I. In the employed experimental system, the required time of scanning the antenna for 10mm is about 1.0 sec. We confirm that the time for data acquisition with array antennas becomes more than 5 times shorter compared to that with the mono-static scanning, where the same resolution of image is estimated.

2.4   Conclusion

We proposed a fast and high-resolution imaging algorithm with linear array antennas. The reversible transform BBST for the bi-static radars was derived, and applied to the array systems. We verified that the method with the bi-static model was effective for a fast and high-resolution imaging with numerical simulations in 2-D and 3-D problems. Additionally, we investigated the performance of our algorithm with experiments by utilizing the linear array antennas. We confirmed that the bi-static model improves the resolution of the image around the edges in the real environment without increasing the number of antennas. The required time for the data acquisition is also shorten with linear antenna scanning, which is more effective for the robotic applications. Moreover, it is our future task to enhance the accuracy around the edges by compensating those waveform deformations.
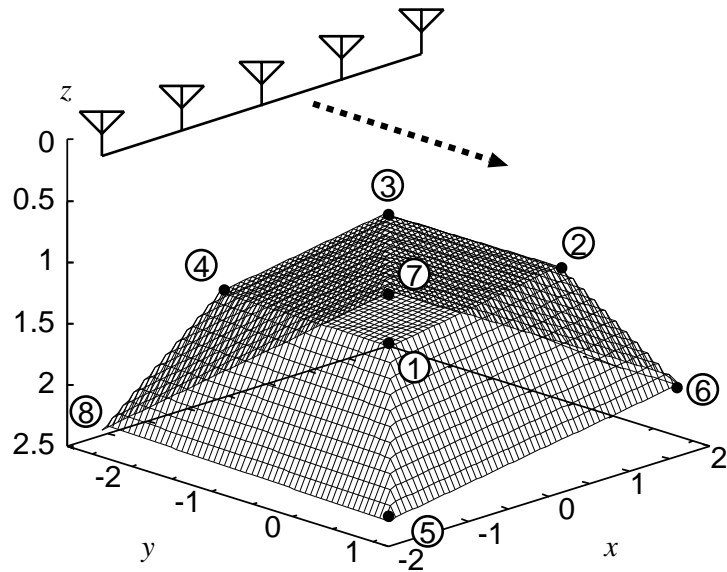
Figure 2.14: True target boundary used in the experiment.
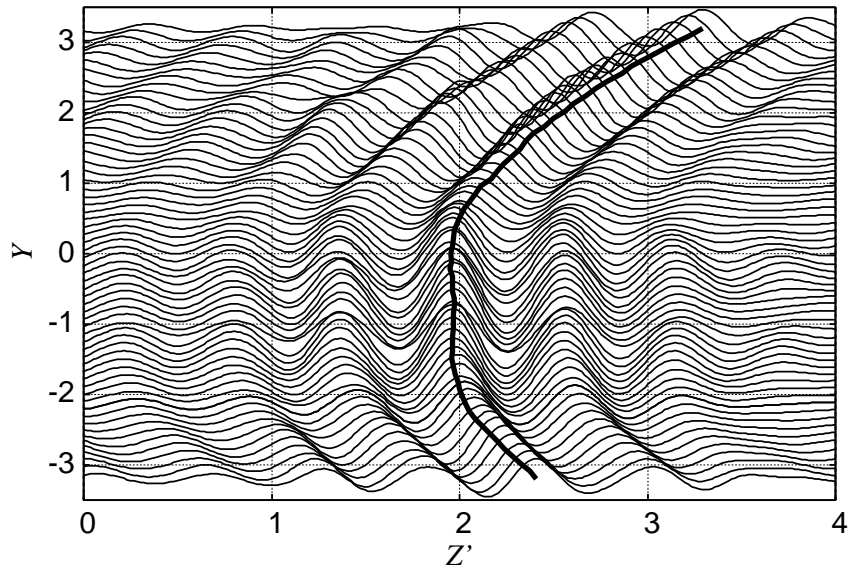
Figure 2.15: Examples of the output of the matched filter in the experiment ($X_{\mathrm{T}} = 100.0$mm, $X_{\mathrm{R}} = -200.0$mm).
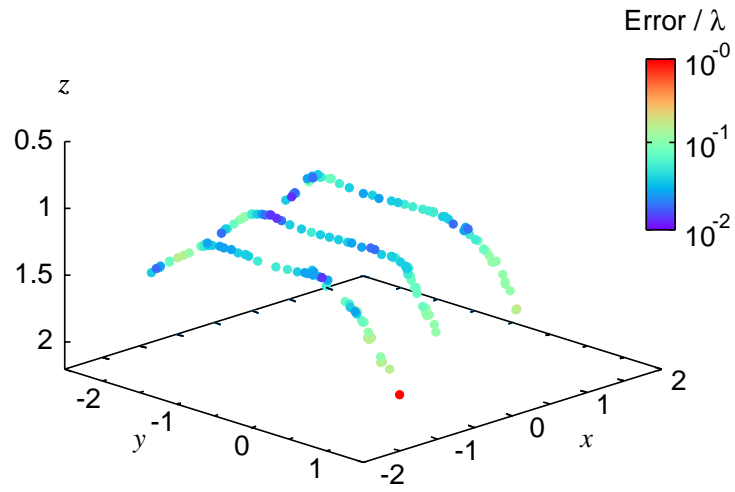
Figure 2.16: Estimated image with the mono-static model in the experiment.
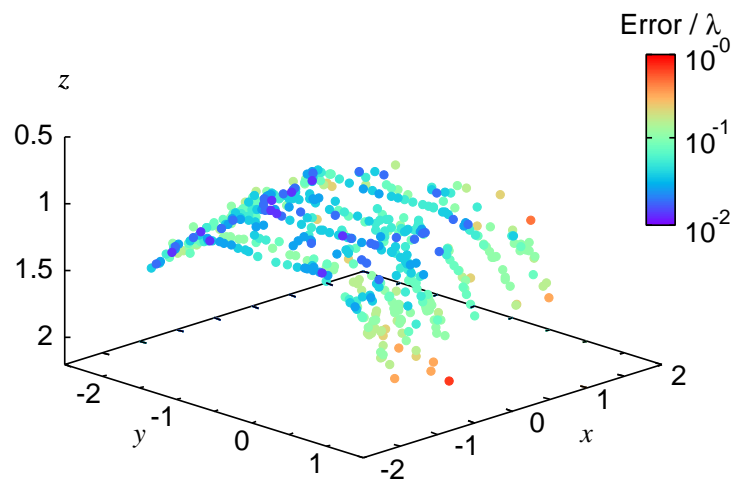
Figure 2.17: Estimated image with the bi-static model in the experiment.
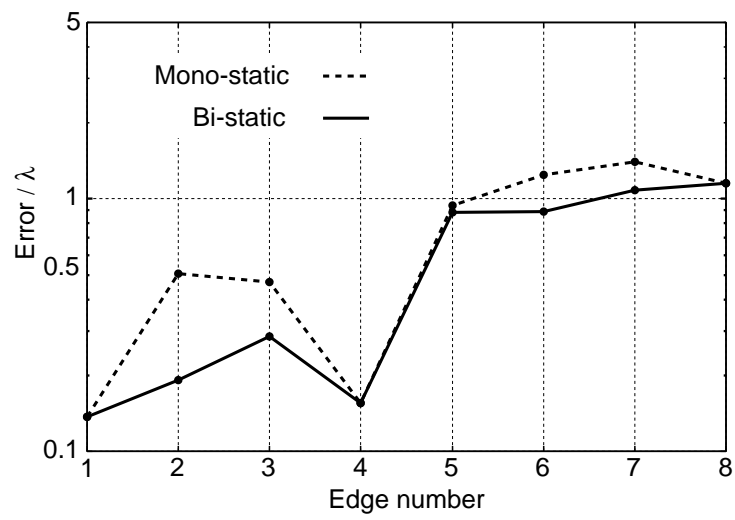
Figure 2.18: Estimated error for the target edges.

Chapter 3

Robust Imaging Algorithm without Derivative Operations

3.1 Introduction

SEABED can realize high-speed and nonparametric imaging with the simple transform as BST in 2-D or 3-D problem [127, 129]. However, the image obtained with SEABED is quite instable in a noisy environment because it utilizes derivatives of the received data. To resolve this problem, image stabilization methods have been proposed. One of them utilizes an adaptive smoothing regarding a target shape with the Gaussian filter [130], another is based on Fractional Boundary Scattering Transform [131]. While these methods are robust in a noisy environment, they cannot completely remove the instability caused by the derivative operations. Moreover, we confirm that there is a trade-off between the resolution and stability of the estimated image.

To resolve this problem, in this paper we develop a robust imaging algorithm with an envelope of circles in 2-D problem, which does not sacrifice the fastness of SEABED. We note that the previous work quoted in [132] is similar to our approach from the viewpoint that it extracts the target boundary with time delays. Additionally, this method achieves a robust imaging in a noisy environment because it does not utilize a derivative operation. However, this method can be applied only to convex targets. In this chapter, we propose a fast and robust imaging algorithm for arbitrary shaped targets including concave boundaries. We calculate circles with estimated delays for each antenna location and utilize the principle that these circles circumscribe or inscribe the target boundary. With this principle, we prove that the target boundary is expressed as a boundary of a union or an intersection set of the circles. This method does not utilize a derivative of received data, and enables us to realize robust imaging for an arbitrary shape target.

This method can be extended to the 3-D problem. It utilizes the envelope of spheres, which are calculated with the observed delays for each antenna location. It is based on the principle that these spheres should circumscribe or inscribe the target boundary.

In addition, this method can robustly compensate the phase rotation, which occurs in the case of concave boundaries. We confirm that it can realize an accurate, robust and high-speed 3-D imaging in numerical simulations.

3.2   2-D Problem

3.2.1   System Model

We utilize the same model as described in Sec. 2.2.1 in 2-D problem, except for the antenna settings. We assume a mono-static radar system. We define $s'(X, Z')$ as the received electric field at the antenna location $(x, z) = (X, 0)$. The output of the matched filter with the transmitted waveform is obtained as $s(X, Z')$. We extract the significant peaks of $s(X, Z')$ for each X, and define those peak points as (X, Z). D-space is defined as the space expressed by (X, Z), and we term it a quasi wavefront. The transform from d-space to r-space corresponds to the imaging.

3.2.2   Instability in SEABED

SEABED utilizes a reversible transform BST between the point of r-space (x, z) and the point of d-space (X, Z). Fig. 3.1 shows the relationship between the r-space and the d-space. IBST utilizes the characteristic that an incident wave is intensively reflected in the normal direction because the mono-static radar is assumed. While SEABED realizes rapid imaging, the estimated image easily deteriorates in a noisy environment because IBST utilizes the derivative of a quasi wavefront. In this section, we examine the behavior of SEABED in a noisy environment. We scan an antenna in $-2.5\lambda \leq x \leq 2.5\lambda$, and receive data at 101 locations. We give the true quasi wavefront with random error whose standard deviation is 0.005λ. We smooth the quasi wavefront with the Gaussian filter. Figs. 3.2, 3.4 and 3.3 show the estimated boundary by applying IBST to the quasi wavefront where, we set the correlation length of the filter as 0.05λ, 0.2λ and 0.1λ, respectively. In Fig. 3.2, the estimated points have large errors around the edge. This is because the correlation length is too short. To discuss the deterioration of the image analytically, we rewrite IBST as

$$\left. \begin{array}{ccc} x & = & X + Z\cos\theta \\ z & = & Z\sin\theta \end{array} \right\}, \tag{3.1}$$

$$\theta = \cos^{-1}(-\partial Z/\partial X), \quad (0 \leq \theta < \pi),$$

where θ is expressed as in Fig. 3.1. Eq. (3.11) means that the estimated points with IBST are on the circle whose center is $(X, 0)$ and radius is Z. In the equation, θ is determined with $\partial Z/\partial X$. Therefore, the estimated point mistakenly plots along this circle in a noisy environment because the accuracy of θ strongly depends on that of $\partial Z/\partial X$.
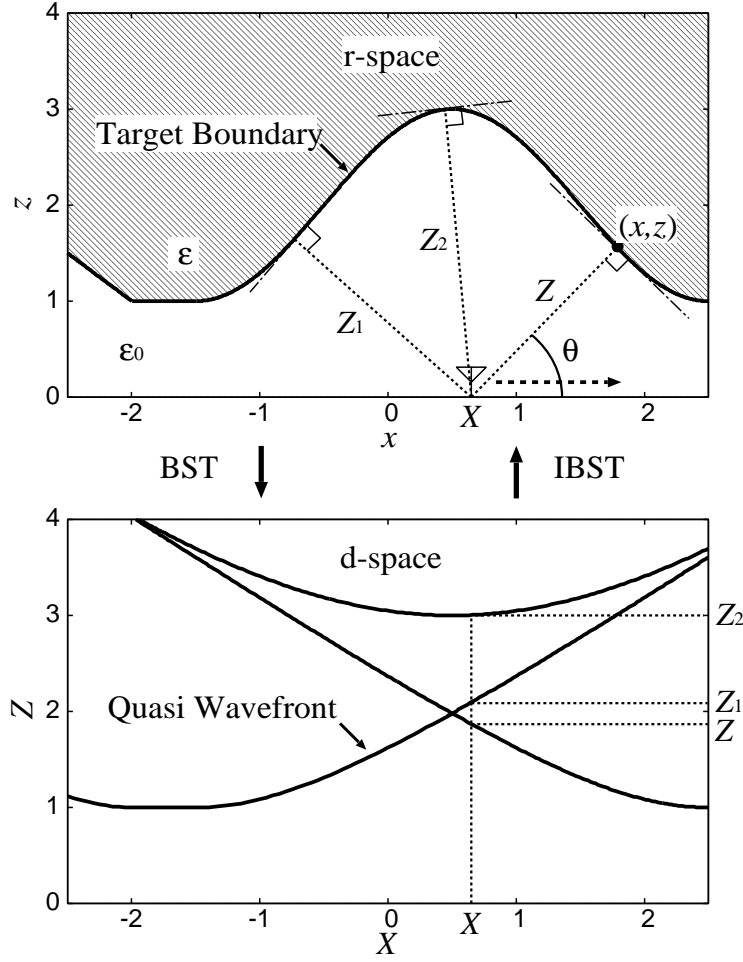
Figure 3.1: Relationship between r-space (upper) and d-space (lower).

While the estimated image in Fig. 3.3 is stable, the resolution of the image degrades, especially around the edge. Accordingly, SEABED suffers from a trade-off between the stability and the resolution of the estimated image. Therefore, we empirically choose the correlation length as 0.1λ which holds the resolution and a stability of the image as shown in Fig.3.4. However the estimated points in Fig. 3.4 still have errors. To resolve this trade-off in SEABED, methods for stabilizing images have been proposed. One method is based on smoothing the quasi wavefront, where we change the standard deviation of the Gaussian filter depending on the target shape [130]. Another is based on smoothing the data obtained in the intermediate space between the r-space and the d-space using Fractional Boundary Scattering Transform [131]. These methods achieve robust imaging in a noisy environment. However, they cannot completely resolve the above trade-off because they still depend on the derivative operations.
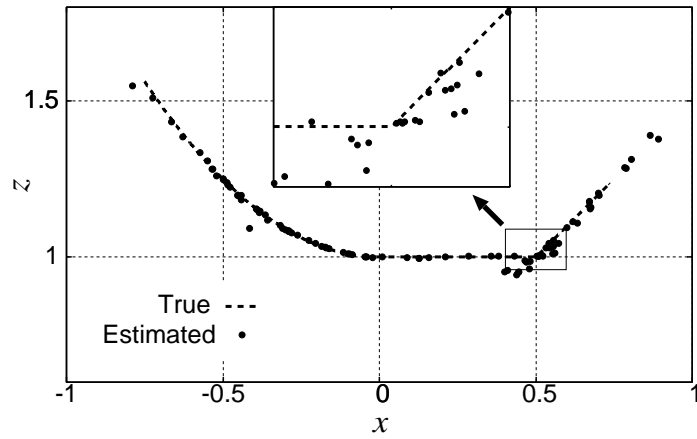
Figure 3.2: An estimated image with SEABED in noisy case, where correlation length is set to 0.05λ ((X, Z) is known).
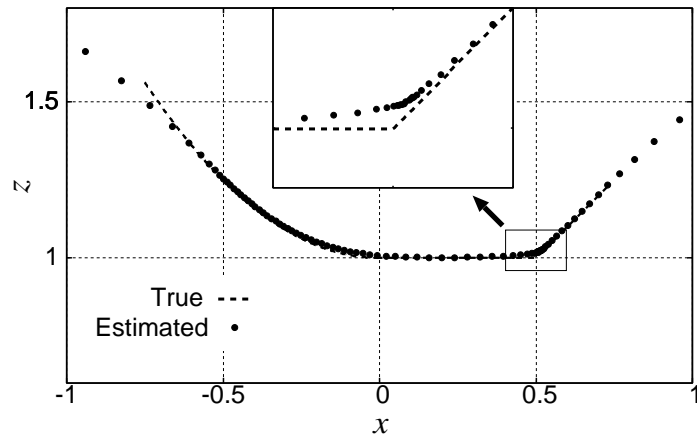
Figure 3.3: Same as Fig. 3.2 but correlation length is set to 0.2λ ((X, Z) is known).
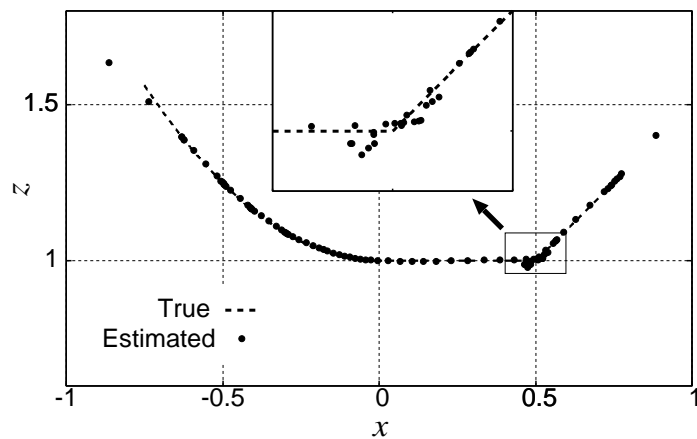
Figure 3.4: Same as Fig. 3.2 but correlation length is set to 0.1λ ((X, Z) is known).
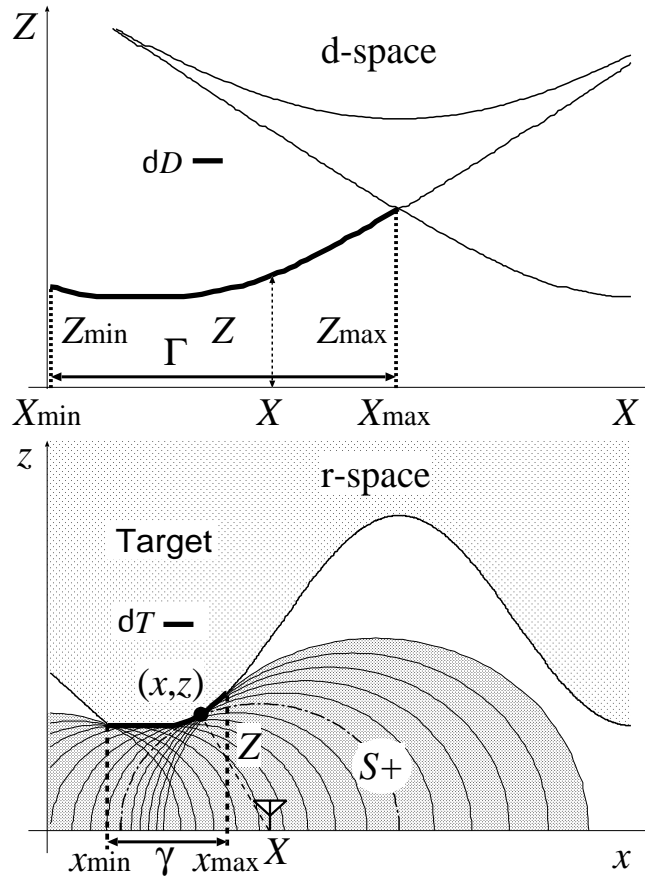
Figure 3.5: Quasi wavefront (upper) and a convex target boundary and an envelope of circles (lower).

3.2.3 Target Boundary and Envelopes of Circles

To resolve the trade-off between the stability and resolution of SEABED as set out in the previous section, we propose a new imaging algorithm that is free from derivative operations. First, we clarify the relationship between the group of points on a target boundary and that on the envelope of the circles. We assume that the target boundary ∂T is expressed as a single-valued and differentiable function. (X, Z) is a point on ∂D, which is the quasi wavefront of ∂T. We define Γ as the domain of X for ∂D. $\partial x / \partial X = 1 - (\partial Z / \partial X)^2 - Z \partial^2 Z / \partial X^2$ is utilized, and γ is defined as the domain of x for ∂T. We define $S_{(X,Z)}$ as an open set, which is defined as an interior of the circle which satisfies $(x - X)^2 + z^2 = Z^2$. Figs. 3.5 and 3.6 show the relationship between d-space and r-space for a convex and a concave targets, respectively. If ∂D is a single-valued and continuous function, we define $S_+ = \bigcup_{X \in \Gamma} S_{(X,Z)}$ and $S_\times = \bigcap_{X \in \Gamma} S_{(X,Z)}$. We define the boundary

54
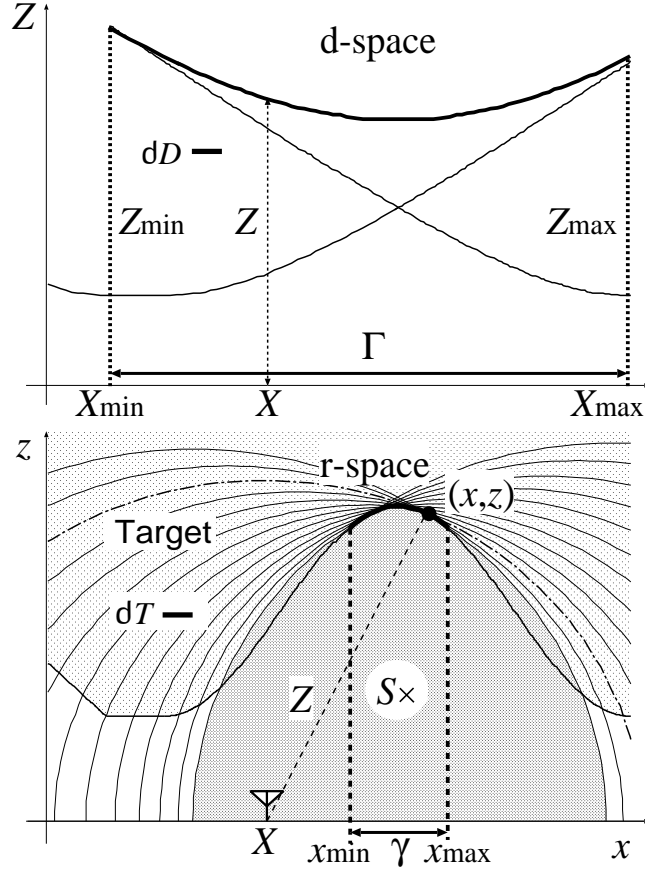
Figure 3.6: Quasi wavefront (upper) and a concave target boundary and an envelope of circles (lower).

∂S_+ as

$$\partial S_+ = \{(x, z) \mid (x, z) \in \overline{S_+} - S_+, \ x \in \gamma, \ z > 0\}, \tag{3.2}$$

and $\partial S_\times$ as

$$\partial S_\times = \{(x, z) \mid (x, z) \in \overline{S_\times} - S_\times, \ x \in \gamma, \ z > 0\}, \tag{3.3}$$

where $\overline{S_+}$ and $\overline{S_\times}$ is a closure of S_+ and $S_\times$, respectively.

Here the next equation holds

$$\partial T = \begin{cases} \partial S_+ & (\partial x/\partial X > 0), \\ \partial S_\times & (\partial x/\partial X < 0). \end{cases} \tag{3.4}$$

The proof of Eq. (3.4) is given in Appendix B.1. Eq. (3.4) shows that ∂S_+ and $\partial S_\times$ express the target boundary as an envelope of circles depending on the sign of $\partial x/\partial X$ as shown in Figs. 3.5 and 3.6. We should correctly select these methods considering the sign of $\partial x/\partial X$. We utilize the next proposition.

55

Proposition 1 *The necessary and sufficient condition of $\partial x/\partial X < 0$ is that*

$$\overline{S_+} \subset \overline{S_{\max} \cup S_{\min}} \tag{3.5}$$

Here, we define $(X_{\max}, Z_{\max})$ and $(X_{\min}, Z_{\min})$ as the point of ∂D, where $X_{\max}$ and $X_{\min}$ are the maximum and minimum values, respectively, at $X \in \Gamma$, as shown in Fig. 3.6. We define $S_{\max}$ and $S_{\min}$ express $S_{(X_{\max}, Z_{\max})}$ and $S_{(X_{\min}, Z_{\min})}$, respectively.

A proof of Proposition 1 is given in Appendix B.2. If $\partial x/\partial X < 0$ holds, all circles for $X \in \Gamma$ should inscribe to the target boundary. This condition corresponds to that $x(X_{\max}, X) < x(X_{\max}, X_{\min}) < x(X_{\min}, X)$ holds for all $X \in \Gamma$ as shown in Fig. B.3, where $x(X, X')$ is x coordinates of the intersection point of $\partial S_{(X,Y)}$ and $\partial S_{(X',Y')}$. This condition is equivalent to Eq. (3.5) that all $S_{(X,Y)}$ in $X \in \Gamma$ are included in $S_{\max}$ and $S_{\min}$. Accordingly, the number of circles which constitute $\overline{S_+}$ should be 2 in minimum for $\partial x/\partial X < 0$. We should search the minimum number of the circles which constitute $\overline{S_+}$. If the minimum number is 2, $\partial T = \partial S_\times$ holds; otherwise, $\partial T = \partial S_+$ holds. When a target boundary includes an edge, the edge can be estimated as the intersection point of circles $\partial S_{(X,Y)}$, where (X, Y) is transformed into the edge point (x, y) with the IBST. Therefore, the target boundary ∂T with edges can be expressed as one of ∂S_+ and $\partial S_\times$.

In this method, we estimate the target boundary with an envelope of circles by utilizing these relationships. This method enables us to transform the group of points (X, Z) to the group of points (x, z) without a derivative operation. Note that we receive the scattered wave that passes through a caustic point if the quasi wavefronts satisfies $\partial x/\partial X < 0$. In that case, a phase of the scattered waveform rotates by $\pi/2$ [128]. We can robustly recognize this phase rotation from (X, Z) with the sufficient condition of proposition 1. We compensate this phase rotation in this method to enhance the accuracy of the estimated image.

Actual Procedures

The actual procedures of the imaging method with an envelope of circles are as follows. We also define ΔX as the sampling interval of the antenna.

Step 1). Apply the matched filter to the received signals $s'(X, Z')$ and obtain the output $s(X, Z')$.

Step 2). Extract quasi wavefronts as (X, Z'') which satisfies $\partial s(X, Z')/\partial Z' = 0$, $s(X, Z') \geq \alpha \cdot \max_{Z'} s(X, Z')$. Extract (X, Z) as ∂D_{T} from (X, Z''), which satisfies the local maximum of Z'' for each X. Parameter α and the searching region of Z'' are determined empirically.

Step 3). Extract a set of (X, Z) as ∂D_i from ∂D_{T}, which is continuous and $|\partial Z/\partial X| \leq 1$ is satisfied.
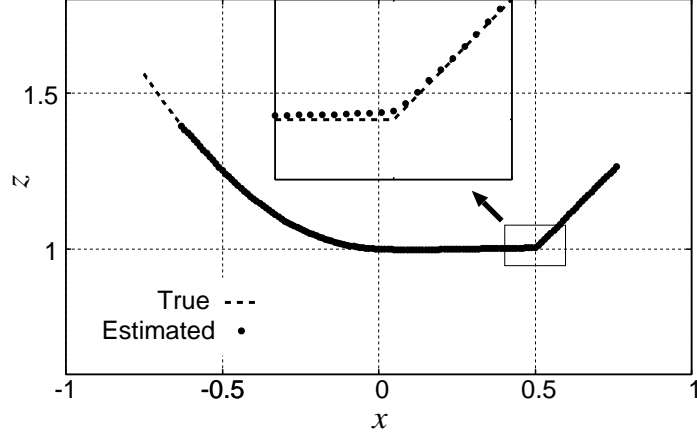
Figure 3.7: Estimated image with Envelope for a convex target with noise ((X, Z) is known).

Step 4). Extract boundary points (x, z) on ∂S_+ as

$$z = \max_{X \in \Gamma_i} \sqrt{Z^2 - (x - X)^2}, \tag{3.6}$$

where Γ_i is a domain of X where $(X, Z) \in \partial D_i$ satisfies. Count the minimum number of circles which constitute S_+, and define the number as N_C. If $N_C > 2$, determine

$$\partial T_i = \partial S_+, \ (x_{\min} \leq x \leq x_{\max}), \tag{3.7}$$

where $x_{\min} = x(X_{\min}, X_{\min} + \Delta X)$ and $x_{\max} = x(X_{\max}, X_{\max} - \Delta X)$.

If $N_C = 2$, compensate a phase rotation for $s(X, Z')$ by $\pi/2$ and renew the quasi wavefronts as (X, Z_c), and extract boundary points (x, z) on $\partial S_\times$ as

$$z = \min_{X \in \Gamma_i} \sqrt{Z_c^2 - (x - X)^2}. \tag{3.8}$$

Determine
$$\partial T_i = \partial S_\times, \ (x_{\min} \leq x \leq x_{\max}), \tag{3.9}$$

where $x_{\min} = x(X_{\max}, X_{\max} - \Delta X)$ and $x_{\max} = x(X_{\min}, X_{\min} + \Delta X)$.

Step 5). Set $i = i + 1$, and iterate Step 3) and 4) until ∂D_T becomes empty.

Step 6). Estimate the target boundary as $\partial T = \bigcup_i \partial T_i$.

We term this method as Envelope.

Figure 3.8: Estimated image with SEABED for a concave target with noise ((X, Z) is known).
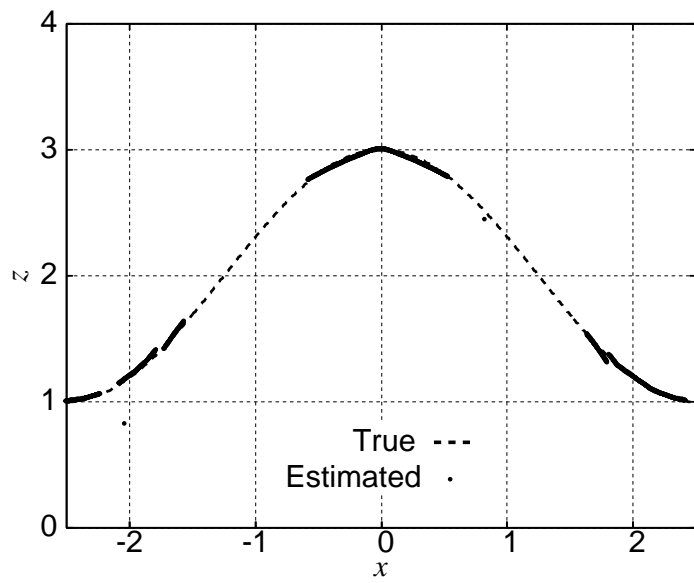
Figure 3.9: Estimated image with Envelope for a concave target with noise ((X, Z) is known).

3.2.4 Shape Estimation Examples

We evaluate the estimation accuracies of SEABED and the method we propose here. First, we give the random errors to the true quasi wavefront, which is calculated from the true target boundary with BST. The standard deviation of the noise is 0.005λ. This simulation estimates the accuracy without influences from other factors including waveform distortion. The signals are received at 101 locations for $-2.5\lambda \leq x \leq 2.5\lambda$. We fix the correlation length to 0.1λ from the results of Sec. 3.2.2. Fig. 3.7 shows the estimated image where we apply Envelope to the same data as Fig. 3.2. The estimated image with Envelope achieves more stable and high-resolution imaging than SEABED, especially around the edge. Figs. 3.8 and 3.9 show the estimated images of the concave target achieved with SEABED and Envelope, respectively. The estimated image for the concave shape with SEABED is not stable, especially at around $x = 0, \pm 2$. Contrarily, the estimated image with Envelope is more stable and accurate. This is because Envelope estimates the inclination of the target as that of the circles, which circumscribe or inscribe to the target boundary. A part of the circles contributes as a part of the estimated shape, which means that the inclination of the circle is utilized for imaging.

Next, we add a white noise to the received data $s'(X, Z')$ calculated with the FDTD method. Fig. 3.10 shows the output of the matched filter with the transmitted waveform. In this case, S/N is about 28 dB. Here we define S/N as

$$\text{S/N} = \frac{1}{\sigma_{\text{N}}^2 (X_{\text{max}} - X_{\text{min}})} \int_{X_{\text{min}}}^{X_{\text{max}}} \max_{Z'} |s(X, Z')|^2 \partial X, \tag{3.10}$$

where X_{max} and X_{min} are the maximum and minimum antenna locations, respectively, and σ_{N} is the standard deviation of noise. Fig. 3.11 and 3.12 show the estimated images with SEABED and Envelope, respectively. The image of SEABED is not accurate especially around the edges of the target. Contrarily, the image obtained by Envelope is stable, although the image around the edge is not precise compared with Fig. 3.7. We confirm that the same image distortion around the edge appear in a noiseless case. Therefore, the image distortion is caused by the edge diffraction waveform which is different from the transmitted one. We should also estimate the scattered waveform by using the estimated image to enhance the accuracy. This will be resolved in the following chapter.

Next, we deal with scattered signals for a concave target. Fig. 3.13 shows the output of the matched filter. S/N is 32 dB. Figs. 3.14 and 3.15 show the estimated images for a concave target with SEABED and Envelope, respectively. Envelope can estimate a more stable and accurate image than that can be achieved with SEABED. The phase rotation of the scattering at the concave surface is correctly compensated. The calculation time of SEABED is 10.0 msec. Envelope requires more than 10.0 msec. This is because our method requires searching operation in Eqs. (3.6) and (3.8). This computational time is short enough for real time imaging. Additionally, due to multiple scattering, false images are seen above the target boundary. To develop a robust algorithm without false images will also be a future task.
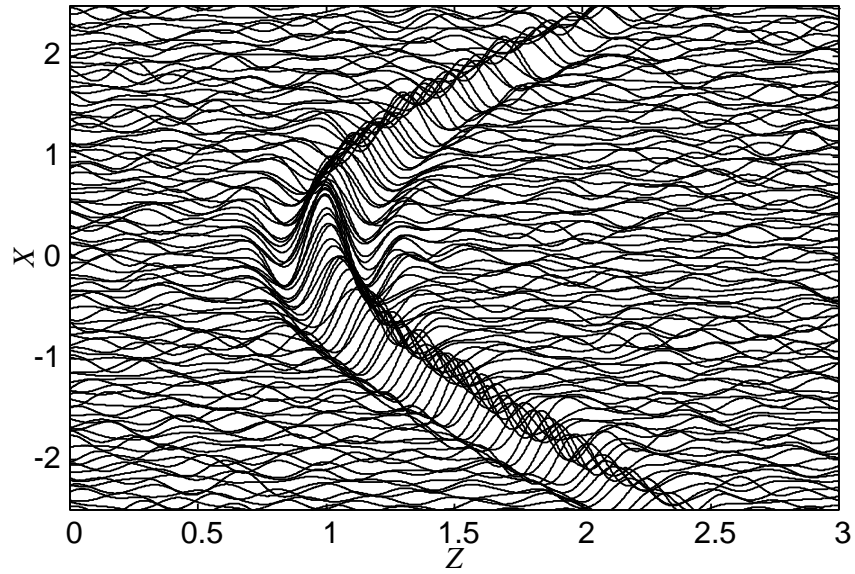
Figure 3.10: Output of the matched filter for a convex target.

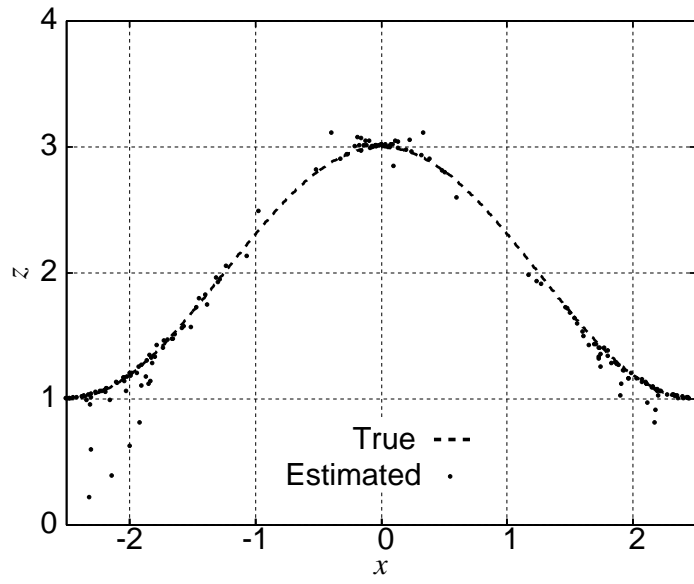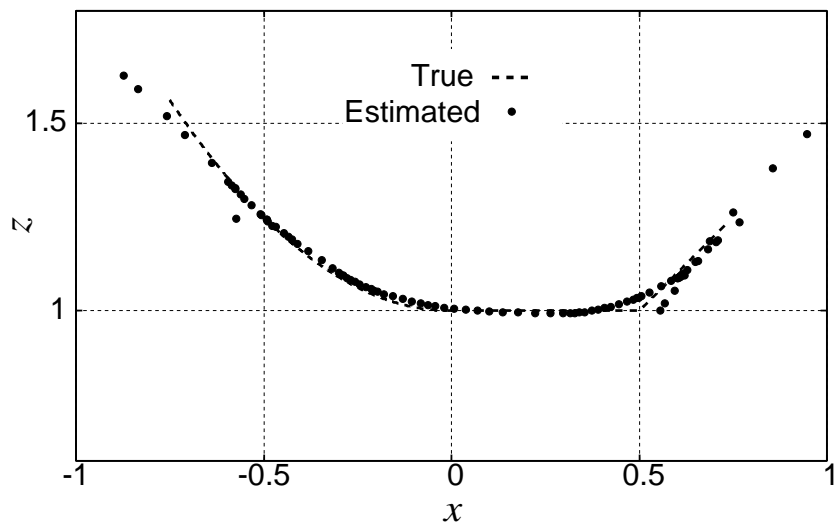Figure 3.11: Estimated image with SEABED for a convex target with noise ((X, Z) is unknown).

60
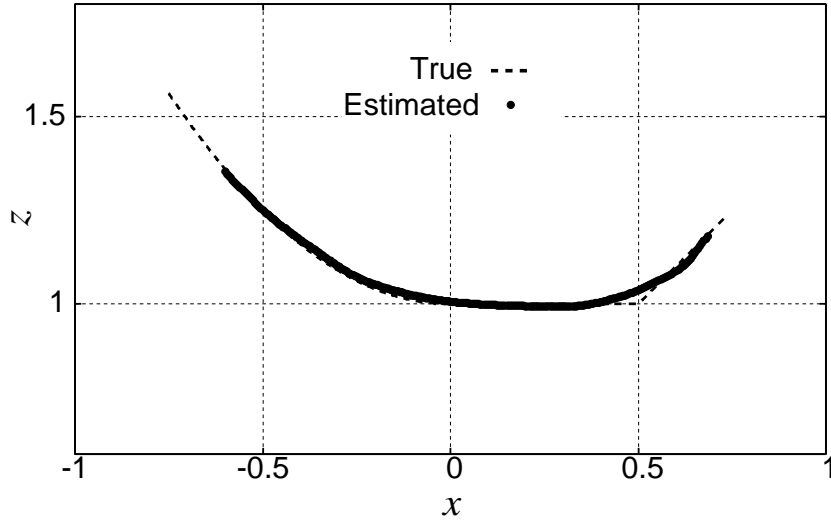
Figure 3.12: Estimated image with Envelope for a convex target with noise ((X, Z) is unknown).

We should compare our method with the conventional method [131]. Fractional boundary scattering transform enables us to deal with the intermediate space between r-space and d-space. With this transform, we can adaptively smooth data depending on the target shapes. The optimized way of smoothing with FBST is equal to the smoothing in the d-space for the assumed target shapes in Figs. 3.4 and 3.8. Therefore, Figs. 3.4 and 3.8 correspond to the optimal smoothing method with FBST.

3.2.5 Accuracy Limitation to Noise

In this section, we quantitatively evaluate the accuracy of the estimated image with Envelope. We give random errors to the true quasi wavefront. Figs. 3.16 and 3.17 show the root mean square errors (abbreviated as RMS) for the convex and the concave target, respectively. The number of trial is 500. Our method obtains 2 times improvement in accuracy for the both targets compared to SEABED, where $\sigma_N = 5.0 \times 10^{-3}\lambda$. These improvements do not depend on the noise power. Also, the accuracy of each method is larger than $1.0 \times 10^{-3}\lambda$. This is because the quasi wavefront is smoothed with the Gaussian filter whose correlation length is 0.1λ, which causes a systematic error. Although RMS depends on the correlation length of the Gaussian filter, we confirm that RMS of Envelope is better than that of SEABED regardless of the correlation length. The reasons of these results are as follows. SEABED determines a point of the target boundary with derivative operations. Contrarily, Envelope utilizes all of the points of a quasi wavefront in Eqs. (3.6) and (3.8). Therefore, this method absorbs the instability of the derivative operations with
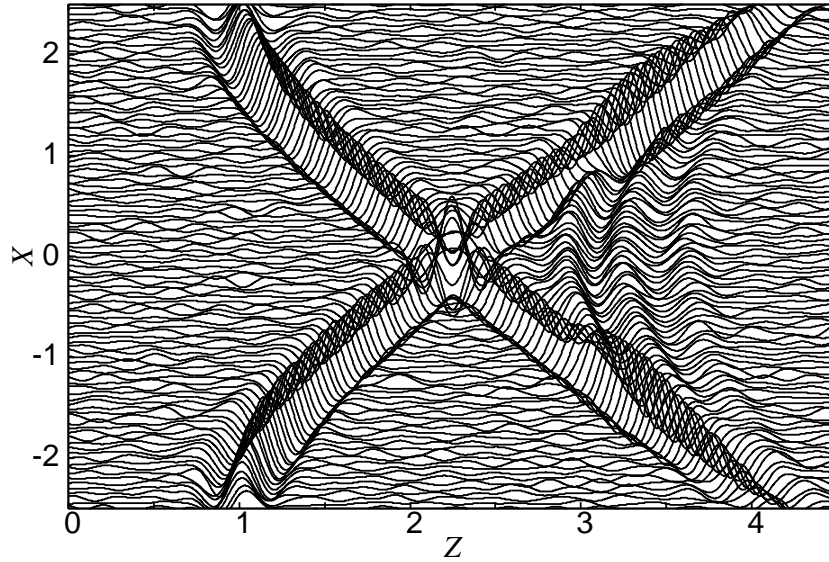
Figure 3.13: Output of the matched filter for a concave target.

the wider information of a quasi wavefront.

Moreover, we see the fluctuations of errors with SEABED in Fig. 3.16. We see the same fluctuation, even if we increase the number of the trial to 10000. The reason is that the relationship between the accuracy and the noise intensity is not simple because SEABED utilizes derivative operations. Additionally, the accuracy of each method depends on the local shape of the target. Figs. 3.18 and 3.19 show the estimation error of z for each x in the both targets ($\sigma_N = 5.0 \times 10^{-3}\lambda$). As shown in Fig. 3.18, the error around the edge region becomes large even in the low noise situation. Though we assume that the antenna is scanned along the straight line in the paper, this method can be readily extended to scanning along an arbitrary curved line.
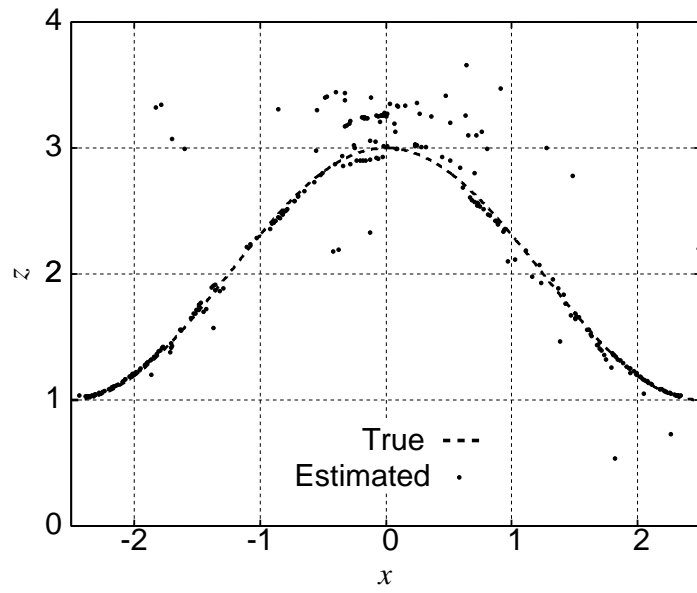
Figure 3.14: Estimated image with SEABED for a concave target with noise ((X, Z) is unknown).
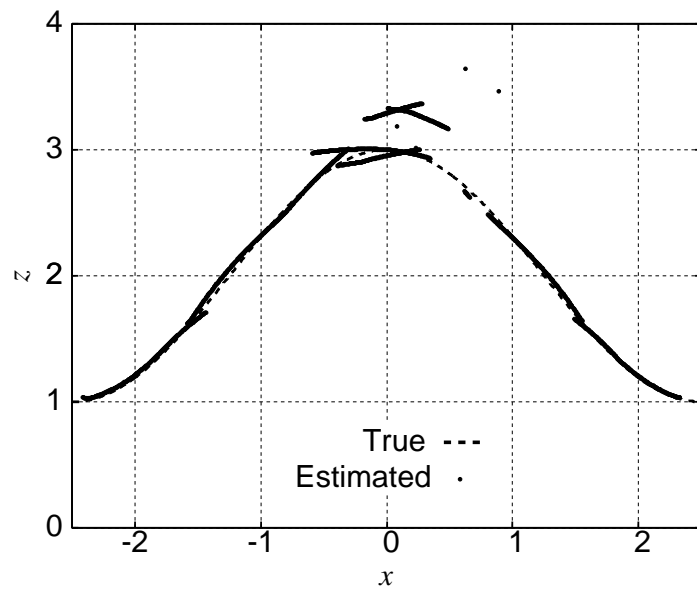
Figure 3.15: Estimated image with Envelope for a concave target with noise ((X, Z) is unknown).
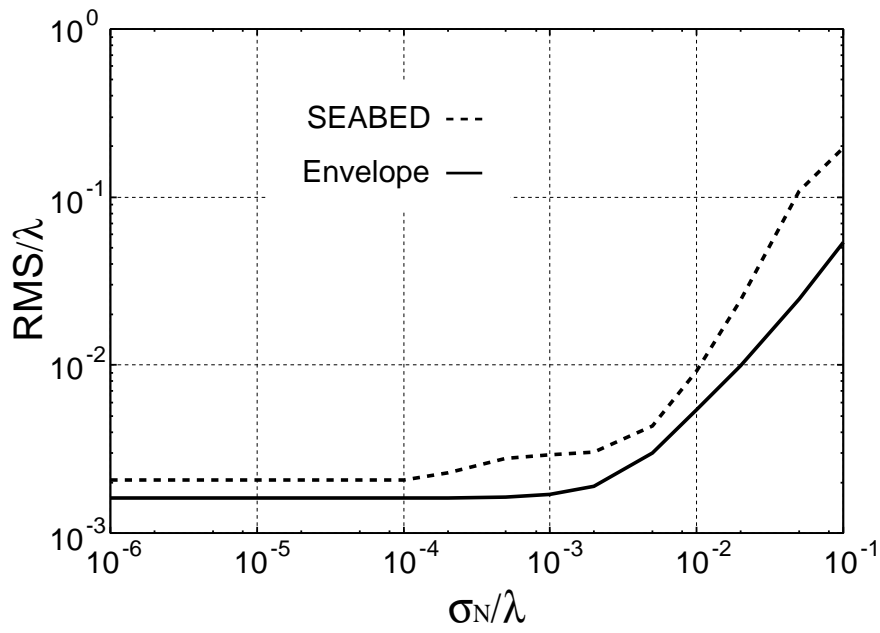
Figure 3.16: Relationship between RMS and σ_N for a convex target.
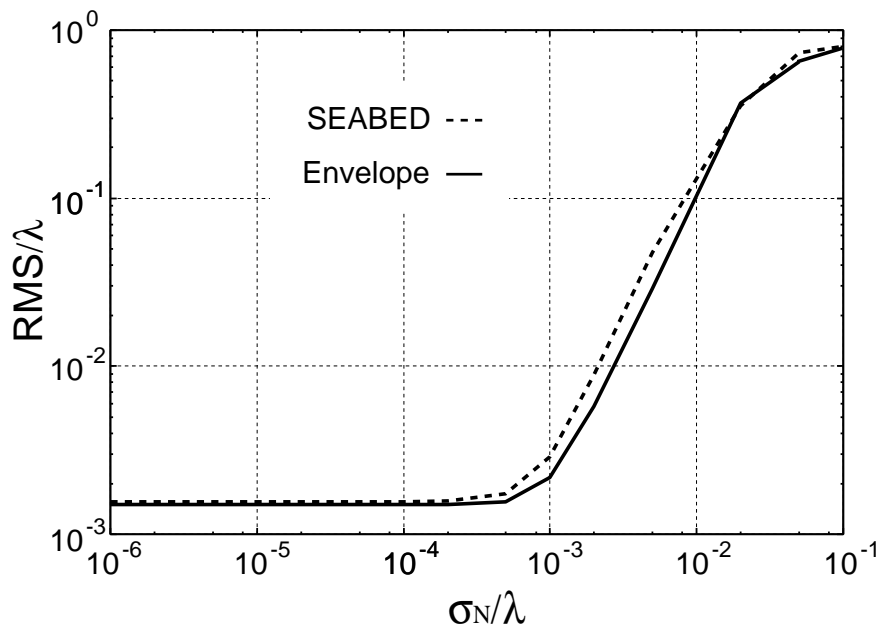
Figure 3.17: Relationship between RMS and σ_N for a concave target.
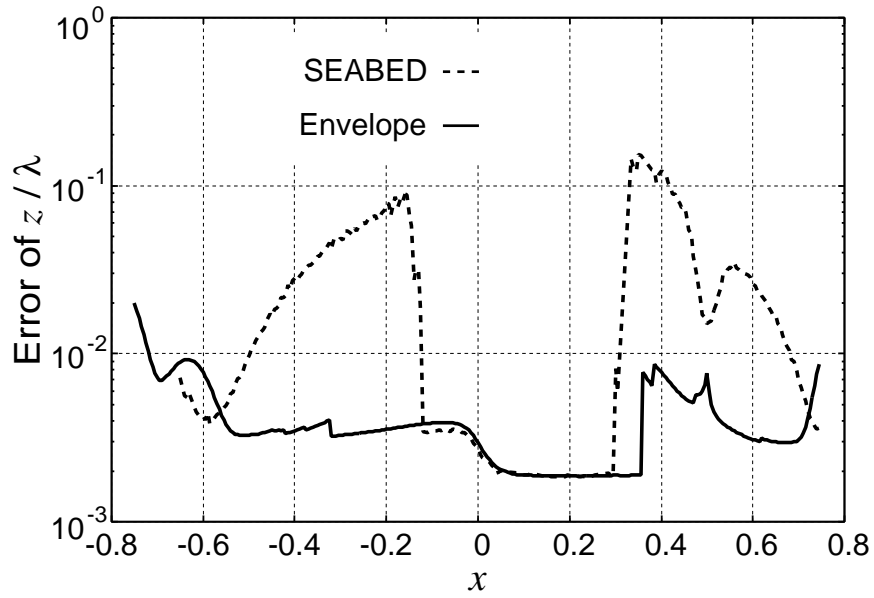
Figure 3.18: Estimation error of z for each x in a convex target ($\sigma_N = 5.0 \times 10^{-3}\lambda$).
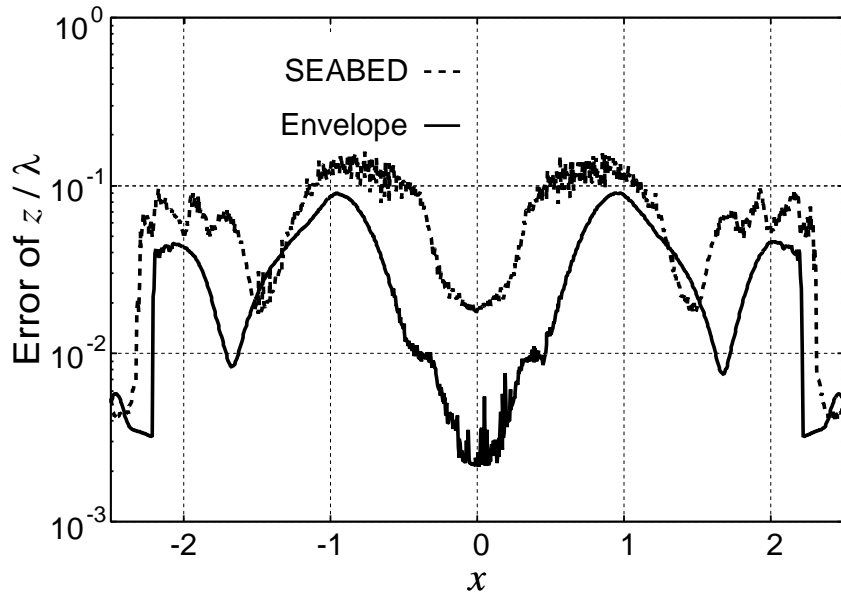
Figure 3.19: Estimation error of z for each x in a concave target. ($\sigma_N = 5.0 \times 10^{-3}\lambda$).
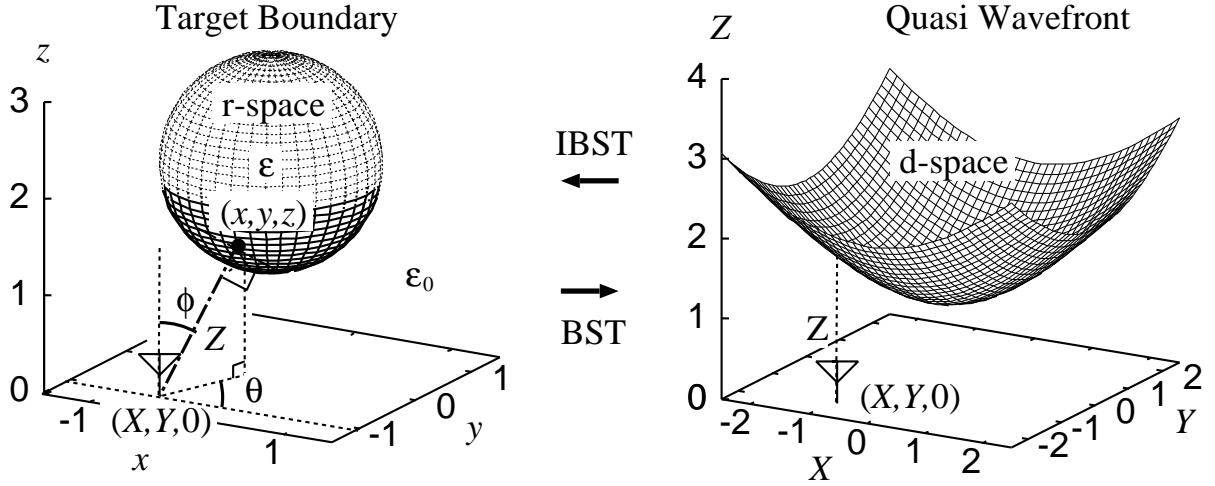
Figure 3.20: Relationship between target boundary in r-space and quasi wavefront in d-space.

3.3   3-D Problem

3.3.1   Noise Tolerance of SEABED

The left side of Fig. 3.20 shows the system model. We utilize the same system model as described in Sec.1.5.6. The right side of Fig. 3.20 shows the quasi wavefront in the mono-static model. SEABED utilizes a reversible transform BST between the point of r-space (x, y, z) and the point of d-space (X, Y, Z). BST and IBST are expressed in Eqs. (1.42) and (1.43), respectively. While SEABED achieves a high-speed 3-D imaging, the estimated image with this method is extremely instable due to the derivative operations in a noisy environment. This section shows a demonstration and an analysis for the instability with SEABED. We scan the antenna at the range for $-2.5\lambda \leq x \leq 2.5\lambda$ $-2.5\lambda \leq y \leq 2.5\lambda$, and take a received data at 41 locations for each axis. We assume the target boundary as the left side of Fig. 3.20. The left side of Fig. 3.21 shows d-space where we give a white noise to the true quasi wavefront. The standard deviation of the noise is 0.15λ. We smooth the quasi wavefront with the Gaussian filter, whose correlation length is 0.05λ. The right hand side of Fig. 3.21 shows the estimated boundary with SEABED. This figure shows that there are many points which is far from the true boundary points, in spite that we give the minute errors to the quasi wavefront. This is because the fluctuation of the quasi wavefront is enhanced with derivative operations. For an analysis of these
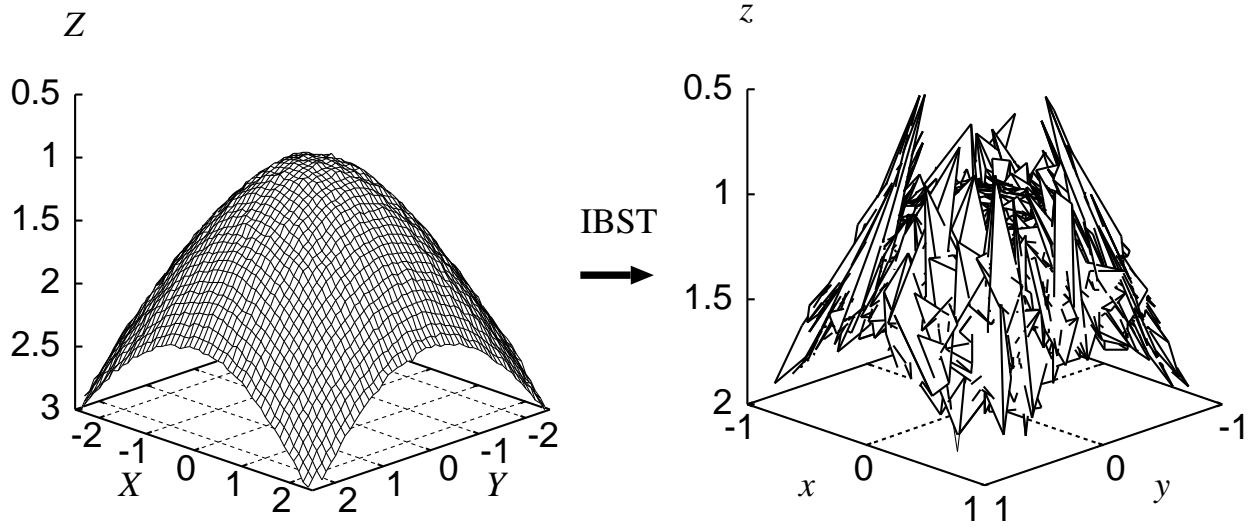
Figure 3.21: Quasi wavefront with white noise (left) and estimated image with SEABED (Right) ((X, Y, Z) is known).

errors, we rewrite IBST as

$$\left.\begin{array}{rcl} x & = & X + Z\cos\theta\sin\phi \\ y & = & Y + Z\sin\theta\sin\phi \\ z & = & Z\cos\phi \end{array}\right\}, \tag{3.11}$$

$$\theta = \angle(-\partial Z/\partial X - \mathrm{j}\partial Z/\partial Y), \quad (-\pi < \theta \le \pi),$$

$$\phi = \cos^{-1}\sqrt{1 - (\partial Z/\partial X)^2 - (\partial Z/\partial Y)^2}, \quad (0 < \phi \le \pi/2),$$

where θ and ϕ are expressed as shown in the left hand side of Fig. 3.20. Eq. (3.11) shows that each estimated point with IBST exists on the sphere whose center is $(X, Y, 0)$ and radius is Z. The accuracy for θ and ϕ depends on that of $\partial Z/\partial X$ and $\partial Z/\partial Y$. Thus, the estimated point readily moves around the sphere with the fluctuation of quasi wavefront. While the adaptive smoothing method has been developed [130], there is a trade-off between the stability and the resolution of the image for the same reason of 2-D problem.

3.3.2 Target Boundary and Envelopes of Spheres

To resolve the problem described in the previous section, we propose a robust and fast imaging algorithm without derivative operations as follows. This algorithm utilizes the principle that the target boundary should be expressed as the envelope of the spheres,

67
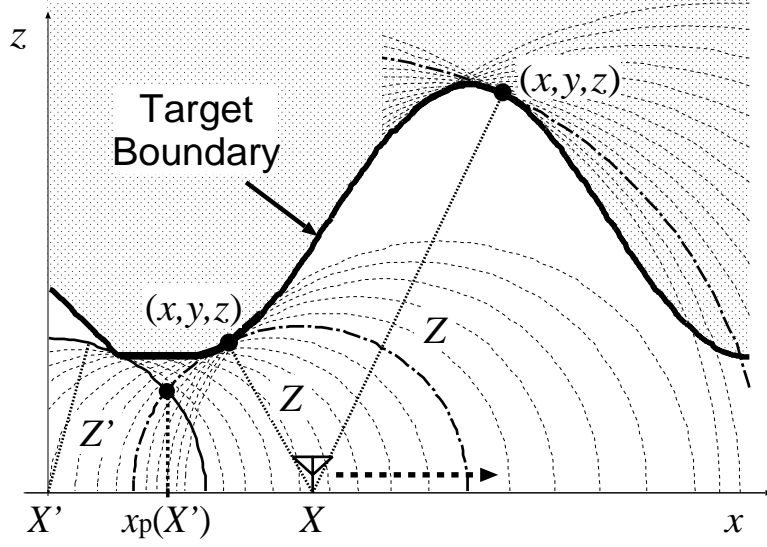
Figure 3.22: Cross section of the target boundary and an envelope of spheres.

whose center point is $(X, Y, 0)$, and radius is Z. Fig. 3.22 shows the cross section of the target boundary and an envelope of the spheres, for simplicity. As shown in Fig. 3.22, we confirm that the envelope of the circles should circumscribe or inscribe to the target boundary for each axis. By extending this relationship to 3-D problems, we determine the region of the target boundary (x, y, z) for each (X, Y, Z) as

$$
\begin{cases}
\max\limits_{s_X(X'-X)<0} x_{\mathrm{p}}(X') \leq x \leq \min\limits_{s_X(X'-X)>0} x_{\mathrm{p}}(X') \\
\max\limits_{s_Y(Y'-Y)<0} y_{\mathrm{p}}(Y') \leq y \leq \min\limits_{s_Y(Y'-Y)>0} y_{\mathrm{p}}(Y') \quad , \\
z = \sqrt{Z^2 - (x-X)^2 - (y-Y)^2}
\end{cases}
\tag{3.12}
$$

where $s_X = \mathrm{sgn}(\partial x/\partial X)$, $s_Y = \mathrm{sgn}(\partial y/\partial Y)$, and X', Y' are searching variables. $x_{\mathrm{p}}(X')$ and $y_{\mathrm{p}}(Y')$ are the intersection points of the estimated circles on the plane $y = Y$ and $x = X$, respectively, as shown in Fig. 3.22. s_X and s_Y express the situation that the envelope of circles circumscribe or inscribe to the target boundary in each plain. The signs of s_X and s_Y can be determined with Proposition 1 in Sec. 3.2.3, respectively, for the each cross section plane. This method estimates the tangent planes of the target boundary as that of outer or inner envelopes of the spheres. Thus, the instability caused by noise is suppressed. Eq. (3.12) determines the part of target boundary as the part of the envelope of spheres.

Procedures of Envelope

We show the procedure of Envelope method as follows. $i = 0$ is set.

Step 1). Obtain the output of the matched filter as $s(X, Y, Z')$ with received signals $s'(X, Y, Z')$ in each antenna location.

Step 2). Extract quasi wavefronts as (X, Y, Z'') which satisfies $\partial s(X, Y, Z')/\partial Z' = 0$, $s(X, Y, Z') \geq \alpha \max_{Z'} s(X, Y, Z')$. Extract (X, Y, Z) as ∂D_{T} from (X, Y, Z''), which satisfies the local maximum of Z'' for each X and Y. Parameter α and the searching region of Z'' are determined empirically.

Step 3). Remove interfered points from ∂D_{T}, which have plural connecting candidates around themselves, and the remained points are defined as ∂D_r.

Step 4). Extract a set of (X, Y, Z) as ∂D_i from ∂D_{r}, which is a single-valued and continuous function of X and Y, and also $(\partial Z/\partial X)^2 + (\partial Z/\partial Y)^2 \leq 1$ is satisfied.

Step 5). For each (X, Y, Z), determine the signs of $\partial x/\partial X$ and $\partial y/\partial Y$ with Prop. 1 in each cross section plane $y = Y$ and $x = X$ of ∂D_i, respectively.

Step 6). Determine the target boundary as $(x, y, x) \in \partial T_i$ by applying Eq. (3.12) to all $(X, Y, Z) \in \partial D_i$. Set $\partial D_r = \partial D_{\mathrm{r}}/\partial D_i$.

Step 7). If ∂D_r is not empty, set $i = i + 1$ and return to the Step 4). Otherwise, estimate the target boundary as $\partial T = \bigcup_i \partial T_i$.

Fig. 3.23 shows the procedures of Envlope method. This method can determine the target boundary for arbitrary shapes without derivative operations.

3.3.3 Application Examples with Numerical Simulations

The performance evaluation is presented as follows. Fig. 3.24 shows the estimated boundary with Envelope, which can be determined with the same quasi wavefront in Fig. 3.21. It verifies that the obtained image is stable and, can reconstruct the smoothed surface on the target. Next, let us show the example of the concave shape target as shown in the upper left side of Fig. 3.23. We give random errors to the true quasi wavefront, whose standard deviation is $7.0 \times 10^{-3}\lambda$, which corresponds to S/N = 24 dB. The antenna is scanned for $-2.5\lambda \leq x \leq 2.5\lambda$, and $-2.5\lambda \leq y \leq 2.5\lambda$. Figs. 3.25 and 3.26 show the estimated images with SEABED and Envelope, respectively. We confirm that the image with SEABED is instable, especially around the concave region due to the derivative of the quasi wavefront. Contrarily, the image with Envelope is quite stable for all regions of the target boundary even in the noisy case. This is because this method absorbs the instability of the derivative operations with the wider information of a quasi wavefront. In addition, we show the examples of Envelope method, where the received signals are calculated with FDTD method in noiseless environment. Fig. 3.26 shows the estimated image with Envelope, and the estimated points on the concave boundary has large offset errors
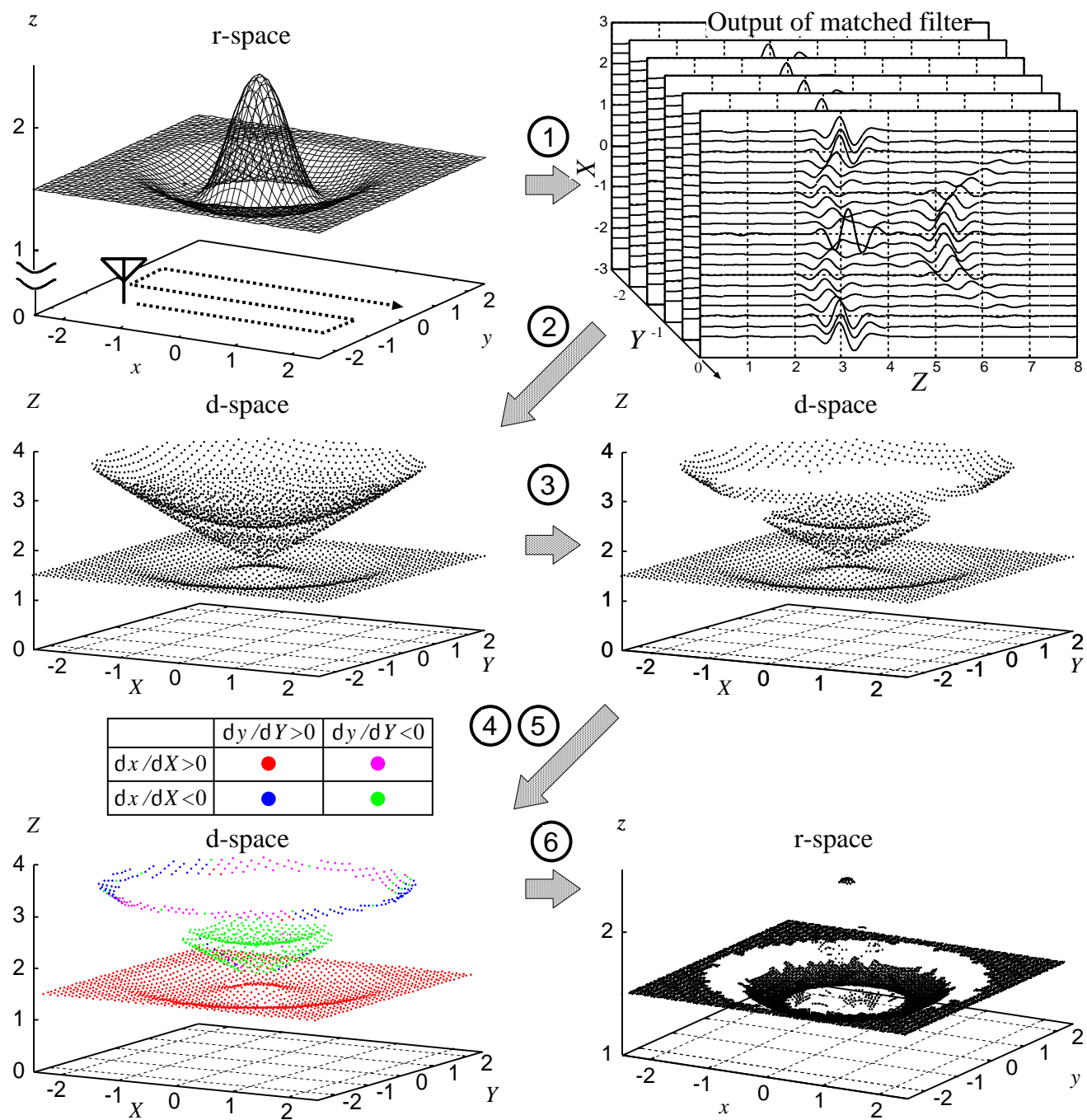
Figure 3.23: The procedures for Envelope method.
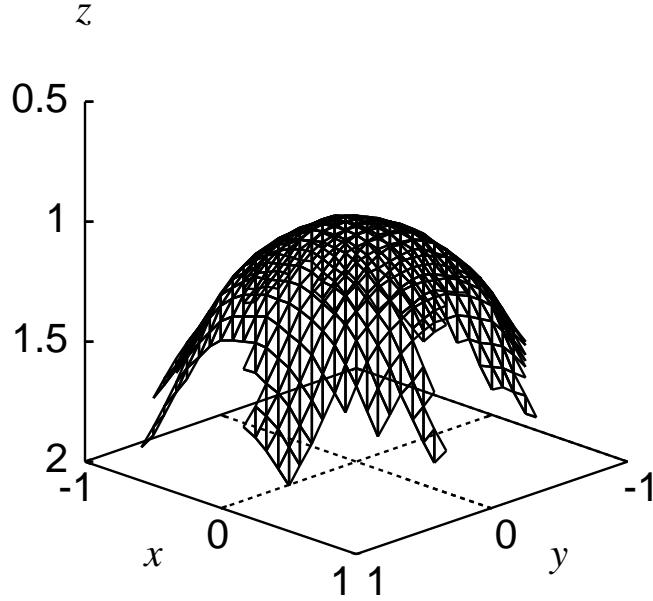
Figure 3.24: The estimated image with Envelope for a convex target.

	$\partial x/\partial X > 0$	$\partial x/\partial X < 0$
$\partial y/\partial Y > 0$	0	$\pi/2$
$\partial y/\partial Y < 0$	$\pi/2$	π

Table 3.1: Relationship between the signs of $\partial x/\partial X$ and $\partial y/\partial Y$, and the phase rotation of scattered waves.

based on the phase rotations of the scattered waves. It is caused by the situation that that scattered waves pass through the caustic points, as described in Sec. 1.3.4. The signs of $\partial x/\partial X$ and $\partial y/\partial Y$ inform us the number of caustic points which scattered wave passed through. Moreover, this method can recognize these types of phase rotations, which can be determined with the signs of $\partial x/\partial X$ and $\partial y/\partial Y$. Table 3.1 shows the relationship of the signs of $\partial x/\partial X$ and $\partial y/\partial Y$, and the phase rotations. If both signs of $\partial x/\partial X$ and $\partial y/\partial Y$ are negative, there are π phase rotation for the scattered waveform, for example. Fig. 3.28 shows the estimated image after the compensation of the phase rotations. This figure shows that the estimated image can express the accurate target boundary, even in the concave target. The computational time of this method is within 0.2 sec for Xeon 3.2 GHz processor, which can realize a real-time operations.

3.4   Conclusion

This section describes newly developed imaging algorithm, which can realize robust and fast imaging in 2-D and 3-D problems. We clarified that convex and concave target boundaries can be expressed as inner and outer envelopes of the circles, respectively, in 2-D problems. This principle can be extended to 3-D problems, where the target boundary can be expressed as the envelopes of spheres. We can robustly determine whether the obtained spheres should inscribe or circumscribe to the target boundary for each axis. It enables us to deal with an arbitrary target shape and automatically compensate the phase rotations of scattered waves caused by passing through the caustic points. Numerical simulation verified that Envelope can estimate images that be more stable and accurate than those obtained with SEABED. Furthermore, it can realize high-speed imaging like with SEABED. However, we confirmed that the estimated image with Envelope distorts around the edge region due to waveform deformations. In the next chapter, we challenge to resolve these deteriorations.
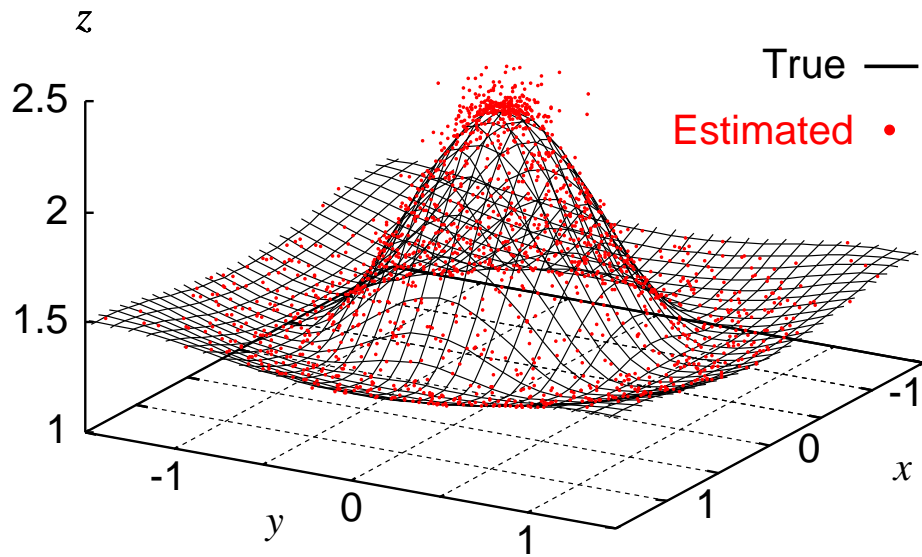
Figure 3.25: The estimated image with SEABED in noisy case $((X, Y, Z)$ is known).
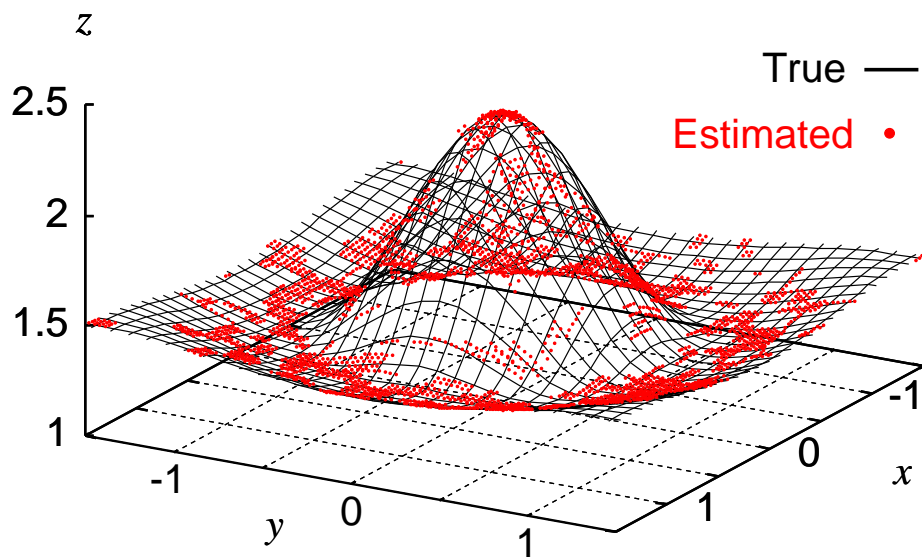
Figure 3.26: The estimated image with Envelope in noisy case $((X, Y, Z)$ is known).

73
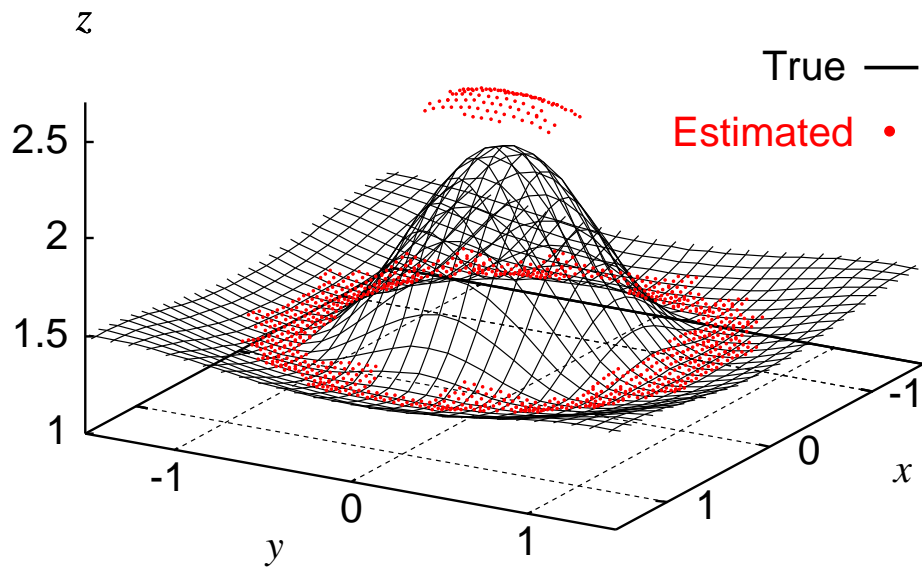
Figure 3.27: The estimated image with Envelope before phase compensations ((X, Y, Z) is unknown).
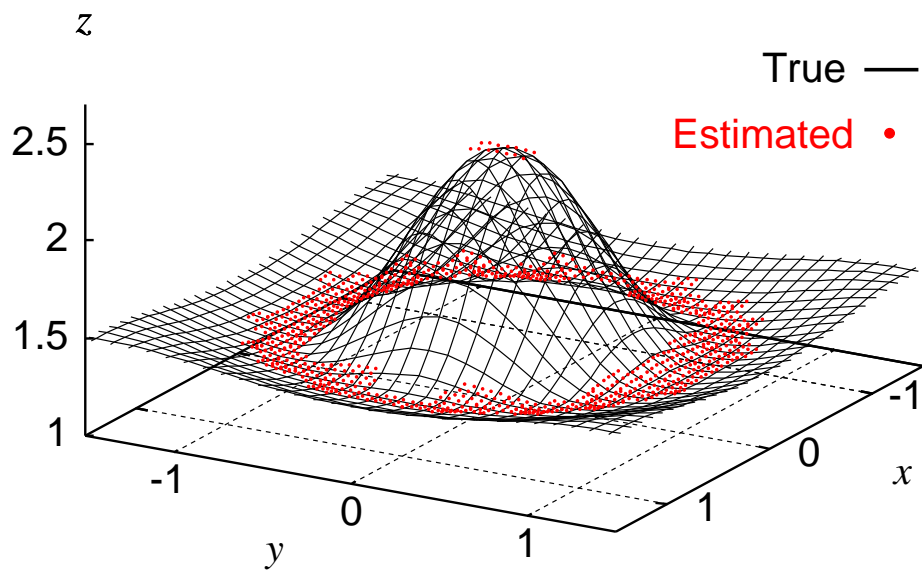
Figure 3.28: The estimated image with Envelope after phase compensations ((X, Y, Z) is unknown) .

74

Chapter 4

Accurate Imaging Algorithm by Compensating Waveform Deformations

4.1   Introduction

We have proposed robust and rapid 3-D imaging algorithm with an envelope of spheres as Envelope in Chap. 3. However, the estimated image with this method distorts around the target edges due to scattered waveform deformations. We confirm that the maximum error caused by those deformations goes up to $1/10$ of the center wavelength. This is due to the assumption that the scattered waveform is the same as the transmitted one. In general, the cost of the lower-frequency component is low compared to that of the higher-frequency one. This is a reason why we need to enhance the accuracy of the image in 2-D problem. This section describes a shape estimation method with a waveform estimation in order to enhance the resolution of the image. We utilize a fast and simple waveform estimation algorithm based on the Green's function integral, which does not spoil the rapidness of the shape estimation. It can deal with general convex targets including smooth curves and edges. Numerical simulations and experiments show that this method accomplishes an accurate and high-resolution imaging in 2-D problems.

However, in 3-D problem, this method requires an large computation for the waveform estimation, because it needs numerical integrals of the target surface for each antenna location. The calculation time of this method is more than 10 sec, which cannot be suitable for a realtime imaging. To realize a high-speed imaging, we propose accurate 3-D imaging algorithm without the waveform estimation for general convex targets. This method utilizes the center frequencies of scattered waveforms and success to compensate the error of the quasi wavefront without a recursive manner. In numerical simulations, the effectiveness of this method is confirmed.
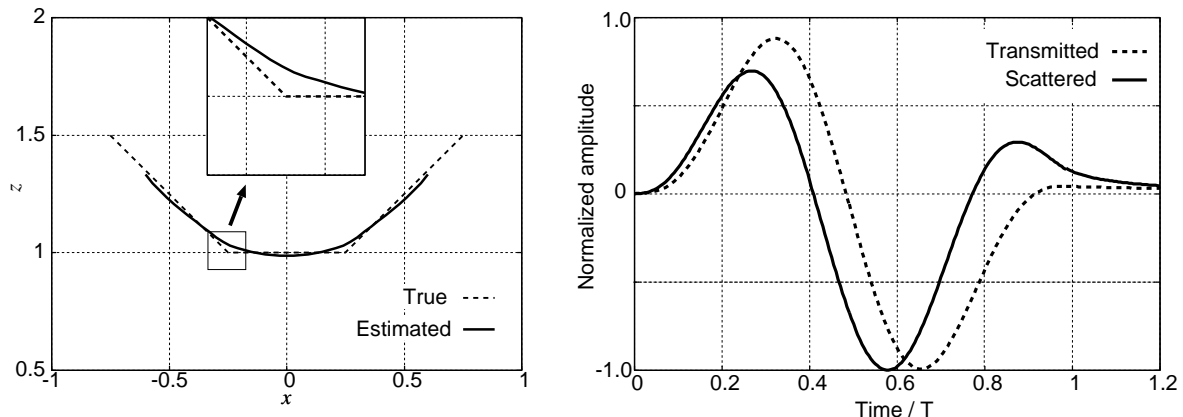
Figure 4.1: Estimated image with Envelope (left), and transmitted and scattered waveforms (right).

4.2 Accurate Imaging Algorithm with Waveform Estimation for 2-D Problem

4.2.1 Image Distortions due to Waveform Deformations

We utilize the same system model as introduced in Sec. 3.2.1. We have already introduced robust and fast imaging algorithm with an envelope of circles as Envelope in Chap. 3. It reveals that the points on the target boundary should be expressed as the points on the envelope of circles with the radius of Z and the center $(X, 0)$ for the quasi wavefront. The left hand side of Fig. 4.1 shows the application example with Envelope in noiseless case, where the received signals are calculated with FDTD method. As shown in this figure, the resolution of the estimated image distorts around the edges, and the error around this region is 0.07λ. These deteriorations are caused by the following reasons. In general, the scattered waveform from a large planar boundary whose length is much longer than the wavelength has the same waveform as the transmitted one with the opposite sign. However, the scattered waveform from edge or ridge point of a target is different from a waveform of the transmitted one. The scattered waveform from a general convex target is a complex one influenced by these effects. The right hand side of Fig. 4.1 shows the transmitted and scattered waveform from the edge point. Thus, the resolution around target edges distorts because we utilize the filter matched with the transmitted waveform. To resolve this problem, we synthesize the shape and waveform estimation, which corresponds to solve the inverse and direct problems recursively. Fig. 4.2 shows an each principle of Envelope and Envelope with the waveform estimation method, respectively.

76
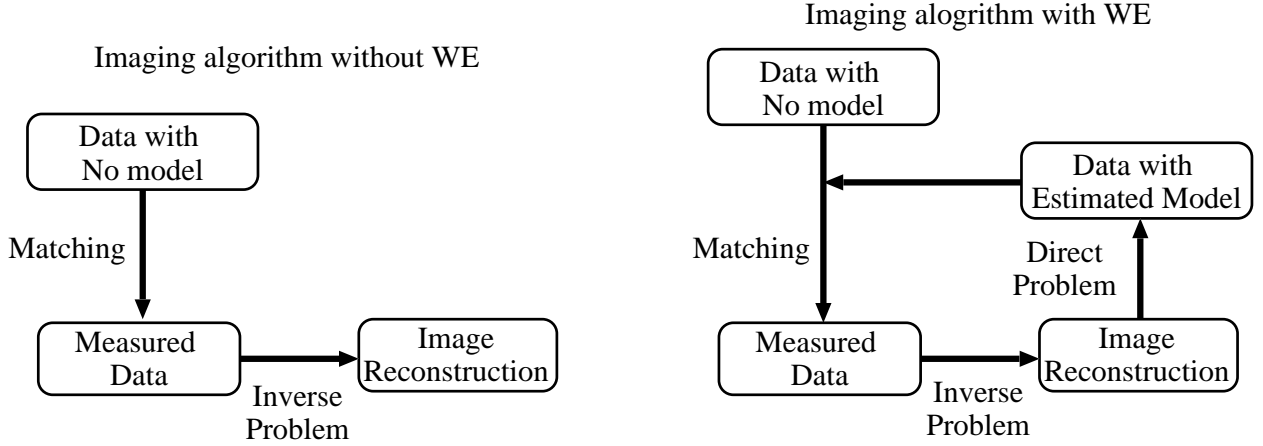
Figure 4.2: Principles of Envelope (left) and Envelope with waveform estimations (right).

4.2.2 Waveform Estimation Based on the Green's Function Integral

In this section, we present the waveform estimation algorithm for the accurate imaging method. In general, the specular reflection waveform from the planar boundary whose width is on the order of the wavelength is different from the transmitted one. This is because the Fresnel zone size in a high frequency band is smaller than one in a low frequency band. Many methods for the waveform estimation have been proposed, as described in Sec. 1.3.4, such as FDTD method and Physical Optics method. FDTD method achieves the high accuracy of the waveform estimation, but requires an intensive computation, which spoils the advantage of the quick imaging of our method. On the other hand, Physical Optics method achieves a fast waveform estimation. However we confirm that this method has an estimation error for the edge diffraction waveform estimation for the current situation. To accomplish a fast and an accurate waveform estimation, we utilize the Green's function integral as follows.

At first, let us consider the electric-field waveform after propagating through a finite aperture. This model is an approximation of the scattering from a rectangular target. We assume that the waveform which passed through the finite rectangular aperture can be regarded as the approximation of the scattered waveform with the opposite sign from a rectangular perfect electric conductor plate whose size is the same as that of the aperture. We assume the coordinates shown in Fig. 4.3 and set the rectangular aperture on the plane $y = 0$. We set the transmitted and received antenna at $(0, -r, 0)$ and $(0, r, 0)$, respectively. We assume that r is longer enough than the wavelength. Under this assumption, the electric field of the wave propagating through an aperture in a 3-D problem is
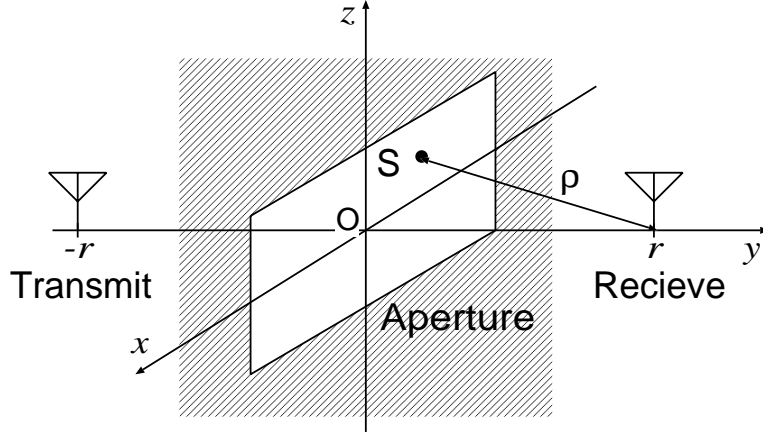
Figure 4.3: Arrangement of the antenna and the rectangular aperture in 3-D model.

approximated by the following equation [133].

$$\boldsymbol{E}(r) \simeq \frac{\mathrm{j}k}{2\pi}\boldsymbol{E}_0' \int_S g(2\rho)\mathrm{d}S, \tag{4.1}$$

where S is the surface of the aperture, g is the Green's function, ρ is the distance from the aperture to the received antenna, $\boldsymbol{E}(r)$ is the electric field at the received antenna, and $\boldsymbol{E}_0'$ is the electric field on the aperture, respectively. This approximation does not include the influences of the scattered waves due to induced current at the edge of the aperture. However, these influences become small except for the region near the edge. In 2-D problem and TE mode waves, we assume that the length of the aperture along z axis is infinite. In this model, we approximate the electric field of the received antenna as

$$E(r) \simeq \sqrt{\frac{\mathrm{j}k}{2\pi}}E_0' \int_l g(2\rho)\mathrm{d}s, \tag{4.2}$$

where $E(r)$ is the amplitude of z component of the entire electric field at $(0, r, 0)$. E_0' is that on the aperture. l is the range of the aperture boundary. g is the Green's function of 2-D problem as given by $g(\rho) = \frac{\mathrm{i}}{4}H_0^{(2)}(k\rho)$, where $H_0^{(2)}(*)$ is the 0th order Hankel's function of the 2nd kind. We expand this principle to the scattered waveform estimation. We utilize E_0 in stead of E_0', which expresses the electric field of the transmitted waveform, and approximate the scattered waveform from the finite plate as

$$E(r) \simeq K\sqrt{\mathrm{j}k}E_0 \int_l g(2\rho)\mathrm{d}s, \tag{4.3}$$

where K is a constant.

78
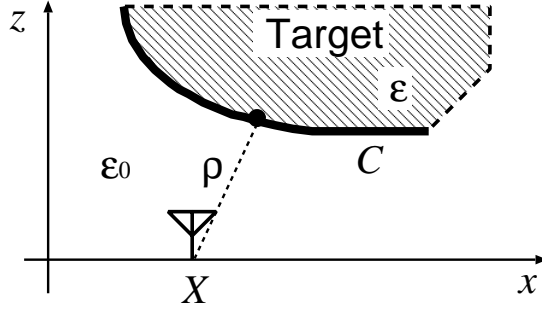
Figure 4.4: Arrangement of the antenna and the convex target.

By expanding this principle to general convex targets, we calculate the transfer function with the integral of the Green's function along target boundaries which dominantly contribute to the scattering. Fig. 4.4 illustrates the antenna location and the target boundary. The scattered waveform $F(\omega, X)$ in the frequency domain at the location X is approximated as

$$F(\omega, X) = \sqrt{\frac{\mathrm{j}k}{2\pi}} E_0(\omega) \int_C g(2\rho) \, \mathrm{d}s, \tag{4.4}$$

where C is the integration path $E_0(\omega)$ is the transmitted waveform in the frequency domain. Here, we approximate the edge diffraction waveform as the summation of the two specular reflection waveforms from the planar boundaries making the edge. This method enables us to compensate the frequency change depending on the Fresnel zone size in each frequency. Although this method is not a strict solution of the scattered waveforms, the accuracy is enough for our application.

4.2.3 Examples of Waveform Estimation for Convex Targets

Examples of the waveform estimation are presented to evaluate the accuracy for the estimated quasi wavefront of the convex target. Figs. 4.5 and 4.6 show the error of the quasi wavefront for each antenna location with the matched filter for the transmitted and estimated waveform, respectively. The accuracy of the quasi wavefront with the estimated waveform is within $0.01\lambda/c$ around the edges. This level of accuracy cannot be obtained with the transmitted waveform. Also the waveform estimation is effective for any antenna location except for the upper left side of Fig. 4.6. In this region, the upper side of the target boundary strongly contributes the scattered waveform, which is a shadow region in Eq. (4.4). Additionally, Fig. 4.7 shows the transmitted and estimated waveform at the antenna location at $(x, y) = (4.0\lambda, 1.0\lambda)$. This figure confirms that Eq. (4.4) correctly compensates for the scattered waveform distortions. The computational time of this
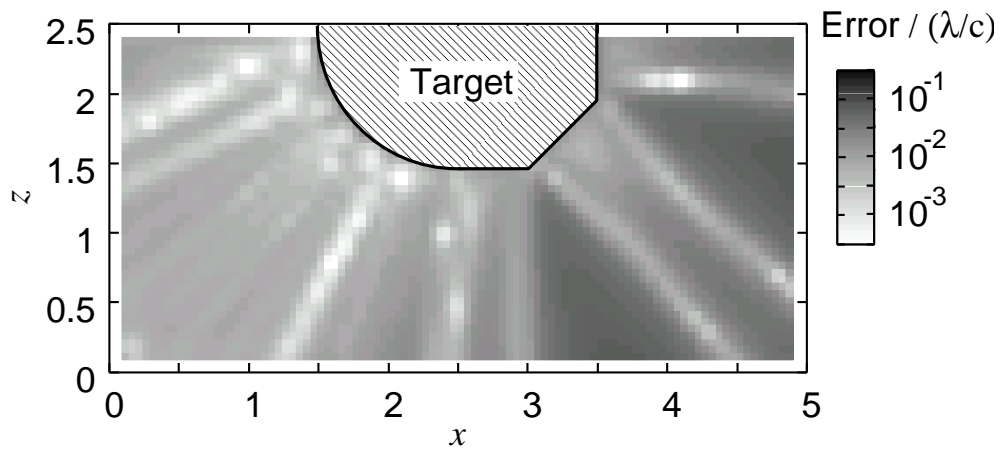
Figure 4.5: Accuracy for extracted quasi wavefront with the transmitted waveform.
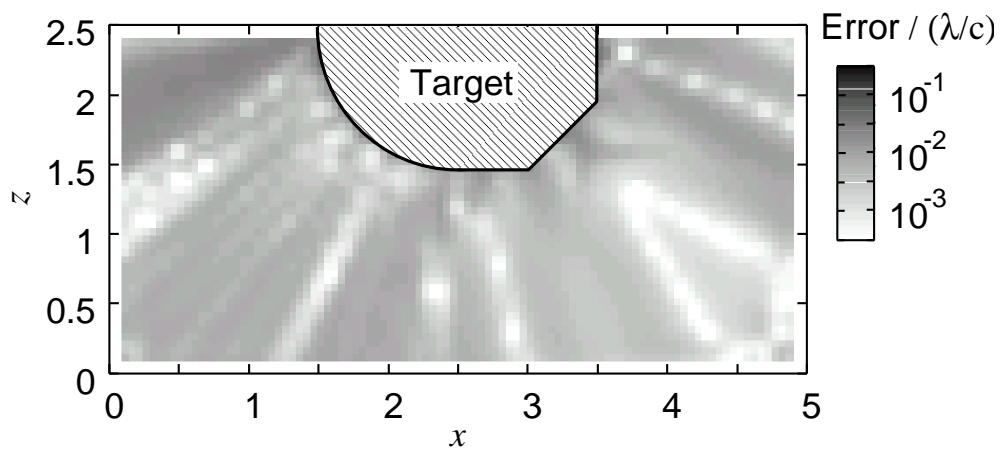
Figure 4.6: Accuracy for extracted quasi wavefront with the estimated waveform.
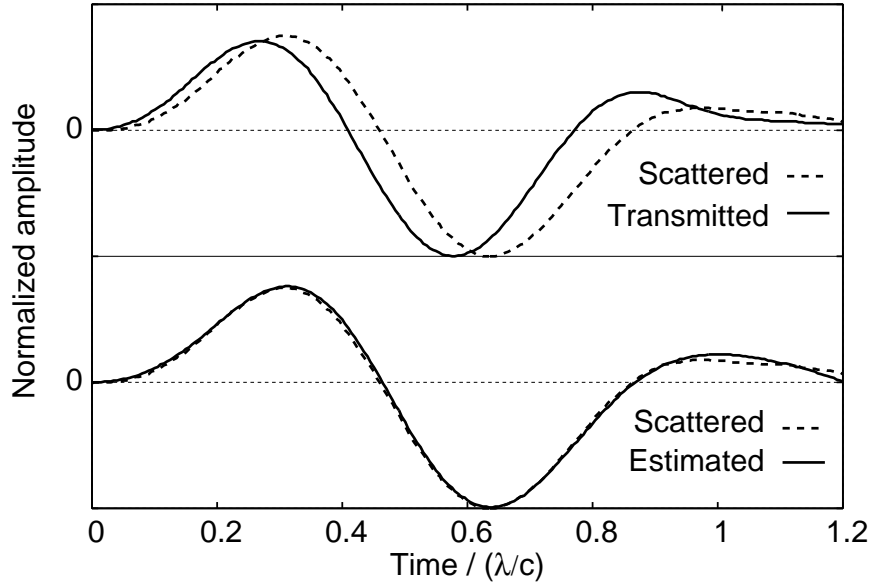
Figure 4.7: Examples of the scattered and estimated waveforms.

method is within 5.0 msec for each antenna location with a Xeon 3.2 GHz processor, which does not spoil the high-speed of the shape estimation.

4.2.4 Procedure of Envelope+WE

The actual procedure of the imaging method with the waveform estimation is explained as follows. $X_{\min}$ and $X_{\max}$ are defined as the minimum and the maximum X, respectively. We define the target boundary and the quasi wavefronts as C_0 and $Z_0(X)$, respectively, which are estimated with Envelope.

Step A). Estimate an initial target boundary with Envelope method. Set $i = 1$, where i is the iteration number.

Step B). Calculate the waveform for each X as

$$F_i(X, \omega) = \sqrt{\frac{\mathrm{j}k}{2\pi}} E_0(\omega) \int_{C_{i-1}} g(2\rho)\mathrm{d}s. \tag{4.5}$$

where C_{i-1} is the estimated boundary for $i - 1$ th iteration.

Step C). Update the output of the matched filter as

$$s_i(X, Z') = \int_{-\infty}^{\infty} S'(X, \omega) F_i(X, \omega)^* \mathrm{e}^{\mathrm{j}\omega 2Z'} \mathrm{d}\omega, \tag{4.6}$$

81
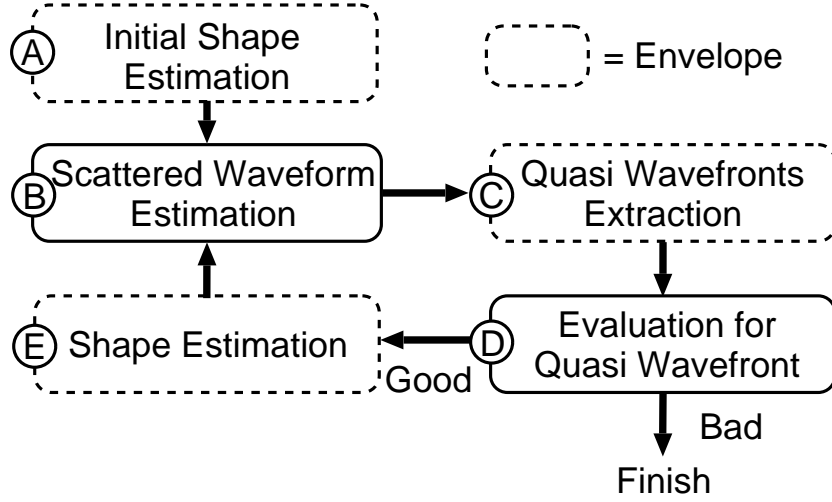
Figure 4.8: Flowchart of Envelope+WE.

where $S'(X, \omega)$ is the received signal in the frequency domain. Extract the quasi wavefront for i th iteration as

$$Z_i(X) = \arg \max_{Z'} s_i(X, Z').$$
(4.7)

Step D). Evaluate the updated quasi wavefront with the evaluation value ΔQ_i defined as

$$\Delta Q_i = \frac{\int_{X_{\min}}^{X_{\max}} |Z_i(X) - Z_{i-1}(X)| \, \mathrm{d}X}{\int_{X_{\max}}^{X_{\min}} \mathrm{d}X}.$$
(4.8)

The following equation is applied

$$\Delta Q_i < \begin{cases} \epsilon & (i = 1), \\ \Delta Q_{i-1} & (i \geq 2). \end{cases}$$
(4.9)

Step E). If the equation holds true, we update the target boundary $(x, z) \in C_i$ as

$$z = \max_X \sqrt{Z_i(X)^2 - (x - X)^2},$$
(4.10)

set $i = i+1$, and return to the Step B). Otherwise, we complete the shape estimation. ϵ is set empirically.

For successive iteration, ΔQ_i is assumed to become smaller, and Step E.) prevents the incorrect divergence of the estimated image with the iteration. By this procedure, the estimated waveform approaches to the true one. This improvement can enhance the resolution of the target shape. We call this method as Envelope+WE. Fig. 4.8 shows the flowchart of Envelope+WE.

82

4.2.5 Examples of Shape Estimation with Numerical Simulations

In this section, we verify the effectiveness of Envelope+WE with numerical simulations as follows. The left and right side of Fig. 4.9 show the output of the matched filter and the quasi wavefront with each method. $\epsilon = 0.01\lambda$ is set empirically, and the number of the iteration is 4. Envelope+WE accomplishes the 5 times improvement for the accuracy of the quasi wavefront than Envelope. Fig. 4.10 shows the estimated image with Envelope+WE. The target boundary, including the edges, is expressed more accurately compared to Fig. 4.1. This is because the estimated quasi wavefront is close to the true one with Envelope+WE. In addition, the estimated accuracy at the edge is within 0.01λ, which is 7 times more accurate than Envelope. Furthermore, let us evaluate a curvature of the target boundary, which is expressed as

$$\kappa \;=\; \frac{\mathrm{d}^2 z/\mathrm{d}x^2}{(1 + (\mathrm{d}z/\mathrm{d}x)^2)^{3/2}}. \tag{4.11}$$

Here a difference approximation is used to calculate $\mathrm{d}z/\mathrm{d}x$ and $\mathrm{d}^2 z/\mathrm{d}x^2$. Fig 4.11 shows the estimated curvatures with each method. This figure shows that the curvature of Envelope is not accurate for the edges. On the contrary, the estimated κ with Envelope+WE is more accurate, and we see the two edges clearly.

Next, we discuss the estimation accuracy in a noisy environment. We introduce the evaluation value μ as

$$\mu = \frac{\sqrt{\int_{x_{\min}}^{x_{\max}} \{f_{\mathrm{t}}(x) - f_{\mathrm{e}}(x)\}^2 \mathrm{d}x}}{\sqrt{\int_{x_{\min}}^{x_{\max}} f_{\mathrm{t}}(x)^2 \mathrm{d}x}} \tag{4.12}$$

where $f_{\mathrm{t}}(x)$ and $f_{\mathrm{e}}(x)$ are the true and estimated target boundaries, respectively, and $x_{\min}$ and $x_{\max}$ are minimum and maximum x for the estimated boundary. Fig. 4.12 shows μ of the estimated boundary to S/N ratio. S/N is defined in Eq. (3.10). As shown in this figure, the 6 times improvement is obtained for the accuracy compared to Envelope for S/N $\geq$ 50 dB. It also confirms us that Envelope+WE is effective for S/N $\geq$ 30 dB. These conditions are quite realistic because we utilize coherent averaging for radar systems.

Furthermore, we examine examples in the case of the target with both smooth curves and an edge. Figs. 4.13 and 4.14 show the estimated images with Envelope and Envelope+WE, respectively. As shown in these figures, a more accurate image can be obtained around the edges and the smooth curve of the target with Envelope+WE. These results show that Envelope+WE can be applied to the general curved target. The calculation time for this method is 2.0 sec with a single Xeon 3.2 GHz processor.

4.2.6 Examples of Shape Estimation with Experiments

In this section, let us investigate the performance of our algorithm with the experiments. We utilize the same signal and antenna settings as described in 2.3.4. The target is made
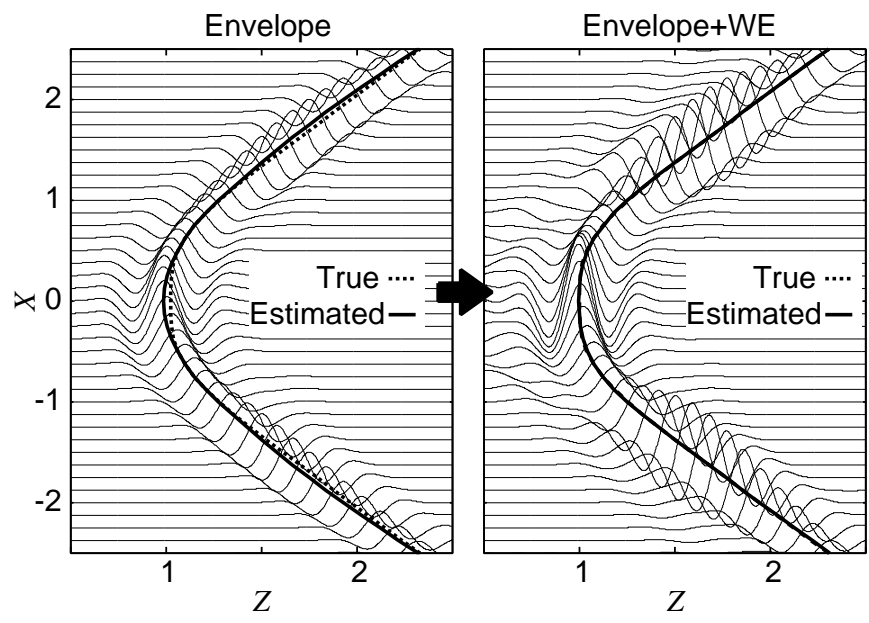
Figure 4.9: Output of the filter and extracted quasi wavefront with each method.

Figure 4.10: Estimated image with Envelope+WE.

84
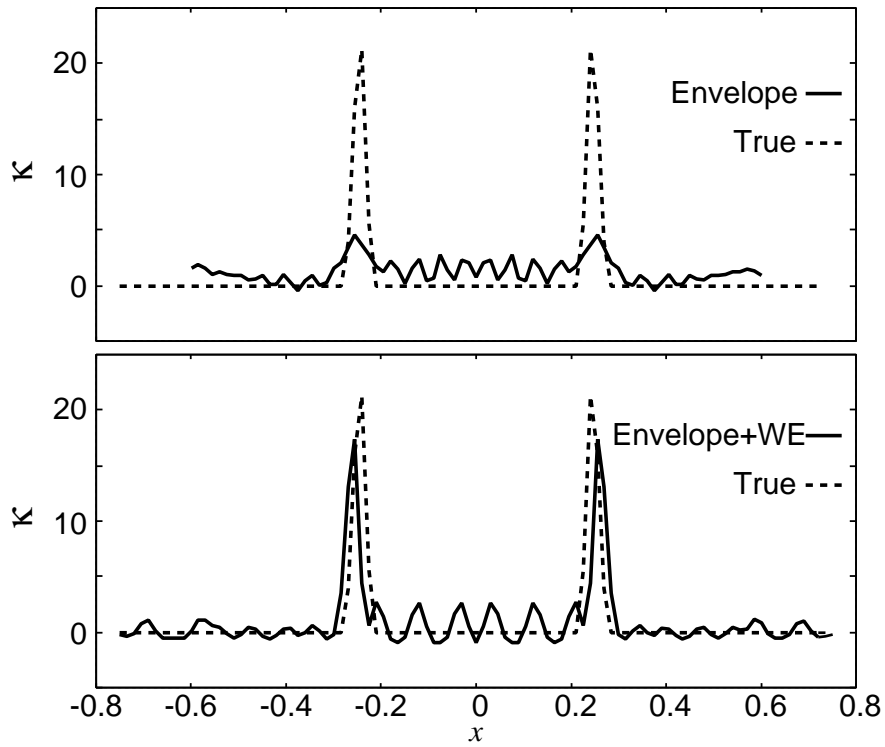
Figure 4.11: Estimated curvatures with Envelope (upper) and Envelope+WE (lower).

Figure 4.12: Estimation accuracy of the estimated image for S/N.

85
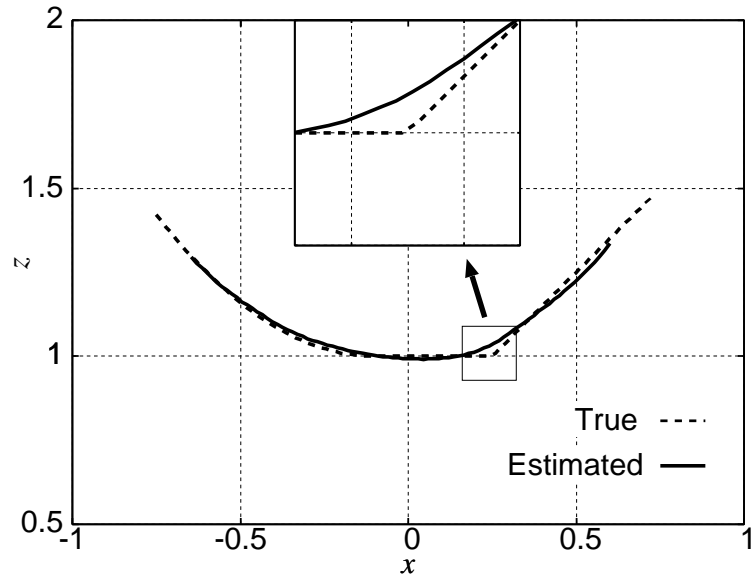
Figure 4.13: Estimated image with Envelope for the curved target.
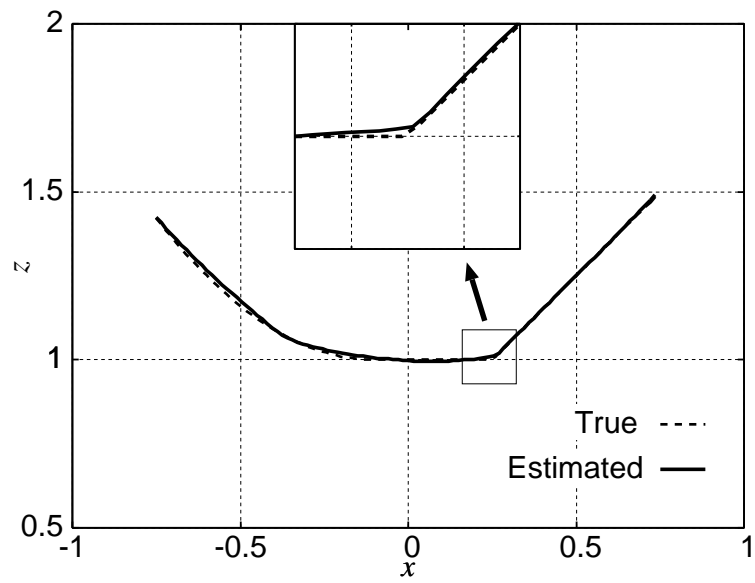
Figure 4.14: Estimated image with Envelope+WE for the curved target.
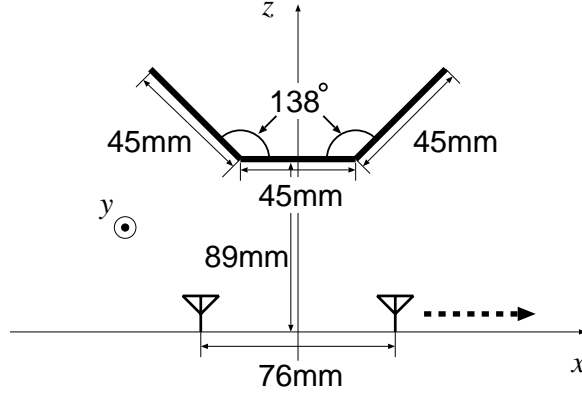
Figure 4.15: Arrangement of bi-static antennas and targets in experiments.

of stainless steel sheet. Fig. 4.15 illustrates the location of the antenna and the target. We utilize two antennas whose separation in x-direction is 76 mm, which corresponds to 0.835 center wavelength of 91mm. The antenna location $(X, 0, 0)$ is defined as the center point of the two antennas. The target is set with a sufficiently long span in the y direction, compared to the center wavelength in order to obtain the data for the 2-D problem. Additionally, the multiple scattered waveforms are integrated with a common midpoint for fixed $(X, 0, 0)$, as the 2-D waveform $R(X, t) = \sum_{i=0}^{N} r(X, y_i, t)$, where $r(X, y_i, t)$ is the scattered waveform from the transmitting point $(X, y_i, 0)$ to the receiving point $(X, 0, 0)$, N is fixed to 40, and the sampling interval is fixed to 10 mm. Fig. 4.29 shows the arrangement of the pair antennas and the target in real environment. The data is coherently averaged 1024 times to enhance the S/N. The antenna pair are scanned for the range of -200 mm $\leq x \leq 200$ mm where the sampling interval is set to 10 mm. We first measure the direct wave without scattering, and eliminate the direct waveform from the received signals to obtain the scattered waveform.

Envelope+WE can be easily extended to the bi-static system. In the bi-static model, the target boundary is estimated with the envelope of the ellipses which utilize the location of the transmitted and received antenna as the focus. Fig. 4.17 illustrates the envelope of the ellipses for the antenna pair. We also easily extend the scattered waveform estimation to the pair antennas with setting an integral path for the two-path model as shown in Fig.4.17. Fig. 4.18 shows the observed signals with our experiment. The S/N is 48.0 dB. Figs. 4.19 and 4.20 show the estimated images with Envelope and Envelope+WE method, respectively. The number of iterations is 5. As shown in Fig. 4.19, the estimated image does not have sufficient resolution around the edges, and μ of this image is about $2.2 \times 10^{-2}\lambda$, which is defined in Eq. (4.12). In contrast, the image with Envelope+WE method is more accurate than Envelope method, especially around the edges. μ of this
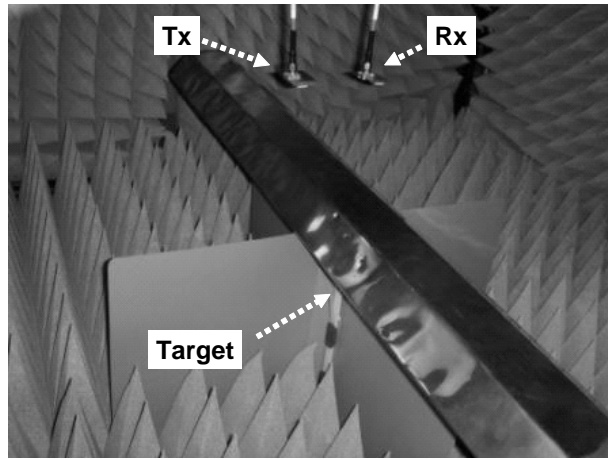
Figure 4.16: Arrangement of the pair antenna and the target in experiments.
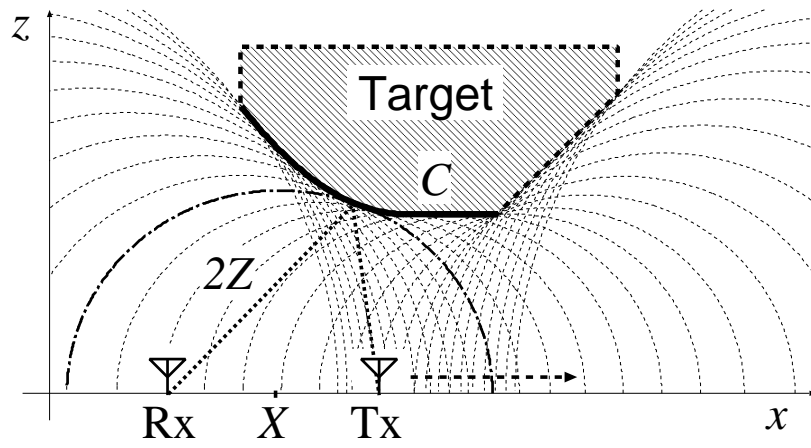
Figure 4.17: Target boundary and an envelope of the ellipses for bi-static model.
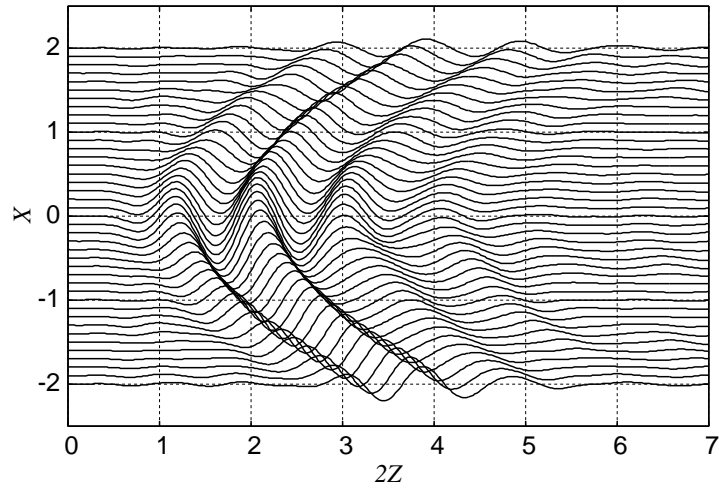
Figure 4.18: Scattered waveforms in experiments.

image is about $1.5 \times 10^{-2}\lambda$. Fig. 4.21 shows the estimated curvatures with each method. This figure shows that Envelope+WE method can accurately estimate the locations of the edges. However, there are two false peaks of the curvature for Envelope+WE, and the image around the edges deteriorates compared with Fig.4.10. These false peaks are caused by the small errors of the quasi wavefront. This is because we cannot completely eliminate the direct wave and the undesirable echoes from other objects. The cables and the plastic poles which support the antennas contribute to the received signal as the multiple scattered wave between the target and those objects. Additionally, these false peaks are also estimated in numerical simulations, where we add the white noise (S/N = 30 dB) as shown in Fig. 4.22. Therefore, data with higher S/N and S/I is needed to enhance the accuracy of this region. Moreover, this method requires 2.0 sec for the calculation for Xeon 3.2 GHz processor, and more rapid imaging method is needed for our assumed applications.
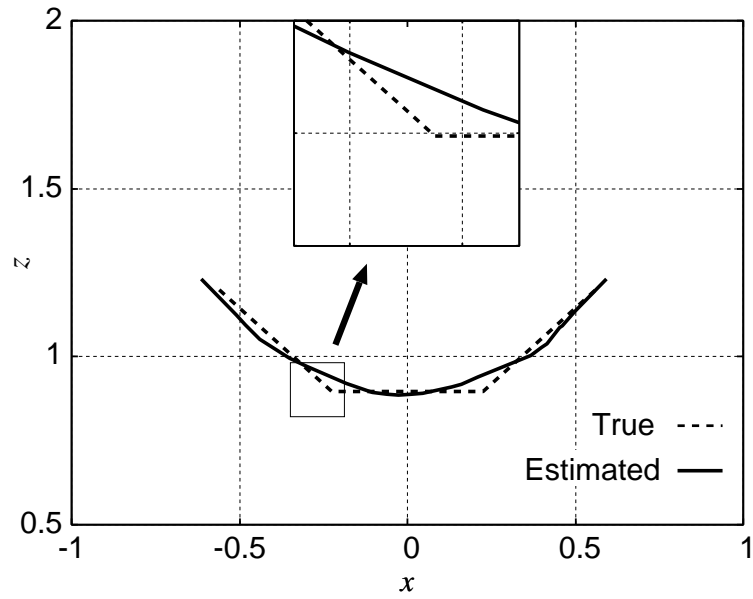
Figure 4.19: Estimated image with Envelope in experiments.
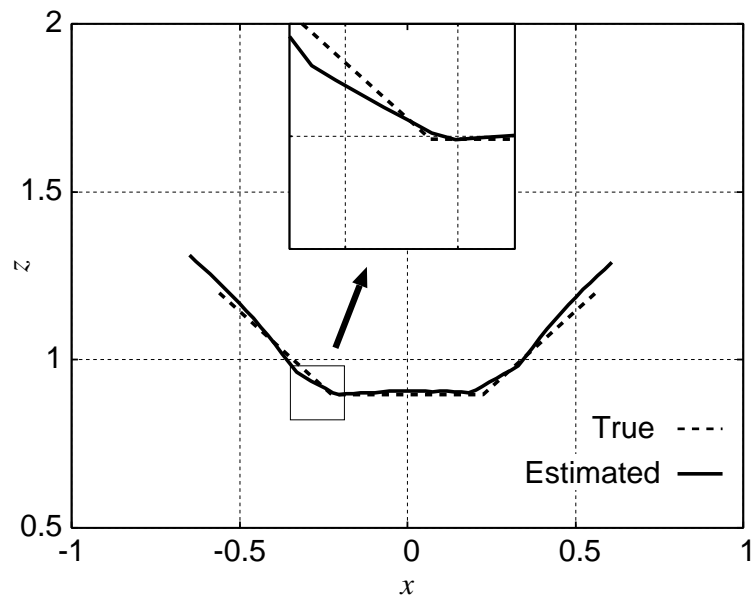
Figure 4.20: Estimated image with Envelope+WE in experiments.
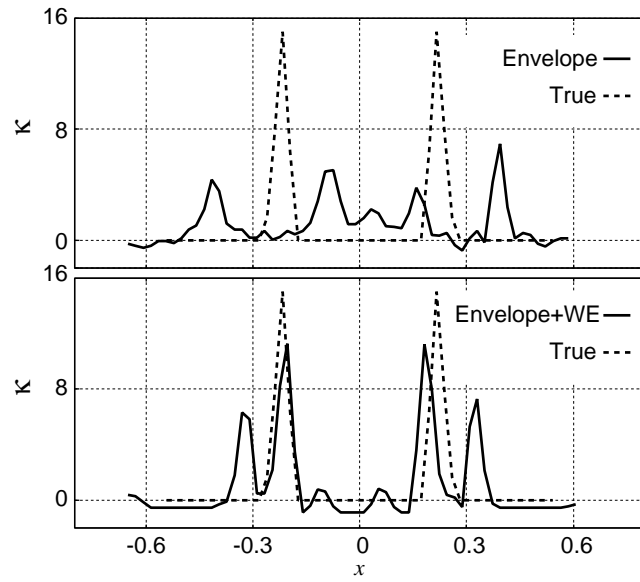
Figure 4.21: Estimated curvatures with Envelope (upper) and Envelope+WE (lower) methods in experiments.
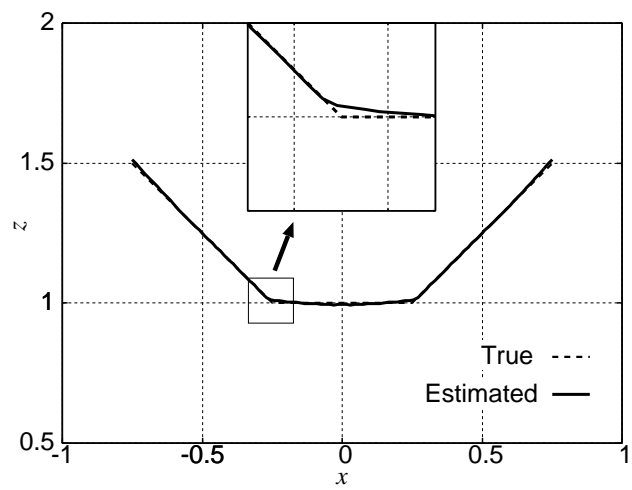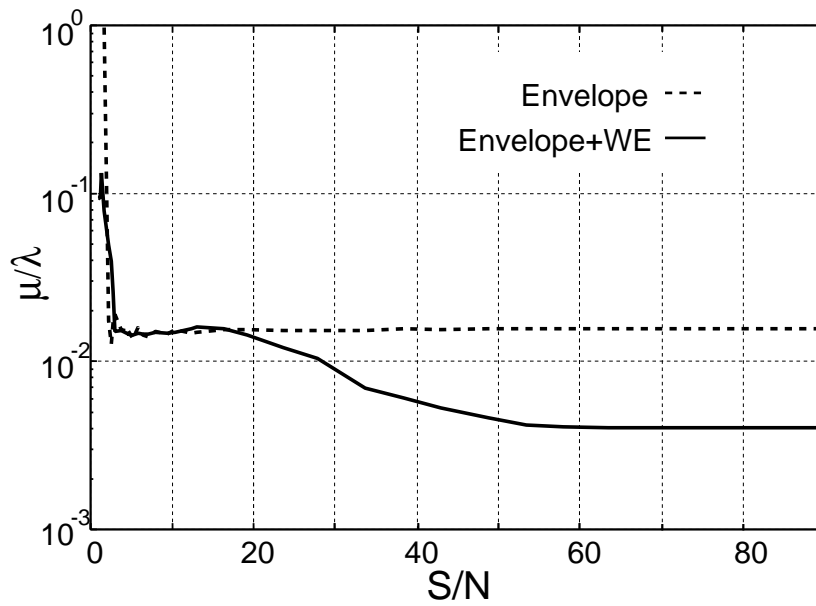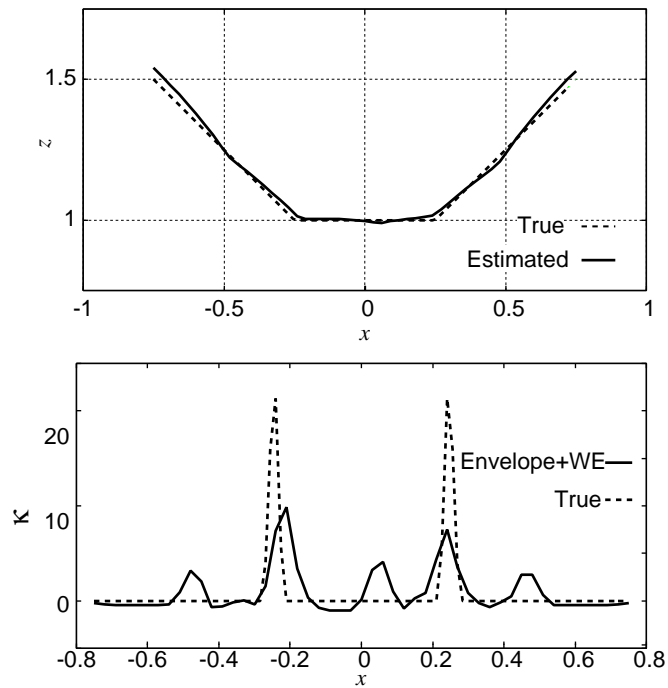

Figure 4.22: Estimated image with Envelope+WE in numerical simulations for S/N=30 dB (upper) and estimated curvatures (lower).
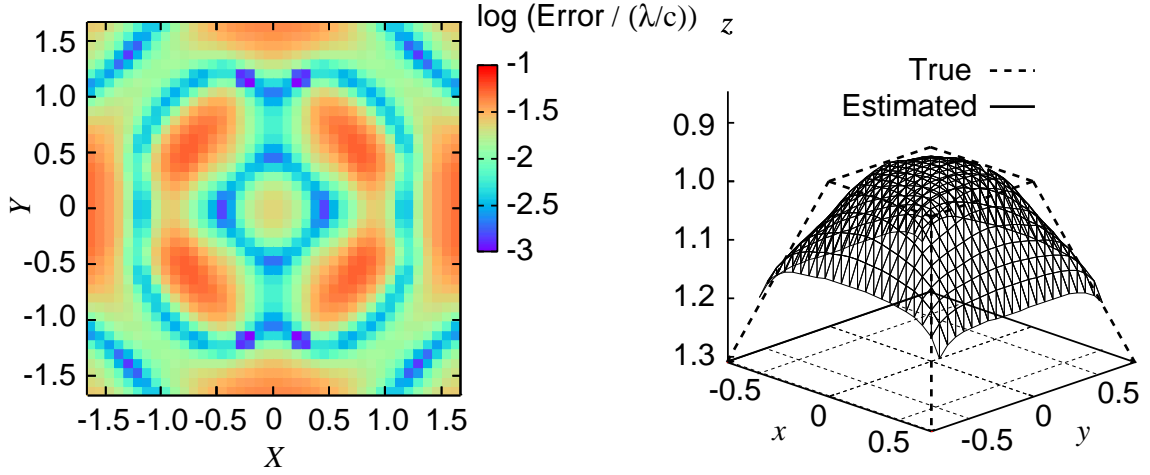
Figure 4.23: Accuracy for quasi wavefront (left) and estimated image (right) with Envelope.

4.3 Accurate Imaging Algorithm with Waveform Estimation for 3-D Problem

4.3.1 Image Distortions for 3-D Problem

We utilize the same model, as described in Sec. 3.3.1. The target has a convex shape boundary. Envelope method utilizes the principle that the target boundary should be expressed as an envelope of spheres whose center $(X, Y, 0)$ and radius Z. The left and right sides of Fig. 4.23 show the accuracy of the extracted quasi wavefront for each antenna location and the estimated image with Envelope in noiseless environment, respectively, where the received signals are calculated with FDTD method. We confirm that the resolution of this method is relatively low around the target edges due to the error of quasi wavefront. The maximum error for the quasi wavefront goes up to $3.0 \times 10^{-2} \lambda/c$. This is because the edge diffraction waveforms are different from the transmitted one due to the same effects in 2-D problem.

4.3.2 Performance Evaluation for Envelope+WE

To resolve this problems, we synthesize the shape and waveform estimations to enhance the resolution around the edges or wedges with the same approach in 2-D problem, which is termed Envelope+WE. In 3-D problem, the waveform estimation with the Green's function integral can be expressed as

$$F(\omega; X, Y) = \mathrm{j}\omega E_0(\omega) \int_S g(2|\boldsymbol{r}|)\mathrm{d}S \tag{4.13}$$
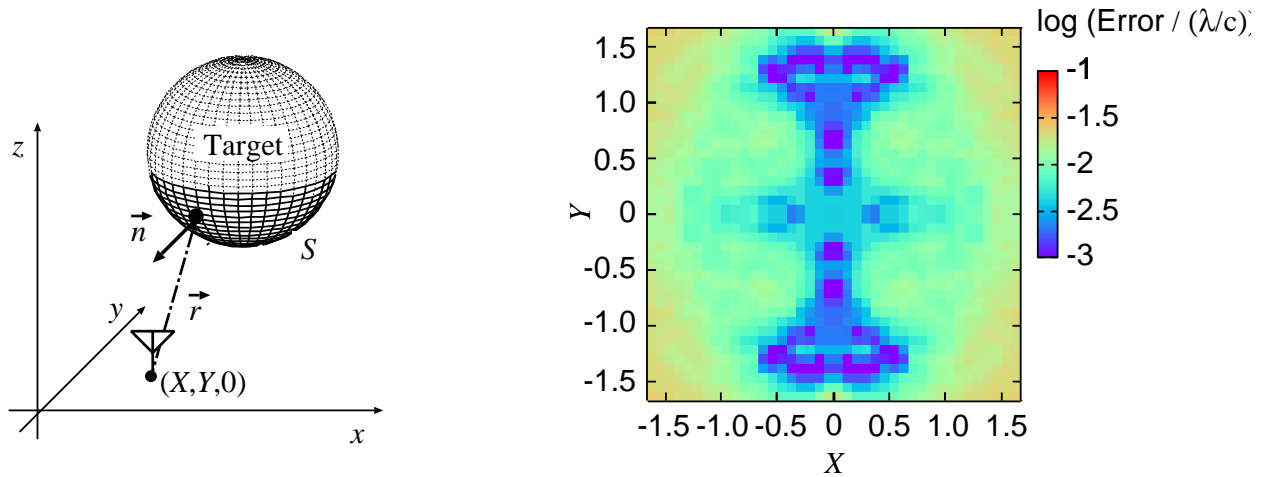
Figure 4.24: Target boundary and antenna location for the waveform estimation (left), and the accuracy for the quasi wavefront, where true target parameter is given in the case of Fig. 4.23 (right).

where r the position vector on the target surface, and S is the target boundary, which dominantly contributes the scattering. $g(r) = \mathrm{e}^{-jkr}/r$ and $E_0(\omega)$ is the transmitted waveform in the frequency domain. The left hand side of Fig. 4.24 shows relationship between the target boundary and antenna location. We show the example for the waveform estimation as follows. The right hand side of Fig. 4.24 shows an accuracy of the quasi wavefront, where we give the true parameter of the target boundary in the case of Fig. 4.23. It can enhance the accuracy for the quasi wavefront, around the edge region. However, at the side of target boundary, the accuracy becomes lower because the influence of shadow region is not negligible in the scattering effects. The left and right hand sides of Fig. 4.25 show the accuracy for the quasi wavefront and the estimated image, where we carry out the shape and waveform estimation recursively with the same principles in 2-D problems, which corresponds to Envelope+WE. The iteration number is 2. We confirm that the resolution and accuracy for the edge region are still insufficient, and the estimated image hardly converges to the true shape, even if we increase the number of the iteration. The errors around the edge region is more than $2.0 \times 10^{-2}\lambda$. Moreover, the calculation time of this method is more than 10 sec, which is not realistic to deal with the practical applications.
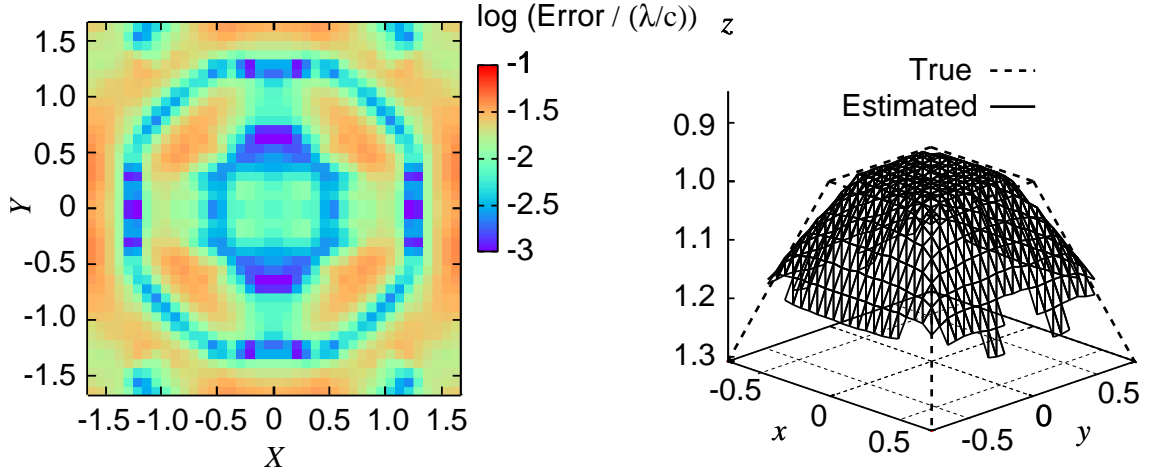
Figure 4.25: Accuracy for quasi wavefront (left) and estimated image (right) with Envelope+WE (Iteration number is 2).

4.4 Fast and Accurate 3-D Imaging Algorithm with Spectrum Offset Correction

4.4.1 Imaging Algorithm with Spectrum Offset Correction

To resolve those problems described in the previous section, we propose a high-speed and accurate 3-D imaging with the spectrum offset correction. This method directly compensates a range error of Z with the center frequencies of the waveforms. We confirm that the matching point between the scattered and transmitted signals cannot express the true time of arrival due to the waveform deformations. Fig. 4.26 shows the matching example between the transmitted and scattered waveforms. This method approximates the range shift ΔZ as

$$\Delta Z = \frac{f_0}{W}(f_{\mathrm{tr}}^{-1} - f_{\mathrm{sc}}^{-1}), \tag{4.14}$$

where f_{sc} and f_{tr} are the center frequencies of the scattered and transmitted waveforms, respectively. $f_0 = \mathrm{c}/\lambda$. W is a normalized constant, which is determined with the fractional bandwidth of the transmitted waveform, and here we set $W = 4$. Each center frequency is calculated as the frequency whose power spectrum in the frequency domain is maximum. The procedures of this method are summarized as follows. We calculate the initial value of Z_{init} by the peak search for the output of the matched filter. By calculating Eq. (4.14), Z is compensated as $Z = Z_{\mathrm{init}} + \Delta Z$ for each antenna location. The target boundary is estimated with an envelope of spheres. We call this method as Envelope+SOC (Spectrum Offset Correction). This method accomplishes rapid and high-

94
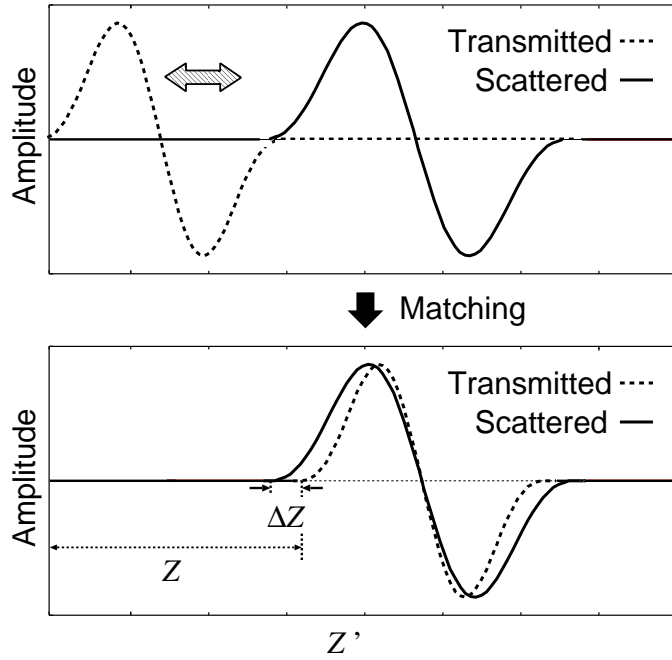
Figure 4.26: A matching example between scattered and transmitted waveforms.

resolution 3-D imaging with direct compensations for the measured errors of the quasi wavefronts.

4.4.2 Application Examples with Numerical Simulations

The left and right hand sides of Fig. 4.27 show the accuracy for the quasi wavefront and the estimated image with Envelope+SOC, respectively. We confirm that our method accomplishes more accurate 3-D imaging including the target edges and wedges. The error around this region is 0.01λ, and the calculation time of this method is 0.2 sec for Xeon 3.2 GHz processor, which can be applicable for the realtime operation. This is because the accuracy of the estimated image depends only on that of the quasi wavefront, which can be directly compensated without reconstructing the scattered waveform completely. In addition, Fig. 4.28 shows the accuracy of quasi wavefront with this method, where we give the white noise to the received signals for S/N = 32 dB. We confirm that it can realize the high-resolution imaging, even in the noisy environment for S/N $\geq$ 30 dB. These results verify that Envelope+SOC method accomplishes the high-performance imaging, in terms of speed, stability, and accuracy, which has never been obtained with the conventional works. The reason of this superiority is that this method specifies to extract the clear boundary with the correctly estimated time delays.

4.4.3 Application Examples with the Experiment

This section describes the performance evaluation with the experimental data, where the same transmitted signal and antennas as described in Sec. 2.3.4 are used. We set the trapezoid target, which is made of stainless steel sheet. Fig. 4.29 illustrates the location of the antenna and the target in the experiment. The transmitted and received antennas are scanned on $z = 0$ plane, for -170mm $\leq x \leq 170$mm and -200mm $\leq y \leq 200$mm, respectively, where each sampling interval is set to 10mm. The separation between the transmitted and received antennas is 48mm in y-direction, which corresponds to the major axis of the elliptic polarimetry. The data are coherently averaged 1024 times. Figs. 4.30 and 4.31 show the estimated image and the accuracy for the quasi wavefront with Envelope, respectively. S/N is 35 dB. As shown in these figures, the accuracy for the target wedge is distorted due to the scattered waveform deformations. ϵ, which is defined in Eq. (2.7), is $3.178 \times 10^{-2}\lambda$. Contrarily, Fig. 4.32 and 4.33 show those with Envelope+SOC. While it verifies that there are some improvement for the accuracy, the estimated image still has errors. ϵ is $1.933 \times 10^{-2}\lambda$. This is because scattered waves are interfered from the direct waves, which cannot be eliminated completely due to the timing jitters. Thus, it causes non-negligible errors for the center frequency estimations because we calculate f_{sc} in the frequency domain.

Frequency estimation in the time domain

To suppress these errors in the frequency estimation, we calculate f_{sc} in the time domain as [134],

$$f_{\mathrm{sc}} = \frac{1}{2\pi} \angle \left(\sum_{i=0}^{N} s_i^* \, s_{i+1} \right), \tag{4.15}$$

where $s_i = s\left(i\Delta t + 2Z_{\mathrm{init}}\lambda/\mathrm{c}\right)$, $s(t)$ is an analytical signal of the scattered wave, Δt is the interval of the time sampling, and N is the total number of the samples. Eq. (4.15) enables us to calculate f_{sc} with eliminating the interferences from the multiple scattered or the direct waves because these components can be windowed in the time domain. Here, $N\Delta t$ is set to $2.0\lambda/\mathrm{c}$, which is empirically determined as the optimum value in terms of the accurate and robust frequency estimation. Fig. 4.34 shows the examples of the transmitted and scattered waves in the experiment, and the time region for the frequency estimations.

Fig. 4.35 and 4.36 show the estimated image and the accuracy for the quasi wavefront with Envelope+SOC, respectively, where the center frequency is calculated in the time domain. These figures verify that the estimated image can be more accurately reconstructed, around the upper surface of the target. ϵ is $1.631 \times 10^{-2}\lambda$. This is because the center frequency can be determined in the time domain, where the interferences of the direct wave are relatively lower. However, there are some distortions in the estimated image, compared to the results in the numerical simulations. This is because the fractional

bandwidth of the experimental pulse is lower than that of the mono-cycle pulse. Thus, the scattered wave is severely interfered with the remains of direct wave, which cannot be completely eliminated.

4.5   Conclusion

We proposed a high-resolution imaging algorithm as Envelope+WE by simultaneously estimating the shape and scattered waveform in 2-D problem. We clarify that Envelope+WE achieves a high-resolution imaging and correctly identifies the characteristic of the target shape. The accuracy of the estimated image is better than 0.01λ with a numerical simulation for S/N$\geq$ 30 dB. We have investigated the performance of Envelope+WE with the experiments, and clarified the effectiveness in detecting edges even for the realistic environment. However, this method requires 2.0 sec for the calculation time, which is not sufficient for the real time operations. Moreover, we extended this idea to 3-D problems, and demonstrated the performance with numerical simulations. We confirmed that the estimated image hardly converged to the true target shape, and it required an intensive computation.

To resolve this problem, we proposed the directly compensation algorithm for the measured error of the quasi wavefront with the spectrum offset correction as Envelope+SOC. It can realize rapid and high-resolution 3-D imaging for general convex targets. Numerical simulations verify that the accuracy for imaging is within 0.01λ and the calculation time 0.2 sec with Xeon 3.2 GHz processor for S/N $\geq$ 30 dB. Furthermore, we investigate the experimental study of Envelope+SOC, and it is confirmed that this method can realize more accurate imaging in real environment. We consider that this method can accomplish the high-performance imaging, and remarkably improves the quality of the proximity radar imaging, which is never obtained with the conventional works.
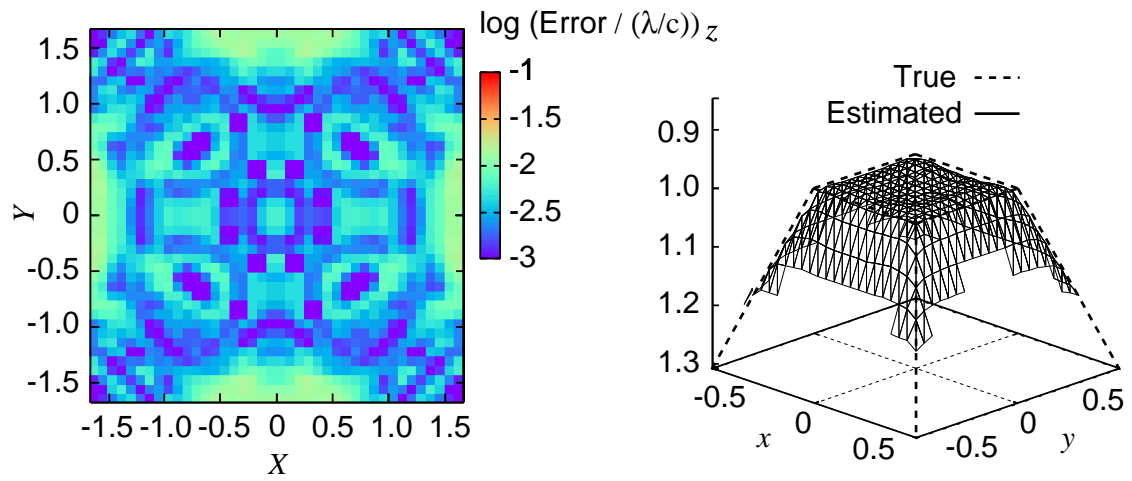
Figure 4.27: Accuracy for quasi wavefront (left) and estimated image (right) with Envelope + SOC .
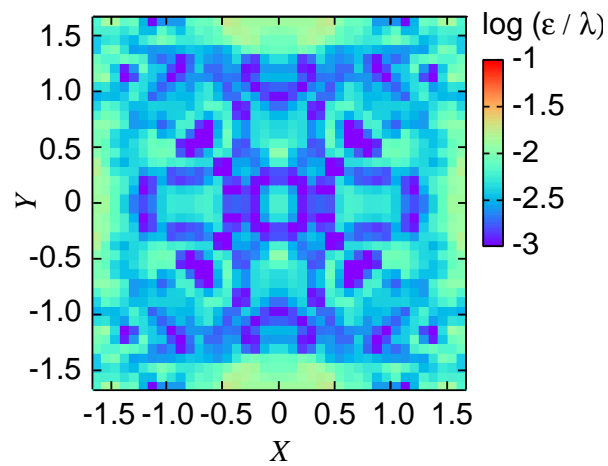
Figure 4.28: Accuracy for the quasi wavefront with Envelope+SOC where S/N = 32 dB.
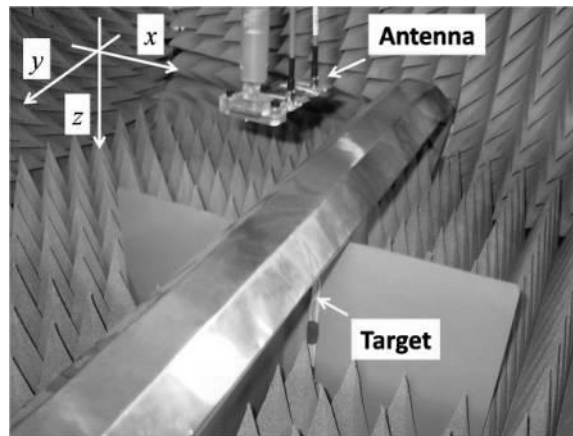
Figure 4.29: Arrangement of the experiment.
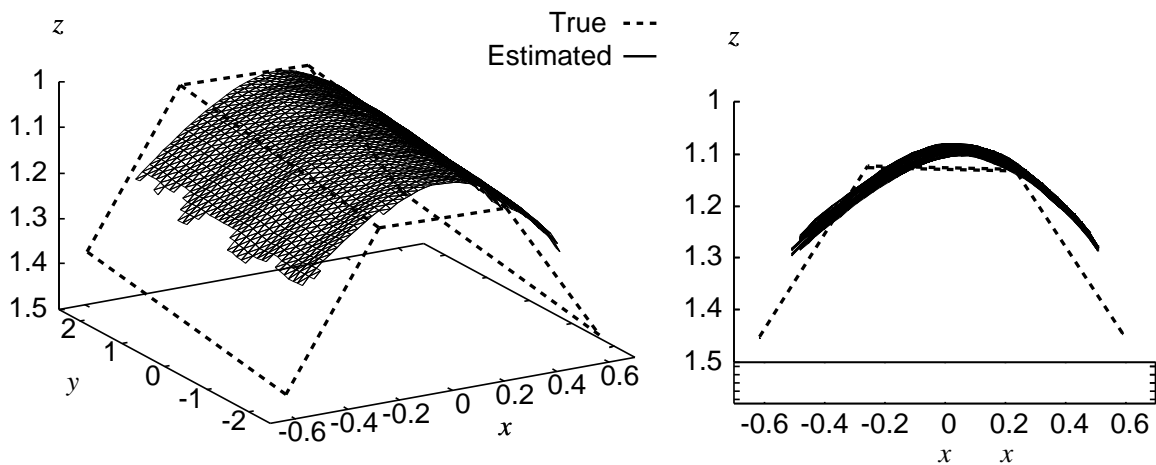
Figure 4.30: Estimated image with Envelope in the experiment.
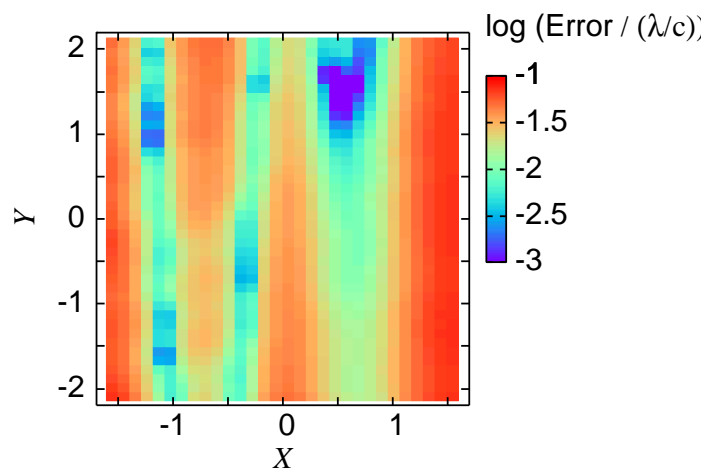
Figure 4.31: Accuracy for the quasi wavefront with Envelope in the experiment.

99
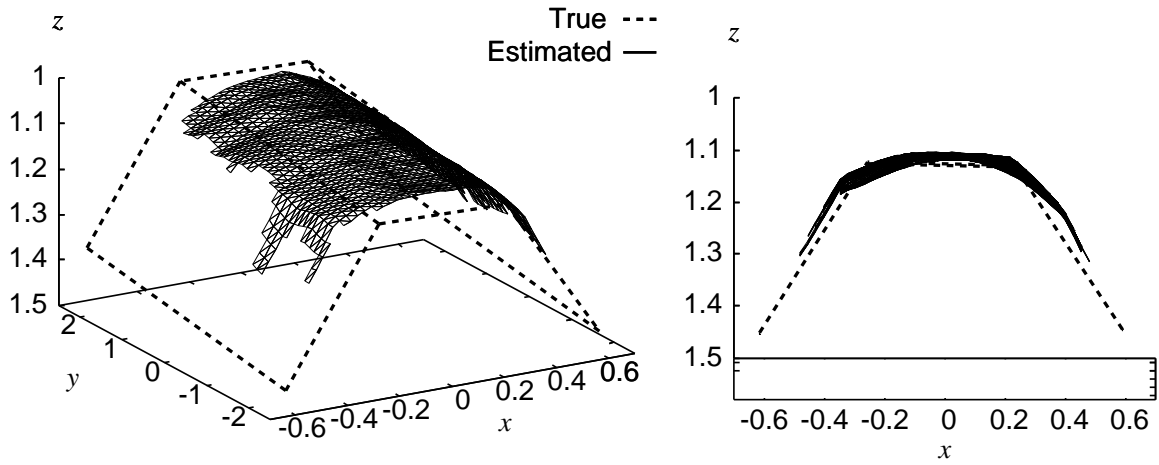
Figure 4.32: Estimated image with Envelope+SOC in the experiment, where the center frequency is calculated in the frequency domain.
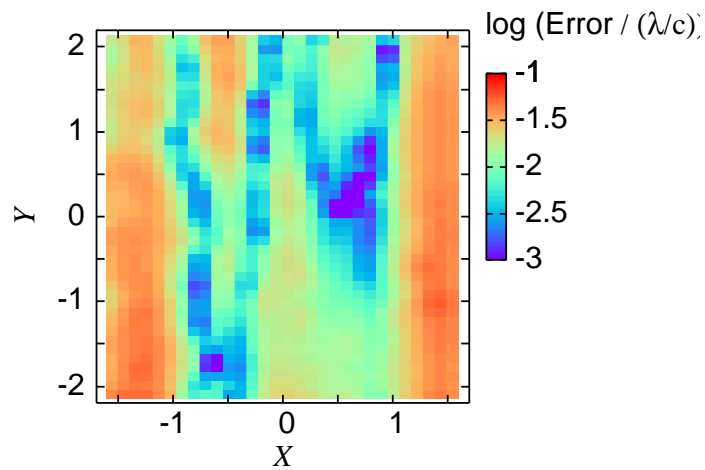
Figure 4.33: Accuracy for the quasi wavefront with Envelope+SOC in the experiment, where the center frequency is calculated in the frequency domain.
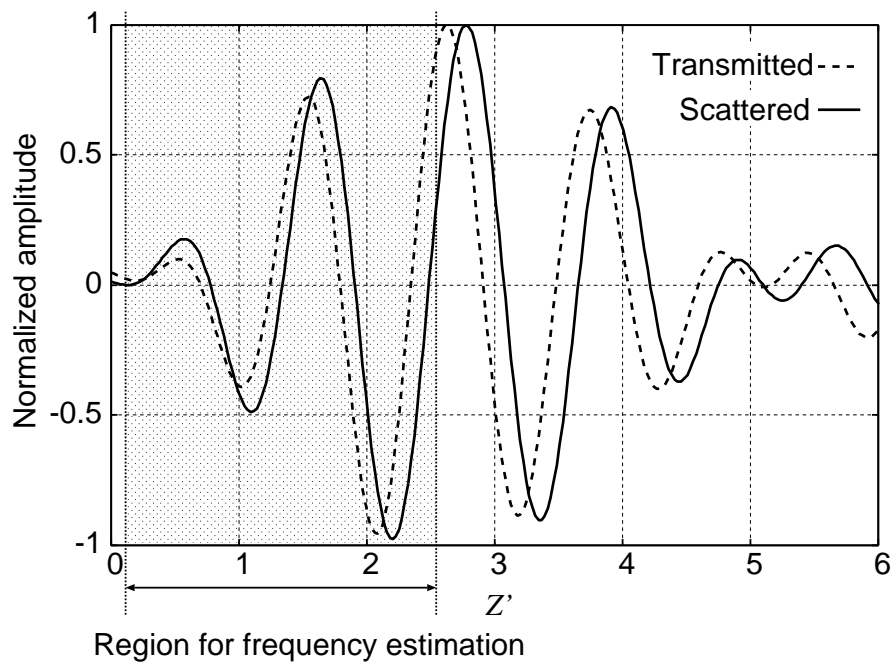
Figure 4.34: An example of the transmitted and scattered waveform in the experiment.
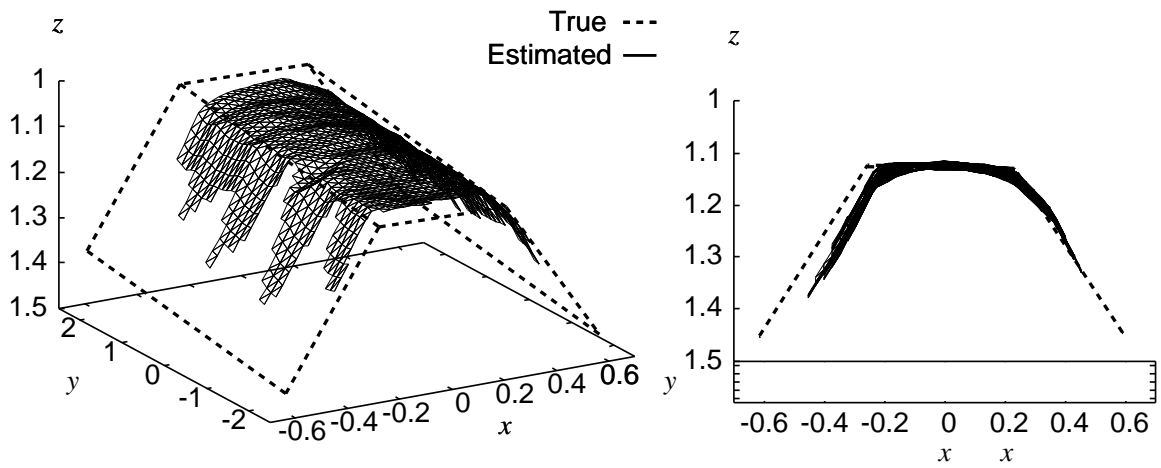
Figure 4.35: Estimated image with Envelope+SOC in the experiment, where the center frequency is calculated in the time domain.
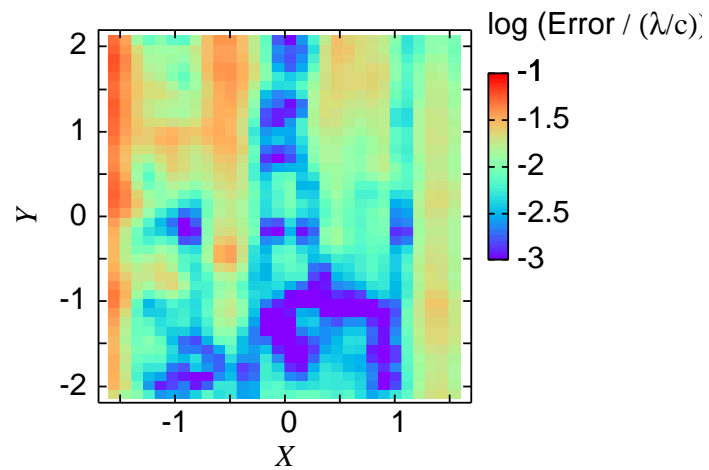
Figure 4.36: Accuracy for the quasi wavefront with Envelope+SOC in the experiment, where the center frequency is calculated in the time domain.

Chapter 5

Concluding Remarks

This thesis provides the high-performance 3-D imaging algorithms for UWB pulse radars, which are suitable for the proximity imaging. Envelope+SOC method can realize the high-performance imaging, in terms of rapidness, robustness, flexibility, accuracy and resolution. These performances are required for the non-destructive investigation of the precision devices, such as reflector antennas and automobiles. Moreover, these studies are promising as the near field imaging for rescue or household robots, and will promote the development of these applications.

Chap 2 describes the high-resolution and fast imaging algorithm with linear array antennas. We extend the reversible transform BST for the bi-static radar systems. It can realize the high-resolution imaging without increasing the number of the array antennas. We showed the effectiveness of the extended system with the bi-static radar in both numerical simulations and experiments. This system is quite realistic for the actual imaging system with robots because a linear array antenna can be equipped with the robots for the vertical direction. Thus, by moving around the target, it can realize the 2-D scanning of antenna, and enables robots to detect or avoid objects more effectively.

Chap 3 represents the robust and fast 3-D imaging algorithm with the envelope of spheres as Envelope. It can realize robust and rapid imaging for an arbitrary target shape without derivative operations. In addition, we can robustly compensate the phase rotations caused by passing through the caustic points in the case of the concave boundary. This result is quite profitable for the accurate imaging, which aims at the precision devices, such as reflector antenna with a concave shape. However, the accuracy for the edge regions distorts due to the waveform deformations.

Thus, in Chap 4, we introduce the accurate imaging algorithm by compensating these waveform deformations. In 2-D problems, we synthesize the shape and waveform estimations with a recursive manner as Envelope+WE. This method can deal with the general convex targets, and we confirmed that it can realize the high-resolution imaging including the target edges in numerical simulations and experiments. However, in 3-D problems, the calculation time for the waveform estimation cannot be negligible, and we proposed

	Rapidness	Robustness	Accuracy	Flexibility
SEABED		×	△	◯
Envelope	◯	◯	△	◯
Envelope + WE	△	△	◯	◯
Envelope + SOC	◯	◯		◯

Table 5.1: Performance comparison for each algorithm

fast and high-speed imaging with the spectrum shift of the scattered waveform as Envelope+SOC. This method can directly determine the measured shift due to waveform deformations with the center frequencies. In numerical simulation, it can determine the target surface on the order of 0.01λ for 0.2 sec with Xeon 3.2 GHz processor, which can never be obtained with the conventional radar systems. Moreover, we investigate the performance evaluations with the experimental data. These results show that Envelope+SOC achieves an accurate imaging in the real environment to the order of $1/100 \lambda$.

Table.5.1 shows the performance comparison for each imaging algorithm. Although SEABED has a great advantage for rapidness and flexibility, it is difficult to deal with the practical application due to the instability. While Envelope resolves this instability, the accuracy distorts around the target edges. Envelope+WE achieves the accurate 2-D imaging; however the rapidness and robustness are not sufficient for the assumed applications. Contrarily, Envelope+SOC accomplishes a high quality in each performance, which is considered to become a breakthrough of the radar imaging, and it is most promising candidate for the proximity imaging. Moreover, it can be applied to the imaging systems, which deal with general waves.

However, it is our important future task to develop this algorithm for the various kinds of target models, which have more complex shapes with not clear boundary, such as human body. The synthesis between the radar and other imaging systems has a incalculable possibility to overcome these problems, and accomplishes the high-grade imaging for free space.

Appendix A

Bistatic BST

A.1   Derivation of Eqs. (2.3) and (2.4).

First, let us derive Eq. (2.4). As shown in Fig. 2.3, the target boundary (x, z) should be on an ellipse as

$$\frac{(x - X)^2}{Z^2} + \frac{z^2}{Z^2 - d^2} = 1, \tag{A.1}$$

where $Z > d > 0$ holds. We define $G(x, z; X, Z, d)$ as

$$G(x, z; X, Z, d) = (Z^2 - d^2)(x - X)^2 + Z^2 z^2 - Z^2(Z^2 - d^2). \tag{A.2}$$

Thus, Eq. (A.1) is expressed as

$$G(x, z; X, Z, d) = 0. \tag{A.3}$$

Additionally, the target boundary (x, z) should exist on an envelope of ellipses in Eq. (A.1) with parameter X, and

$$\partial G(x, z; X, Z, d)/\partial X = 0, \tag{A.4}$$

holds. Eliminating z in Eqs. (A.3) and (A.4), we obtain

$$d^2 Z_X (x - X)^2 - Z(Z^2 - d^2)(x - X) - Z^4 Z_X = 0, \tag{A.5}$$

where $Z_X = \partial Z/\partial X$ is defined. If $d \neq 0$ and $Z_X \neq 0$ holds, x is expressed as,

$$x = X - \frac{2Z^3 Z_X}{Z^2 - d^2 \pm \sqrt{(Z^2 - d^2)^2 + 4d^2 Z^2 Z_X^2}}. \tag{A.6}$$

We define the two solutions as x_+ and x_-, respectively, where the subscript of the solution corresponds to the mark of the square root. By taking $d \to 0$ for the absolute value of x_+
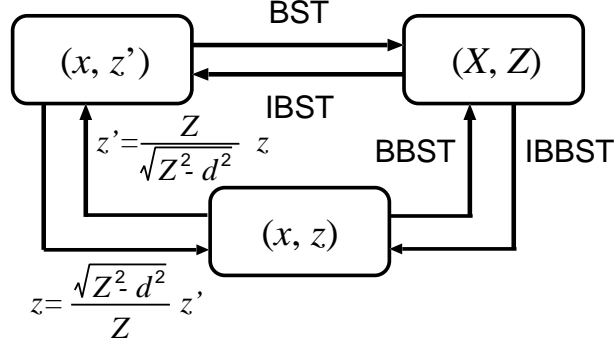
Figure A.1: Relationship between (x, z), (x, z') and (X, Z).

and x_-, we obtain

$$\lim_{d \to 0} |x_+| = |X - ZZ_X|, \qquad (A.7)$$

$$\lim_{d \to 0} |x_-| = \infty. \qquad (A.8)$$

With the condition that x converge to the finite for $d \to 0$, x is given as

$$x = X - \frac{2Z^3 Z_X}{Z^2 - d^2 + \sqrt{(Z^2 - d^2)^2 + 4d^2 Z^2 Z_X^2}}, \quad (d \neq 0, Z_X \neq 0). \qquad (A.9)$$

Eq. (A.9) corresponds to the solutions, where we set $Z_X = 0$ and $d = 0$ in Eq. (A.5), respectively. Solving Eq. (A.1) for z, Eq. (2.4) is derived.

Eq. (2.3) can be derived in a similar manner. $g(X, Z; x, z, d)$ is defined as

$$g(X, Z; x, z, d) = (Z^2 - d^2)(x - X)^2 + Z^2 z^2 - Z^2(Z^2 - d^2). \qquad (A.10)$$

The point (X, Z) should be on an envelope of the curves in Eq. (A.10) with parameter x. Thus, (X, Z) should satisfy

$$g(X, Z; x, z, d) = 0, \qquad (A.11)$$

$$\partial g(X, Z; x, z, d)/\partial x = 0. \qquad (A.12)$$

Solving these two equations about X and Z, Eq. (2.3) is derived.

We prove a reversibility between Eqs. (2.3) and (2.4) as follows. We define z' as an arbitrary single-valued function of x, which is differentiable. (X, Z) is defined with BST as $X = x + z' z'_x$, $Z = z'\sqrt{1 + z'^2_x}$. The reversibility between (x, z') and (X, Z) is proved in [127]. Additionally,

$$G(x, z'; X, Z, 0) = g(X, Z, x, z', 0) = 0, \qquad (A.13)$$

$$\partial G(x, z'; X, Z, 0)/\partial X = 0, \qquad (A.14)$$

$$\partial g(X, Z; x, z', 0)/\partial x = 0, \qquad (A.15)$$

106

should hold. Here, we define z as $z = \frac{\sqrt{Z^2-d^2}}{Z}z'$, where d is constant and $Z > d > 0$ holds. Substituting z to Eqs. (A.13), (A.14) and (A.15), we obtain

$$\frac{(x-X)^2}{Z^2} + \frac{z^2}{Z^2-d^2} = 1, \tag{A.16}$$

$$d^2 Z_X(x-X)^2 - Z(Z^2-d^2)(x-X) - Z^4 Z_X = 0 \tag{A.17}$$

$$(Z^2-d^2)(x-X) + Z^2 z z_x = 0. \tag{A.18}$$

These three equations correspond to Eqs. (A.3), (A.4) and (A.12), respectively. Accordingly, (X, Z) and (x, z) should satisfy Eqs. (2.3) and (2.4). Additionally, $z' = \frac{Z}{\sqrt{Z^2-d^2}}z$ holds, and (x, z) and (x, z') satisfy a reversibility. Thus, the reversibility between (x, z) and (X, Z) should hold. Fig. A.1 shows the relationship between (x, z'), (X, Z), and (x, z).

A.2 Derivation of Eqs. (2.5) and (2.6).

Let us derive Eq. (2.6) as follows. The point on the target boundary (x, y, z) should be on the ellipsoid as,

$$\frac{(x-X)^2}{Z^2} + \frac{(y-Y)}{Z^2-d^2} + \frac{z^2}{Z^2-d^2} = 1, \tag{A.19}$$

where $Z > d > 0$ holds. Here we define the function $G(x, y, z; X, Y, Z, d)$ as

$$
\begin{aligned}
G(x, y, z; X, Y, Z, d) &= (Z^2-d^2)(x-X)^2 + Z^2(y-Y)^2 \\
&\quad + Z^2 z^2 - Z^2(Z^2-d^2).
\end{aligned} \tag{A.20}
$$

Eq. (A.29) is expressed as

$$G(x, y, z; X, Y, Z, d) = 0. \tag{A.21}$$

The target boundary should be on an envelope of ellipsoids with the parameters X and Y. Thus,

$$\partial G(x, y, z; X, Y, Z, d)/\partial X = 0, \tag{A.22}$$

$$\partial G(z, y, z; X, Y, Z, d)/\partial Y = 0, \tag{A.23}$$

hold. Eliminating y and z in Eqs. (A.21) and (A.23), the solution for x is expressed as

$$x = X - \frac{2Z^3 Z_X}{Z^2-d^2 + \sqrt{(Z^2-d^2)^2 + 4d^2 Z^2 Z_X^2}}. \tag{A.24}$$

Here we specify the subscript of the solution with the similar approach in A.1. Additionally, eliminating z in Eqs. (A.21) and (A.23), y is expressed as

$$y = Y + Z_Y \left\{ d^2(x-X)^2 - Z^4 \right\}/Z^3 \tag{A.25}$$

107

With Eq. (A.5), z is expressed as

$$z = \sqrt{Z^2 - d^2 - (y - Y)^2 - \frac{(Z^2 - d^2)(x - X)^2}{Z^2}}. \tag{A.26}$$

Thus, Eq. (2.6) is derived. Eq. (2.5) can be derived, where we define $g(X, Y, Z; x, y, z, d)$ as

$$
\begin{aligned}
g(X, Y, Z; x, y, z, d) &= (Z^2 - d^2)(x - X)^2 + Z^2(y - Y)^2 \\
&\quad + Z^2 z^2 - Z^2(Z^2 - d^2).
\end{aligned} \tag{A.27}
$$

(X, Y, Z) should satisfy the next conditions,

$$
\begin{aligned}
g(X, Y, Z; x, y, z, d) &= 0, & \text{(A.28)} \\
\partial g(X, Y, Z; x, y, z, d)/\partial x &= 0, & \text{(A.29)} \\
\partial g(X, Y, Z; x, y, z, d)/\partial y &= 0. & \text{(A.30)}
\end{aligned}
$$

Additionally, the reversibility between (x, y, z) and (X, Y, Z) is proved with the similar approach in A.1.

Appendix B

Envelope of Circles and Target Boundary

B.1 Proof of Eq. (3.4)

First, let us prove that if $\partial x/\partial X > 0$ holds at $(X, Z) \in \partial D$, $\partial S_{(X,Z)}$ circumscribes ∂T, where we define $\partial S_{(X,Z)}$ as the boundary of $S_{(X,Z)}$. With $(x, z) \in \partial T$, the curvature κ on ∂T is expressed as

$$\kappa = \frac{\partial^2 z/\partial x^2}{(1 + (\partial z/\partial x)^2)^{3/2}} \tag{B.1}$$

$$= \frac{Z_{XX}}{1 - ZZ_{XX} - Z_X^2}. \tag{B.2}$$

where we define $Z_X = \partial Z/\partial X$, $Z_{XX} = \partial^2 Z/\partial X^2$, and utilize $\partial z/\partial x = Z_X/\sqrt{1 - Z_X^2}$, and $\partial^2 z/\partial x^2 = \frac{Z_{XX}}{(1 - Z_X^2)^{3/2}(1 - ZZ_{XX} - Z_X^2)}$, which are derived in [128]. Here, the condition that $\partial S_{(X,Z)}$ circumscribes ∂T is that $\kappa > -1/Z$ holds because a curvature of $\partial S_{(X,Z)}$ should be $-1/Z$ for $z \geq 0$. If $\partial x/\partial X > 0$ holds, this condition is expressed as $1 - (\partial Z/\partial X)^2 > 0$, which is satisfied because z is a real number in the IBST. Therefore, the previous proposition is proved. Similarly, we can prove that if $\partial x/\partial X < 0$ holds at $(X, Z) \in \partial D$, $\partial S_{(X,Z)}$ inscribes ∂T. By utilizing these facts, the next proposition holds,

Proposition 2 *If $\partial x/\partial X > 0$ holds at ∂D and $(x, z) \in \partial T$, $x \in \gamma$ holds, $(x - X)^2 + z^2 \geq Z^2$ is satisfied for all $(X, Z) \in \partial D$, and (X, Z) exists as only one, where an equal sign holds.*

We show the proof of this proposition as follows. We define $(x_{\mathrm{p}}, z_{\mathrm{p}}) \in \partial T, x_{\mathrm{p}} \in \gamma$ as the circumscription point of $\partial S_{(X_{\mathrm{p}}, Z_{\mathrm{p}})}$ where $(X_{\mathrm{p}}, Z_{\mathrm{p}}) \in \partial D$. We assume that $\partial S_{(X_{\mathrm{p}}, Z_{\mathrm{p}})}$ exists, which intersects ∂T except for $(x_{\mathrm{p}}, z_{\mathrm{p}})$ as shown in Fig. B.1. We define this intersection point as $Q = (x_{\mathrm{q}}, z_{\mathrm{q}})$, where $x_{\mathrm{q}} > x_{\mathrm{p}}$, $x_{\mathrm{q}} \in \gamma$ holds, and other intersection points do
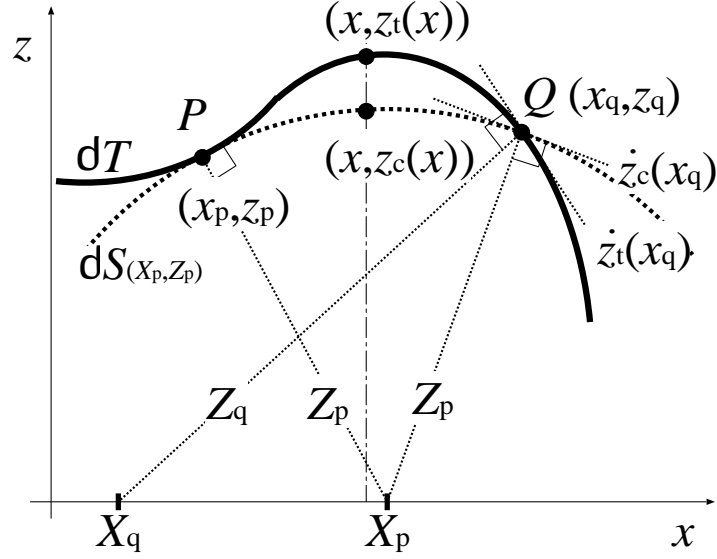
Figure B.1: Arrangement of P, Q, $S_{(X_\mathrm{p}, Z_\mathrm{p})}$ and ∂T for the proof of Proposition 2..

not exist for the region $x_\mathrm{p} < x < x_\mathrm{q}$. We also define $(X_\mathrm{q}, Z_\mathrm{q})$, which is transformed from $(x_\mathrm{q}, z_\mathrm{q})$ with BST. Here $(X_\mathrm{q}, Z_\mathrm{q}) \in \partial D$ holds because $(x_\mathrm{q}, z_\mathrm{q}) \in \partial T$. We define the points as $(x, z_\mathrm{t}(x)) \in \partial T$ and $(x, z_\mathrm{c}(x)) \in \partial S_{(X_\mathrm{p}, Z_\mathrm{p})}$ for the region $x_\mathrm{p} \leq x \leq x_\mathrm{q}$. In this region, $z_\mathrm{t}(x) \geq z_\mathrm{c}(x)$ holds because $\partial S_{(X_\mathrm{p}, Z_\mathrm{p})}$ circumscribes ∂T at P. We also define the inclination of ∂T and $\partial S_{(X_\mathrm{p}, Z_\mathrm{p})}$ at Q as $\dot{z}_\mathrm{t}(x_\mathrm{q})$ and $\dot{z}_\mathrm{c}(x_\mathrm{q})$, respectively. Here $\dot{z}_\mathrm{t}(x_\mathrm{q}) \leq \dot{z}_\mathrm{c}(x_\mathrm{q})$ holds because $z_\mathrm{t}(x) \geq z_\mathrm{c}(x)$ holds for $x_\mathrm{p} \leq x \leq x_\mathrm{q}$. Contrarily, $X_\mathrm{q} > X_\mathrm{p}$ holds because $\partial x / \partial X > 0$ and $x_\mathrm{q} > x_\mathrm{p}$ holds. Therefore, $\dot{z}_\mathrm{t}(x_\mathrm{q}) > \dot{z}_\mathrm{c}(x_\mathrm{q})$ satisfies because $X_\mathrm{q} = x_\mathrm{q} + z_\mathrm{q} \dot{z}_\mathrm{t}(x_\mathrm{q})$ and $X_\mathrm{p} = x_\mathrm{q} + z_\mathrm{q} \dot{z}_\mathrm{c}(x_\mathrm{q})$ hold. These facts contradict each other, and $\partial S_{(X_\mathrm{p}, Z_\mathrm{p})}$ circumscribes ∂T at only one point at P. It is also proved if $x_\mathrm{p} > x_\mathrm{q}$ holds. Therefore, $(x - X_\mathrm{p})^2 + z^2 \geq Z_\mathrm{p}^2$ holds for $(x, z) \in \partial T$. Similarly, this is satisfied for all $(X, Z) \in \partial D$. Thus, the proposition 2 is proved. Similarly, we prove that if $\partial x / \partial X < 0$ holds at ∂D and $(x, z) \in \partial T$, $x \in \gamma$ holds, $(x - X)^2 + z^2 \leq Z^2$ satisfies for all $(X, Z) \in \partial D$, and (X, Z) exists as only one, where an equal sign holds.

Here we prove $\partial T = \partial S_+$ as follows.

(a) Proof of $\partial S_+ \subset \partial T$. We assume that the point $P = (x_\mathrm{p}, z_\mathrm{p})$, $(x_\mathrm{p} \in \gamma)$ exists, where $P \in \partial S_+$, $P \notin \partial T$. We define the point $Q = (x_\mathrm{p}, z_\mathrm{q}) \in \partial T$ as shown in Fig. B.2. Here, $(X_\mathrm{p}, Z_\mathrm{p}) \in \partial D$ exists, where $(x_\mathrm{p} - X_\mathrm{p})^2 + z_\mathrm{p}^2 = Z_\mathrm{p}^2$ holds. On the other hand, $(x_\mathrm{p} - X_\mathrm{p})^2 + z_\mathrm{q}^2 \geq Z_\mathrm{p}^2$ holds with Prop. 2. Therefore $z_\mathrm{q} \geq z_\mathrm{p}$ holds because $z_\mathrm{q}, z_\mathrm{p} > 0$. Moreover, $z_\mathrm{q} > z_\mathrm{p}$ because we assume $P \notin \partial T$. Here we define $(X_\mathrm{q}, Z_\mathrm{q}) \in \partial D$ which is transformed from $(x_\mathrm{p}, z_\mathrm{q})$ with BST. Here $(X_\mathrm{q} - x_\mathrm{p})^2 + z_\mathrm{p}^2 < Z_\mathrm{q}^2$ holds because of $(X_\mathrm{q} - x_\mathrm{p})^2 + z_\mathrm{q}^2 = Z_\mathrm{q}^2$ and $z_\mathrm{q} > z_\mathrm{p}$. Therefore $P \in S_{(X_\mathrm{q}, Z_\mathrm{q})}$ holds. $P \in S_+$ holds because of $S_{(X_\mathrm{q}, Z_\mathrm{q})} \subset S_+$. However $\partial S_+ \cap S_+ = \phi$ holds, where ϕ is null set, because S_+ is open

110
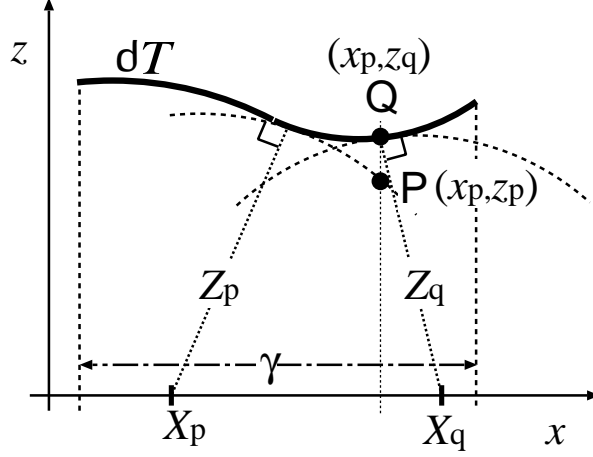
Figure B.2: Arrangement of P, Q and ∂T for the proof of $\partial S_+ \subset \partial T$.

set. Accordingly, $P \notin \partial S_+$ should not hold. Therefore $\partial S_+ \subset \partial T$ is proved.

(b) Proof of $\partial T \subset \partial S_+$, $(x \in \gamma)$.

We assume that $P = (x_p, z_p)$ will exist where $P \in \partial T$, $P \notin \partial S_+$ holds. Here it is obvious with the definition of ∂S_+ that the sufficient condition of $(x, z) \in \partial S_+$ is that for all $(X, Z) \in \partial D$, $(x - X)^2 + z^2 \geq Z^2$ holds and $(X, Z) \in \partial D$ exists at least one point where an equal sign holds. On the contrary, P satisfies the sufficient condition of $(x, z) \in \partial S_+$ with Prop. 2 because $P \in \partial T$ and $\partial x / \partial X > 0$ holds. Accordingly, the previous assumption is not true, and $\partial T \subset \partial S_+$ is proved.

With the facts (a),(b), $\partial T = \partial S_+$ is proved, where $\partial x / \partial X > 0$ holds. Similarly, we can prove that $\partial T = \partial S_\times$ where $\partial x / \partial X < 0$ holds.

B.2   Proof of Proposition 1.

(i). Proof of the necessary condition of Proposition 1.

Here $\partial T = \partial S_\times$ holds because $\partial x / \partial X < 0$. We define $(X_q, Z_q) \in \partial D$, where $X_q \neq X_{\max}, X_{\min}$ holds. We define the point $Q = (x_q, z_q) \in \partial T$, which is transformed from (X_p, Z_p) with IBST as shown in Fig. B.3. Here we also define $(x_{\min}, z_{\min}) \in \partial T$ which is transformed from $(X_{\min}, Z_{\min})$. Here, for all $(X, Z) \in \partial D$, $(X - x)^2 + z^2 \leq Z^2$ holds at $(x, z) \in \partial T$ because $\partial x / \partial X < 0$ holds. Therefore, $(X_{\min} - x_q)^2 + z_q^2 < Z_{\min}^2$ and $(X_q - x_{\min})^2 + z_{\min}^2 < Z_q^2$ hold because $x_q \neq x_{\min}$ holds for $X_q \neq X_{\min}$. We define the points on $\partial S_{(X_q, Z_q)}$ and $\partial S_{\min}$ as $(x, z_Q(x))$ and $(x, z_{\mathrm{MIN}}(x))$, respectively. Here, $z_Q(x_q)^2 < Z_{\min}^2 - (x_q - X_{\min})^2 = z_{\mathrm{MIN}}(x_q)^2$ holds. Also, $z_{\mathrm{MIN}}(x_{\min})^2 < Z_q^2 - (x_{\min} - X_q)^2 = z_Q(x_{\min})^2$ holds. Therefore, $z_Q(x_q) < z_{\mathrm{MIN}}(x_q)$ and $z_Q(x_{\min}) > z_{\mathrm{MIN}}(x_{\min})$ hold because we assume $z \geq 0$. Accordingly, $\partial S_{(X_q, Z_q)}$ and $\partial S_{\min}$ intersect at the region $x_q < x < x_{\min}$ because

111
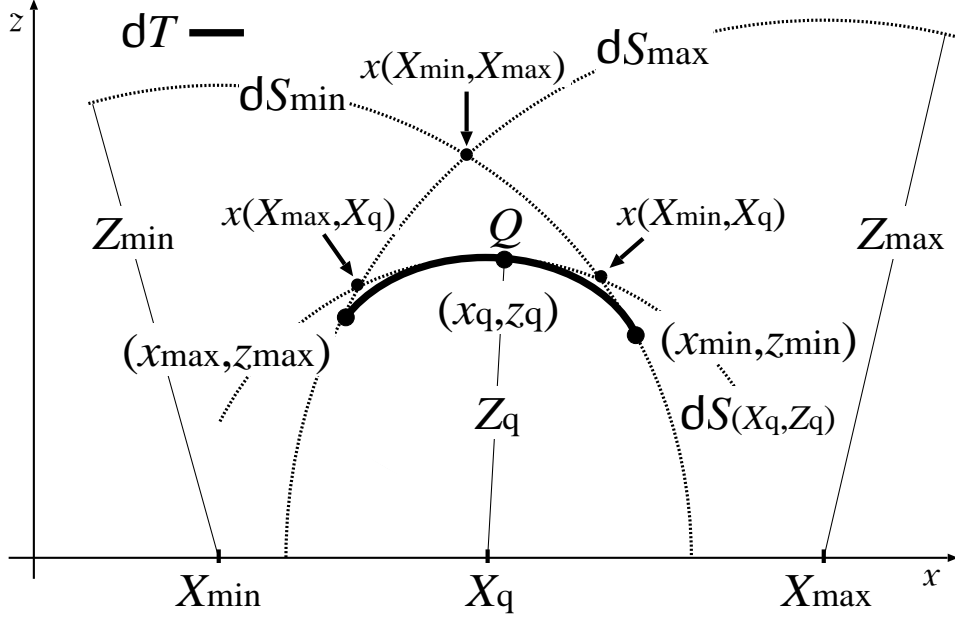
Figure B.3: Arrangement Q, $\partial S_{\min}$ and $\partial S_{\max}$ for the proof of the necessary condition of Proposition 1.

$x_{\mathrm{q}} < x_{\min}$ for $\partial x / \partial X < 0$. Here the intersection point of these two circles exists as only one because we assume $z \geq 0$. Therefore, $z_{\mathrm{Q}}(x) < z_{\mathrm{MIN}}(x)$ holds for $x \leq x_{\mathrm{q}}$, and $\partial S_{(X_{\mathrm{q}}, Z_{\mathrm{q}})} \subset \overline{S_{\min}}$ holds. Additionally, $S_{(X_{\mathrm{q}}, Z_{\mathrm{q}})} \subset \overline{S_{\min}}$ because of the definition of $S_{(X_{\mathrm{q}}, Z_{\mathrm{q}})}$ and $z \geq 0$. Therefore $\overline{S_{(X_{\mathrm{q}}, Z_{\mathrm{q}})}} \subset \overline{S_{\min}}$ holds. In the case of $x \geq x_{\mathrm{q}}$, we similarly prove $\overline{S_{(X_{\mathrm{q}}, Z_{\mathrm{q}})}} \subset \overline{S_{\max}}$ because $x_{\max} < x_{\mathrm{q}}$. Accordingly, $\overline{S_{(X_{\mathrm{q}}, Z_{\mathrm{q}})}} \subset \overline{S_{\min}} \cup \overline{S_{\max}}$ holds. This holds in the case of $X_{\mathrm{q}} = X_{\min}$ or $X_{\mathrm{q}} = X_{\max}$. Therefore, for all $(X, Z) \in \partial D$, this relationship holds, and the necessary condition of Proposition 1. is proved.

(ii). Proof of the sufficient condition of Proposition 1. We assume that $\partial x / \partial X > 0$ holds in $(X, Z) \in \partial D$. By Eq. (3.4), $\partial T = \partial S_{+}$ holds. We define $P \in \partial T$ as $(x_{\mathrm{p}}, z_{\mathrm{p}})$. In this region, $\overline{S_{+}} \subset \overline{S_{\max}} \cup \overline{S_{\min}}$ holds. Moreover, $P \in \overline{S_{+}}$ holds because $\partial T = \partial S_{+}$ and $\partial S_{+} \subset \overline{S_{+}}$ hold. Here $P = (x_{\mathrm{p}}, z_{\mathrm{p}}) \in \partial T$ should exist where $x_{\min} < x_{\mathrm{p}} < x_{\max}$ holds. We define $(X_{\mathrm{p}}, Z_{\mathrm{p}}) \in \partial D$ which is transformed from $(x_{\mathrm{p}}, z_{\mathrm{p}})$ with BST. With Prop. 2, $(x_{\mathrm{p}} - X_{\min})^2 + z_{\mathrm{p}}^2 > Z_{\min}^2$, and $(x_{\mathrm{p}} - X_{\max})^2 + z_{\mathrm{p}}^2 > Z_{\max}^2$ holds because $\partial x / \partial X > 0$ and $(x_{\mathrm{p}} - X_{\mathrm{p}})^2 + z_{\mathrm{p}}^2 = Z_{\mathrm{p}}^2$ holds. Therefore $P \notin \overline{S_{+}}$ holds because $P \notin \overline{S_{\min}}$ and $P \notin \overline{S_{\max}}$. However this relationship contradicts the previous assumption. Therefore the sufficient condition of Proposition 1. is proved.

112

Bibliography

[1] M. Okutomi and T. Kanade, "Stereo matching algorithm with multiple baselines," *IEICE Trans. Inf.& Syst.*, Vol. J75-D, No. 8, pp. 1317-1327, 1992 (in Japanese).

[2] M. Ogami, K. Ikeuchi and H. Hanekura, "3-dimensional visualization handbook," Asakura Publishing Co., ltd, vol. 1, pp. 33–71, Feb, 2006,

[3] K. Sakae, A. Amano, and N. Yokoya, "Optimization approaches in computer vision and image processing," *IEICE Trans. Inf.& Syst.*, Vol. E82-D, No. 3, pp. 534-547, 1999.

[4] Y. Yagi, "Omni-directional sensing and its applications," *IEICE Trans. Inf. & Syst.*, vol. E82-D, no. 3, pp. 548–557, 1999.

[5] T. Joochim and K. Chamnongthai, "Mobile robot navigation by wall following using polar coordinate image from omni-directional image sensor," *IEICE Trans. Inf. & Syst.*, vol. E85-D, no. 1, pp. 264–274, 1999.

[6] N. Yokoya, T. Shakunaga, and M. Kanbara, "Passive range sensing techniques: depth from images," *IEICE Trans. Inf.& Syst.*, vol. E82-D, no. 3, pp. 523–534, 1999.

[7] C. S. Chen, K. C. Hung, Y. P. Hung, L. L. Chen, and C. S. Fuh, "Semi-automatic tool for aligning a parameterized CAD model to stereo image pairs," *IEICE Trans. Inf. & Syst.* , vol. E82-D, no. 12, pp. 1582 – 1589, 1999.

[8] O. Nakayama, M. Shiohara, S. Sasaki, T. Takashima, and D. Ueno, "Robust vehicle detection under poor environmental conditions for rear and side surveillance," *IEICE Trans. Inf.&.Syst.*, vol. E87-D, no. 1, pp. 97–105, 2004

[9] Y. Kanazawa, and K. Kanatani, "Reliability of 3-D reconstruction by stereo vision," *IEICE Trans. Inf.& Syst.*, vol. E78-D, no. 10, pp. 1301–1307, 1995.

[10] H. Jeong and Y. Oh, "Fast stereo matching using constraints in discrete space," *IEICE Trans. Inf. & Syst.*, vol. E83-D, no. 7, pp. 1592–1600, 2000.

[11] S.H. Seo, M.R.A-Sadjadi and B. Tian, "A least-squares-based 2-D filtering scheme for stereo image compression," *IEEE Trans. Image Process.*, vol. 9, no. 11, pp. 1967–1972, Nov, 2000.

[12] G.L. Mariottini, G. Oriolo and D. Prattichizzo, "Image-based visual servoing for nonholonomic mobile robots using epipolar geometry," *IEEE Trans. Robot.*, vol. 23, no. 1, pp. 87–100, Feb, 2007.

[13] V. Lippiello, B. Siciliano and L. Villani, "Position-based visual servoing in industrial multirobot cells using a hybrid camera configuration," *IEEE Trans. Robot.*, vol. 23, no. 1, pp. 73–86, Feb, 2007.

[14] Y. Fang, I. Masaki and B. Horn, "Depth-based target segmentation for intelligent vehicles: fusion of radar and binocular stereo," *IEEE Trans. Intell. Transp. Syst.*, vol. 3, no. 3, pp. 196–202, Sep, 2002.

[15] L. Zhao and C.E. Thorpe, "Stereo and neural network-based pedestrian detection," *IEEE Trans. Intell. Transp. Syst.*, vol. 1, no. 3, pp. 148–154, Sep, 2000.

[16] Y. Suematsu and H. Yamada, "Image Processing Engineering," CORONA Publishing Co., LTD., pp. 179–210, 2000 (in Japanese).

[17] W. van der Mark and D.M. Gayrila, "Real-time dense stereo for intelligent vehicles," *IEEE Trans. Intell. Transp. Syst.*, vol. 7, no. 1, pp. 38–50, Mar, 2006.

[18] O. Ikeda, "Optical array imaging system with improved focusing function," *IEICE Trans. Fundamentals.*, vol. E76-A, no. 12, pp. 2108–2113, 1993.

[19] O. Ikeda, "A fast and adaptive imaging algorithm for the optical array imaging system," *IEICE Trans. Fundamentals.*, vol. E80-A, no. 6, pp. 1092–1098, 1997.

[20] Y. Oike, M. Ikeda and K. Asada, "A row-parallel position detector for high-speed 3-D camera based on light-section method," *IEICE Trans. Electron.*, vol. E86-C, no. 11, pp. 2320–2328, 2003.

[21] J.F. Whitaker, K. Yang, R. Rean and L.P.B. Katehi, "Electro-optic probing for microwave diagnostics," *IEICE Trans. Electron.*, vol. E86-C, no. 7, pp. 1328–1337, 2003.

[22] M.Q. Nguyen and M. Atkinson and H.G. Lewis, "Superresolution mapping using a hopfield neural network with LIDAR data," *IEEE Letters. Geosci. Remote Sens.*, vol. 2, no. 3, pp. 366–371, Jul, 2005.

[23] F. Hosoi and K. Omasa, "Voxel-based 3-D modeling of individual trees for estimating leaf area density using high-resolution portable scanning lidar," *IEEE Trans. Geosci. Remote Sens.*, vol. 44, no. 12, pp. 3610–3618, Dec, 2006.

114

[24] B. Ma, S. Lakshmanan and A. O. Hero III, "Simultaneous detection of lane and pavement boundaries using model-based multisensor fusion," *IEEE Trans. Intell. Transp. Syst.*, vol. 1, no. 3, pp. 135–147, Sep, 2000.

[25] T. Gandhi ad M.M. Trivedi, "Vehicle surround capture: survey of techniques and a novel omni-video-based approach for dynamic panoramic surround maps," *IEEE Trans. Intell. Transp. Syst.*, vol. 7, no. 3, pp. 293–308, Sep, 2006.

[26] S. Li, "Monitoring around a vehicle by a spherical image sensor," *IEEE Trans. Intell. Transp. Syst.*, vol. 7, no. 4, pp. 541–550, Dec, 2006.

[27] N. Hautiere, R. Labayrade and D. Aubert, "Real-time disparity contrast combination for onboard estimation of the visibility distance," *IEEE Trans. Intell. Transp. Syst.*, vol. 7, no. 2, pp. 201–212, Jun, 2006.

[28] N. Shimomura, K. Fujimoto, T. Oki and H. Muro, "An algorithm for distinguishing the types of objects on the road using laser radar and vision," *IEEE Trans. Intell. Transp. Syst.*, vol. 3, no. 3, pp. 189–195, Sep, 2002.

[29] Q. Zheng, S.Z. Der and H.I. Mahmoud, "Model-based target recognition in pulsed ladar imagery," *IEEE Trans. Image Process.*, vol. 10, no. 4, pp. 565–572, Apr, 2001.

[30] M. Grasmeuck and D.A. Viaggiano, "Integration of ground-penetrating radar and laser position sensors for real-time 3-D data fusion," *IEEE Trans. Geosci. Remote Sens.*, vol. 45, no. 1, pp. 130–137, Jan, 2007.

[31] C.Gronwall, F. Gustafsson and M. Millnert, "Ground target recognition using rectangle estimation," *IEEE Trans. Image Process.*, vol. 15, no. 11, pp. 3401–3409, Nov, 2006.

[32] K.C. Slatton, M.M. Crawford and B.L. Evans, "Fusing interferometric radar and laser altimeter data to estimate surface topography and vegetation heights," *IEEE Trans. Geosci. Remote Sens.*, vol. 39, no. 11, pp. 2470–2482, Nov, 2001.

[33] M. Pieraccini, L. Noeferini, D. Mecatti, C. Atzeni, G. Teza, A. Galgaro and N. Zaltron, "Integration of radar interferometry and laser scanning for remote monitoring of an urban site built on sliding slope," *IEEE Trans. Geosci. Remote Sens.*, vol. 44, no. 9, pp. 2335–2342, Seo, 2006.

[34] A. Broggi, M. Bertozzi, A. Fascioli, C.G.L. Bianco and A. Piazzi, "Visual perception of obstacles and vehicles for platooning," *IEEE Trans. Intell. Transp. Syst.*, vol. 1, no. 3, pp. 164–176, Sep, 2000.

[35] N. Portzgen, D. Gisolf and G. Blacquiere, "Inverse wave field extrapolation: a different NDI approach to imaging defects," *IEEE Trans. Ultrason., Ferroelect., Freq. Contr.*, vol. 54, no. 1, pp. 118–127, Jan, 2007.

[36] S.Y. Yi, "Global ultrasonic system for self-localization of mobile robot," *IEICE Trans. Commun.*, vol. E86-B, no. 7, pp. 2171–2177, 2003.

[37] C.Kim and H.W.Park, "Preprocessing and efficient volume rendering of 3-D ultrasound image," *IEICE Trans. Inf.& Syst.*, vol. E83-C, no. 2, pp. 259–264, 2000.

[38] E. Biagri, N. Dreoni, L. Masotti, I. Rossi and M. Scabia, "ICARUS: Imaging pulse compression algorithm through remapping of ultrasound," *IEEE Trans. Ultrason., Ferroelect., Freq. Contr.*, vol. 52, no. 2, pp. 261–279, Feb, 2005.

[39] F. Gran and J.A. Jensen, "Frequency division transmission imaging and synthetic aperture reconstruction," *IEEE Trans. Ultrason., Ferroelect., Freq. Contr.*, vol. 53, no. 5, pp. 900–911, May, 2006.

[40] D. Tomazevic, B. Likar, T. Slivnik and F. Pernus, "3-D/2-D registration of CT and MR to X-ray imaging," *IEEE Trans. Medical Imaging*, vol. 22, no. 11, pp. 1407–1416, Nov, 2003.

[41] H. Che and P.K. Varshney, "Mutual information-based CT-MR brain imaging registration using generalized partial volume joint histogram estimation," *IEEE Trans. Medical Imaging*, vol. 25, no. 6, pp. 723–731, Jun, 2003.

[42] C. R-Muller, H. B-Cattin, Y. Carillon, C. Odet, A. Briguet and F. Peyrin, "Bone MRI segmentation assessment based on synchrotron radiation computed microtomography," *IEEE Trans. Nuclear Science*, vol. 49, no. 1, pp. 220–224, Feb, 2002.

[43] D.W. Abraham, T.J. Chainer, K.F. Etzol and H.K. Wickramasinghe, "Thermal proximity imaging of hard-disk substrates," *IEEE Trans. Mathematics.*, vol. 36, no. 6, pp. 3997–4003, Nov, 2000.

[44] I. Pavlidis and J. Levine, "Thermal image analysis for polygraph testing," *IEEE Trans. Engineering in Medicine and Biology Magazine*, vol. 21, no. 6, pp. 56–64, Nov, 2002.

[45] H.M. Chen, S. Lee, R.M. Rao, M.A. Slamani and P.K. Varshney, "Imaging for concealed weapon detection; a tutorial overview of development in imaging sensors and processing," *IEEE. Signal Processing Magazine*, vol. 22, no. 2, pp. 52–61, Mar, 2005.

[46] X. Yin, B.W-H. Ng, B. Ferguson, S.P. Mickan and D. Abbott, "2-D wavelet segmentation in 3-D T-ray tomography," *IEEE Sensor Journal*, vol. 7, no. 3, pp. 342–343, Mar, 2007.

[47] K. Ohta, "Electrodynamics I," Maruzen Publishing Co., ltd, pp. 271 – 300, Oct, 2000 (in Japanese).

[48] N. Hasebe, "Radio wave engineering," Corona Publishing Co., ltd, pp. 13–3, May, 1995 (in Japanese).

[49] J,Umoto, "Electromagnetics," Shoukoudou, pp. 297–330, Jun, 1975 (in Japanese)

[50] T. Uno, "Electromagnetic and antenna analysis with FDTD method", CORONA Publishing Co., LTD., pp. 265–269, 1998 (in Japanese).

[51] H. Arai "New antenna engineering", Sougou Densi Publishing Co., LTD, pp. 162–172.1996 (in Japanese).

[52] T. Homma, H. Igarashi and H. Kawaguchi, "Numerical Electro-magnetic Dynamics," Morikita Publishing Co., Ltd., pp. 68–110, 2002 (in Japanese).

[53] N. Kumatani and N. Morita, "Electro-magnetic Wave and Boundary Element Method," Morikita Publishing Co., Ltd., pp. 145–189, 1987 (in Japanese).

[54] The Institute of Electronics, Information and Communication Engineers, "Basic Analysis for Electro-magnetic Problems," CORONA Publishing Co., LTD., pp. 198–227, 1987 (in Japanese).

[55] D. L. Mensa, G. Heidbreder, and G. Wade, "Aperture synthesis by object rotation in coherent imaging," *IEEE Trans. Nuclear Science.*, vol. 27, no. 2, pp. 989–998, Apr, 1980.

[56] T. Takano, T. Sato, M. Kashimoto and M. Murata, "Remote sensing and navigation with radio wave in aerospace," CORONA Publishing Co., LTD., pp. 69-72, 2000 (in Japanese).

[57] The Institute of Electronics, Information and Communication Engineers, "Radar Techniques,", CORONA Publishing Co., LTD., pp. 299-302, 1984 (in Japanese).

[58] R. O. Harger, "Synthetic aperture radar systems theory and design," Academic Press, pp. 18–82

[59] J. P. .Fitch, "Synthetic aperture radar,", pp. 33–82. 1988.

[60] "On the Bragg scattering observed in L-Band synthetic aperture radar images of flooded rice fields," *IEICE Trans. Commun.*, vol. E89-B, no. 8, pp. 2218–2225, 2006.

[61] K. Yamamoto, M. Iwamoto and T. Kirimoto, "A new algorithm to generate the reference images of ship target for ATR using ISAR," *IEICE Trans. Commun.*, vol. E88-B, no. 2, pp. 737–744, 2005.

[62] K.J. Ranson, S. Saatchi and G. Sun, "Boreal forest ecosystem characterization with SIR-C/XSAR," *IEEE Trans. Geosci. Remote Sens.*, vol. 33, no. 4, pp. 867–876, Jul, 1995.

[63] D. Haverkamp, L.K. Soh and C. Tsatsoulis, "A comprehensive, automated approach to determining sea ice thickness from SAR data," *IEEE Trans. Geosci. Remote Sens.*, vol. 33, no. 1, pp. 46–57, Jan, 1995.

[64] C. Swift and L.R. Wilson, "Synthetic aperture radar imaging of moving ocean waves," *IEEE Trans. Antenna Propagat.*, vol. 27, no. 6, pp. 725–729, Nov, 1979.

[65] C.L. Rufenach and W.R. Alpers, "Imaging ocean waves by synthetic aperture radars with long integration times," *IEEE Trans. Antenna Propagat.*, vol. 29, no. 3, pp. 422–428, May, 1981.

[66] T. Moriyama, Y. Yamaguchi, S. Uratsuka, T. Umehara, H. Maeno, M. Satake, A. Nadai and K. Nakamura, "A study om polarimetric correlation coefficient for feature extraction of polarimetric SAR data," *IEICE Trans. Commun.*, vol. E88-B, no. 6, pp. 2353–2361, 2005.

[67] K. Hayshi, R. Sato, Y. Yamguchi and H. Yamada, "Polarimetric scattering analysis for a finite dihedral corner reflector," *IEICE Trans. Commun.*, vol. E89-B, no. 1, pp. 191–195, 2006.

[68] K. Suwa and M. Iwamoto, "A two-dimensional bandwidth extrapolation technique for polarimetric synthetic aperture radar images," *IEEE Trans. Geosci. Remote Sens.*, vol. 45, no. 1, pp. 45–54, Jan, 2007.

[69] Y. Hara, R.G. Atkins, R.T. Shin, J.A. Kong, H.Yueh and R. Kwok, "Application of neural networks for sea ice classification in polarimetric SAR images," *IEEE Trans. Geosci. Remote Sens.*, vol. 33, no. 2, pp. 740–748, Mar, 1995.

[70] S.R. Cloud and E.Pottier, "An entropy based classification scheme for land applications of polarimetric SAR," *IEEE Trans. Geosci. Remote Sens.*, vol. 35, no. 1, pp. 68–78, Jan, 1997.

[71] A. Freeman and S.L. Durden, "A three-component scattering model for polarimetric SAR data," *IEEE Trans. Geosci. Remote Sens.*, vol. 36, no. 3, pp. 963–973, May, 1998.

[72] Y.Dong, B.C. Forester and C. Ticehurst, "A new decomposition of radar polarization signatures," *IEEE Trans. Geosci. Remote Sens.*, vol. 36, no. 3, pp. 933–939, May, 1998.

[73] J. Xu, J, Yang, Y. Peng, C. Wang, and Y-A. Liou, "Using similarity parameters for supervised polarimetric SAR image classification," *IEICE Trans. Commun.*, vol. E85-B, no. 12, pp. 2934–2942, Dec, 2002.

[74] T. Moriyama, S. Uratsuka, T. Umehara, H. Maeno, M. Satake, A. Nadai and K. Nakamura, "Polarimetric SAR image analysis using model fit for urban structures," *IEICE Trans. Commun.*, vol. E88-B, no. 3, pp. 1234–1243, 2005.

[75] S. Fukuda and H. Hirosawa, "Polarimetric SAR image classification using support vector machines," *IEICE Trans. Electron.*, vol. E84-C, no. 12, pp. 1939–1945, 2001.

[76] E. Collin, C. Titin-Schnaider and W. Tabbara, "An interferometric coherence optimization method in radar polarimetry for high-resolution imagery," *IEEE Trans. Geosci. Remote Sens.*, vol. 44, no. 1, pp. 167–175, Jan, 2006.

[77] H. Yamada, Y. Yamaguchi, Y. Kim, E. Rodriguez and W.M. Boerner, "Polarimetric SAR interferometry for forest analysis based on the ESPRIT algorithm," *IEICE Trans. Electron.*, vol. E84-C, no. 12, pp. 1917–1924, 2001.

[78] S. Cloude, K. P. Papathanassiou, and E. Pottier "Radar polarimetry and polarimetric interferometry" *IEICE Trans. Electron.*, vol. E84-C, no. 12, pp. 1814–1822, 2001.

[79] A.B. Suksmono and A. Hirose., "A fractal estimation method to reduce the distortion in phase unwrapping process," *IEICE Trans. Commun.*, vol. E88-B, no. 1, pp. 364–371, 2005.

[80] A.B. Suksmono and A. Hirose., "Progressive transform-based phase unwrapping utilizing a recursive structure," *IEICE Trans. Commun.*, vol. E89-B, no. 3, pp. 929–936, 2006.

[81] "Two-dimensional active imaging of conducting objects buried in a dielectric half-space," Y. He, T. Uno, S. Adachi and T. Mashiko, *IEICE Trans. Commun.*, vol. E76-B, no. 12, pp. 1546–1551, 1993.

[82] M. Tanaka and K. Ogata, "Fast inversion method for electromagnetic imaging of cylindrical dielectric objects with optimal regularization," *IEICE Trans. Commun.*, vol. E84-B, no. 9, pp. 2560–2565, 2001.

[83] N.V. Budko, R.F. Remis and P.M. van den Berg, "Two-dimensional imaging and effective inversion of a three-dimensional buried object," *IEICE Trans. Electron.*, vol. E83-C, no. 12, pp. 1889–1895, 2000.

[84] C. Pichot, P. Lobel, C. Dourthe, L.B. Feraud and M. Barlaud, "Microwave inverse scattering: quantitative reconstruction of complex permittivity for different applications," *IEICE Trans. Electron.*, vol. E80-C, no. 11, pp. 1343–1348, 1997.

[85] Q. Fang, P.M. Meaney and K.D. Paulsen, "Singular value analysis of the Jacobian matrix in microwave image reconstruction," *IEEE Trans. Antenna Propagat.*, vol. 54, no. 8, pp. 2371–2380, Aug, 2006.

[86] A. Massa, D. Franceschini, G. Franceschini, M. Pastorino, M. Raffetto and M. Donelli, "Parallel GA-based approach for microwave imaging applications," *IEEE Trans. Antenna Propagat.*, vol. 53, no. 10, pp. 3118–3127, Oct, 2005.

[87] M. Benedetti, M. Donelli and A. Massa, "Multicrack detection in two-dimensional structures by means of GA-based strategies," *IEEE Trans. Antenna Propagat.*, vol. 55, no. 1, pp. 205–215, Jan, 2007.

[88] T. Huang and A.S. Mohan, "Microwave imaging of three dimensional dielectric objects," *IEICE Trans. Commun.*, vol. E88-B, no. 6, pp. 2369–2376, 2005.

[89] G.A. Tsihrintzis and A.J. Devaney, "Higher-order (Nonlinear) diffraction tomography: reconstruction algorithm and computer simulation," *IEEE Trans. Image Process.*, vol. 9, no. 9, pp. 1560–1572, Sep, 2000.

[90] C. Zhou and L. Liu, "Radar-diffraction tomography using the modified quasi-linear approximation," *IEEE Trans. Geosci. Remote Sens.*, vol. 38, no. 1, pp. 404–415, Jan, 2000.

[91] T.J. Cui and W.C. Chew, "Diffraction tomographic algorithm for the detection of three-dimensional objects buried in a lossy half-space," *IEEE Trans. Antenna Propagat.*, vol. 50, no. 1, pp. 42–49, Jan, 2002.

[92] T.B. Hansen and P.M. Johansen, "Inversion scheme for ground penetrating radar that takes into account the planar air-soil interference," *IEEE Trans. Geosci. Remote Sens.*, vol. 38, no. 1, pp. 496–506, Jan, 2000.

[93] L.P. song, C. Yu and Q.H. Liu, "Through-wall imaging (TWI) by radar: 2-D tomographic results and analysis," *IEEE Trans. Geosci. Remote Sens.*, vol. 43, no. 12, pp. 2793–2798, Dec, 2005.

[94] S.Y. Semenov, A.E. Bulyshev, A.Abubakar, V.G. Posukh, Y.E. Sizov, A.E. Souvorov, P.M. van den Berg and T.C. Williams, "Microwave-tomographic imaging of the high dielectric-contrast objects using different image-reconstruction approaches," *IEEE Trans. Microw. Theory and Tech.*, vol. 53, no. 7, pp. 2284–2294, Jul, 2005.

[95] A. Furusawa, T. Wakayama, T. Sato and I. Kimura, "Two-dimensional interpolation in the wavenumber domain for radar image reconstruction," *IEICE Trans. Commun.*, vol. J76-B-II, no. 4, pp. 293–300, 1993.

[96] T. Isernia, V. Pascazio and R. Pierri, "A nonlinear estimation method in tomographic imaging," *IEEE Trans. Geosci. Remote Sens.*, vol. 35, no. 4, pp. 910–923 Jul, 1997.

[97] T. Hasegawa, M. Hoshino, and T. Iwasaki, "Microwave imaging by equivalent inverse diffraction," *IEICE Trans. Commun.*, vol. E83-B, no. 9, pp. 2032–2037, 2000.

[98] D. Nahamoo, S. X. Pan and A. C. Kak, "Synthetic aperture diffraction tomography and its interpolation-free computer implementation," IEEE Trans. Sonics and Ultrasonics., vol.31, no.4, pp.218–229, 1984.

[99] H. Harada, D. Wall, T. Takenaka, and M. Tanaka, "Conjugate gradient method applied to inverse scattering problem," *IEEE Trans. Antenna Propagat.*, vol. 43, no. 8, pp. 784–792, 1995.

[100] A. Qing and C. K. Lee, "A study on improving the convergence of the real-coded genetic algorithm for electromagnetic inverse scattering of multiple perfectly conducting cylinders." *IEICE Trans. Electron.*, vol. E85-C, no. 7, pp. 1460–1471, 2002.

[101] C. Chiu, C. Li, and W. Chan, "Image reconstruction of a buried conductor by the genetic algorithm," *IEICE Trans. Electron.*, vol. E84-C, no. 12, pp. 1946–1951, 2001.

[102] T. Sato, K. Takeda, T. Nagamatsu, T. Wakayama, I. Kimura, and T. Shinbo, "Automatic signal processing of front monitor radar for tunneling machines," *IEEE Trans. Geosci. Remote Sens.*, vol. 35, no. 2, pp. 354–359, 1997.

[103] A. Qing, "Electromagnetic inverse scattering of multiple perfectly conducting cylinders by differential evolution strategy with individual in group," *IEEE Trans. Antenna Propagat.*, vol. 51, no. 6, pp. 1787–1794, 2002.

[104] T. Takenaka, H. Jia, and T. Tanaka, "Microwave imaging of an anisotropic cylindrical object by a forward-backward time-stepping method," *IEICE Trans. Electron.*, vol. E84-C, no. pp. 1910–1916, 2001.

[105] T. Sato, T. Wakayama, and K. Takemura, "An imaging algorithm of objects embedded in a lossy dispersive medium for subsurface radar data processing," *IEEE Trans. Geosci .Remote Sens.*, Vol. 38, No. 1, pp. 296-303, 2000.

[106] H. Zhou and M. Sato, "Subsurface cavity imaging by crosshole borehole radar measurement," *IEEE Trans. Geosci. Remote Sens.*, vol. 42, no. 2, pp. 335–331, Feb, 2004.

[107] J. Song, Q.H. Liu, P. Torrione and L. Collins, "Two-dimensional and three-dimensional NUFFT migration method for landmine detection using ground-penetrating radar," *IEEE Trans. Geosci. Remote Sens.*, vol. 44, no. 6, pp. 1462–1469, Jun, 2006.

[108] X. Xu, E.L. Miller and C.M. Rappaport, "Minimum entropy regularization in frequency-wavenumber migration to localize subsurface objects," *IEEE Trans. Geosci. Remote Sens.*, vol. 41, no. 8, pp. 1804–1812, Aug, 2003.

[109] S.K. Davis, H. Tandradinata, S.C. Hagness and B.D. van Veen, "Ultrawideband microwave breast cancer detection: a detection-theoretic approach using the generalized likelihood ratio test," *IEEE Trans. Biomedical Engineering*, vol. 52, no. 7, pp. 1237–1250, Jul, 2005.

[110] S.A. Greenhalgh, D.R. Pant, and C.R. Rao, "Effect of reflector shape on seismic amplitude and phase," *Wave Motion*, vol. 16, no. 4, pp. 307–322, Dec, 1992.

[111] J. Zhe and S.A. Greenhalgh, "A new kinematics method for mapping seismic reflectors," *Geophysics*, vol. 64, no. 5, pp. 1594–1602, Sep/Oct, 1999.

[112] S.A. Greenhalgh and L. Marescot, "Modeling and migration of 2-D georadar data: a stationary phase approach," *IEEE Trans. Geosci. Remote Sens.*, vol. 44, no. 9, pp. 2421–2429, Sep, 2006.

[113] T. Sato, "Shape estimation of space debris using single-range Doppler interferometry," *IEEE Trans. Geosci. Remote Sens.*, vol. 37, no. 2, pp. 1000–1005, Mar, 1999.

[114] W.L. van Rossum, M.P.G. Otten and R.J.P. van Bree, "Extended PGA for range migration algorithm," *IEEE Trans. Aerospace and Electronic Systems*, vol. 42, no. 2, pp. 478–488, Apr, 2006.

[115] C.J. Leuschen, R.G. Plumb, "A matched-filter-based reverse time migration algorithm for ground penetrating radar data," *IEEE Trans. Geosci. Remote Sens.*, vol. 39, no. 5, pp. 929–937, May, 2001.

[116] M. Converse, E.J. Bond, B.D. Van Veen and S.C. Hagness, "A computational study of ultra-wideband versus narrowband microwave hyperthermia for breast cancer treatment," *IEEE Trans. Microw. Theory and Tech.*, vol. 54, no. 5, pp. 2169–2180, May, 2006.

[117] E. J. Bond, X. Li, S. C. Hagness, and B. D. van Veen, "Microwave imaging via space-time beamforming for early detection of breast cancer" *IEEE Trans. Antenna Propagat.*, vol. 51, no. 8, pp. 1690–1705, 2003.

[118] S.K. Davis, E.J. Bond, X. Li, S.C. Hagness, and B.D. Van Veen, "Microwave imaging via space-time beamforming for early detection of breast cancer: Beamformer design in the frequency domain," *Journal of Electromagnetic Waves and Applications.*, 17,2, pp. 357–381, 2003.

[119] X. Li, S.K. Davis, S.C. Hagness, D.W. van der Weide, and B.D. van Veen, "Microwave imaging via space-time beamforming: experimental investigation of tumor detection in multi-layer breast phantoms," *IEEE Trans. on Microwave Theory and Techniques*, vol. 52, no. 8, pp. 1856–1865, Aug, 2003.

[120] X. Li, E.J. Bond, B.D. Van Veen and S.C. Hagness, "An overview of Ultra-Wideband microwave imaging via space-time beamforming for early-stage breast-cancer detection," *IEEE Magazine, Antennas and Propagat.*, vol. 47, no. 1, pp. 19–34, Feb, 2005.

[121] S. Adachi, T. Uno and T. Nakaki, "Two-dimensional target profiling by electromagnetic backscattering," *IEICE Trans. Electron.*, vol. E76-C, no. 10, pp. 1449–1455, 1993.

[122] N. Kologo and M.Ph. Stoll, "CO_2 laser light scattering by bare soils for emissivity measurements: absolute calibration and correlation with backscattering and composition," *IEEE Trans. Geosci. Remote Sens.*, vol. 34, no. 4, pp. 936–945, Jul, 1997.

[123] D. Liu, S. Vasudevan, J. Krolik, G. Bal and L. Carin, "Electromagnetic time-reversal source localization in changing media; experiment and analysis," *IEEE Trans. Antenna Propagat.*, vol. 55, no. 2, pp. 344–354, Feb, 2007.

[124] Y. Chen, E. Gunawan, K.S. low, S. Wang, Y. Kim and C.B. Soh, "Pulse design for time reversal method as applied to ultrawideband microwave breast cancer detection: a two-dimensional analysis," *IEEE Trans. Antenna Propagat.*, vol. 55, no. 1, pp. 194–204, Jan, 2007.

[125] P. Kosmas and C.M. Rappaport, "FDTD based time reversal for microwave breast cancer detection - localization in three dimensions," *IEEE Trans. Microw. Theory and Tech.*, vol. 54, no. 4, pp. 1921–1297, Apr, 2006.

[126] D. Liu, G. Kang, L. Li, Y. Chen, S. Vasudevan, W. Joines, Q.H. Liu, J. Krolik and L. Carin, "Electromagnetic time-reversal imaging of a target in a cluttered environment," *IEEE Trans. Antenna Propagat.*, vol. 53, no. 9, pp. 3058–3066, Sep, 2005.

[127] T. Sakamoto and T. Sato, "A target shape estimation algorithm for pulse radar systems based on boundary scattering transform," *IEICE Trans. Commun.*, vol.E87-B, no.5, pp. 1357–1365, 2004.

[128] T. Sakamoto and T. Sato, "A phase compensation algorithm for high-resolution pulse radar systems," *IEICE Trans. Commun.*, vol.E87-B, no.6, pp. 1631–1638, 2004.

[129] T. Sakamoto, "A fast algorithm for 3-dimensional imaging with UWB pulse radar systems," *IEICE Trans. Commun.*, vol.E90-B, no.3, pp. 636–644, 2007.

[130] T. Sakamoto, S. Kidera, T. Sato and S. Sugino, "An experimental study on a fast 3-D imaging algorithm for UWB pulse radars," *IEICE Trans. Commun.*, vol.J90-B, no.1, pp. 66–73, 2007 (in Japanese).

[131] T. Sakamoto and T. Sato, "A 2-D image stabilization algorithm for UWB pulse radars with fractional boundary scattering transform," *IEICE Trans. Commun.*, vol.E90-B, no.1, pp. 131–139, 2007.

[132] M. Tsunasaki, H. Mitsumoto, and M. Kominami, "Aperture estimation of the underground pipes by ellipse estimation from ground penetrating radar image," Technical Report of IEICE, SANE2003–52, Sep, 2003 (in Japanese).

[133] K. Maeda and I. Kimura, "Modern electromagnetic wave theory," Ohm Co., Ltd., pp. 70–72, 1984 (in Japanese).

[134] K. Nishimura, T. Sato, T. Nakamura, and M. Ueda, "High Sensitivity Radar-Optical Observations of Faint Meteors," *IEICE Trans. Commun.*, vol.E84-C, no.12, pp. 1877–1884, Dec., 2001.

Major Publications

Refereed Papers

1 . Shouhei Kidera, Takuya Sakamoto, Toru Sato and Satoshi Sugino, "An Accurate Imaging Algorithm with Scattered Waveform Estimation for UWB Pulse Radars", *IEICE Trans. Commun.*, vol. E89-B, no. 9, pp. 2588-2595, Sept., 2006

2 . Shouhei Kidera, Takuya Sakamoto and Toru Sato, "A High-Resolution Imaging Algorithm without Derivatives Based on Waveform Estimation for UWB Radars", *IEICE Trans. Commun.*, vol.E90-B, no.6, pp. 1487–1494, June, 2007.

3 . Shouhei Kidera, Takuya Sakamoto and Toru Sato, "A Robust and Fast Imaging Algorithm with an Envelope of Circles for UWB Pulse Radars", *IEICE Trans. Commun.*, vol.E90-B, no.7, pp. 1801–1809 July, 2007.

Refereed Conference Proceedings

1 . Shouhei Kidera, Takuya Sakamoto and Toru Sato, "A High-Resolution Imaging Algorithm Based on Scattered Waveform Estimation for UWB Pulse Radar Systems,", Proc. 2005 IEEE International Geoscience and Remote Sensing Symposium, pp. 1725-1728, July, 2005.

2 . Shouhei Kidera, Takuya Sakamoto, and Toru Sato, "A High-Resolution 3-D Imaging Algorithm with Linear Array Antennas for UWB Pulse Radar Systems," IEEE AP-S International Symposium, USNC/URSI National Radio Science Meeting, AMEREM Meeting, pp.1057-1060, July, 2006.

3 . Shouhei Kidera, Takuya Sakamoto and Toru Sato, "A Robust and Fast Imaging Algorithm with an Envelope of Circles for UWB Pulse Radars," Progress in Electromagnetics Research Symposium (PIERS), Aug., 2006.

4 . Shouhei Kidera, Takuya Sakamoto and Toru Sato, "A Robust and Fast Imaging Algorithm without Derivative Operations for UWB Pulse Radars," European Conference on Antennas & Propagation (EuCAP) 2006, paper no.314368, Nov. 2006.

5 . Shouhei Kidera, Takuya Sakamoto and Toru Sato, "A High-resolution Imaging Algorithm without Derivatives based on Waveform Estimation for UWB Radars," IEEE AP-S International Symposium 2007, No. 144.6, Jun. 2007.

6 . Shouhei Kidera, Takuya Sakamoto and Toru Sato, "A Robust and Fast 3-D Imaging Algorithm without Derivative Operations for UWB Pulse Radars," EMTS2007, International URSI Commision B Electromagnetic Theory Symposium, no. EMTS084, 26-28 Jul. 2007.